UNIVERSITY OF SOUTHAMPTON

FACULTY OF ENGINEERING, SCIENCE & MATHEMATICS

School of Engineering Sciences

Direct and Large-Eddy Simulation of Interactions between Reacting Flows and Evaporating Droplets

by

Jun Xia

Thesis for the degree of Doctor of Philosophy

February 2008

UNIVERSITY OF SOUTHAMPTON

ABSTRACT

FACULTY OF ENGINEERING, SCIENCE & MATHEMATICS
SCHOOL OF ENGINEERING SCIENCES

Doctor of Philosophy

DIRECT AND LARGE-EDDY SIMULATION OF INTERACTIONS BETWEEN REACTING FLOWS AND EVAPORATING DROPLETS

by Jun Xia

Reacting flows interacting with liquid droplets are of practical and scientific importance due to their appearance in a multiplicity of industrial and domestic applications such as fire suppression systems and humidified gas turbines. Experimental measurements are usually limited to global quantities or local quantities at limited spatial locations, which provide little detailed information for fundamental understanding of complex interactions. Numerical simulations can overcome these limitations, but are restricted by the available computer capacity. Therefore, most previous simulations in the field employ simplifications such as a two-dimensional configuration, the Eulerian description of the dispersed phase, or the Reynolds averaged Navier-Stokes (RANS) methodology, etc. Such simplified methods are not appropriate for scrutinizing the local, unsteady interactions embedded in the realistic multiphase reacting flows from the first principle. To this end, systematic understanding of the multilateral, multiscale and multiphysics interactions among turbulent flow, chemical reaction and dispersing droplets is still far from being achieved.

Recently, the rapid development of the supercomputer hardware and software technologies enables the application of high fidelity numerical techniques, i.e., direct numerical simulation (DNS) and large eddy simulation (LES), to such complex flows. In the present study, a hybrid Eulerian-Lagrangian methodology is developed and implemented to investigate the multiphysics interactions. The well-designed parallel algorithms enable us to look at both canonical and practical configurations, including a temporal reacting shear layer, a turbulent reactive jet diluted with droplets and a simplified small-scale domestic fire suppression system. All these configurations are characterised by nonuniform droplet loading in the computational domain, fully three-dimensional simulation and the Lagrangian description for droplets. The number of traced droplets reaches the magnitude of 10^6 in some cases. DNS results with various physical parameters have been obtained, showing self-consistency and correct trends. In LES, to avoid arbitrary tuning of subgrid model coefficients, fully dynamic procedures have been designed following the Germano procedure and implemented for the main six subgrid models. LES of a heated plane jet, a reacting jet diluted with evaporating droplets and a simplified fire suppression system has been performed and analysed. Droplet effects on turbulence and combustion are quantified through examining the transport equations for the kinetic energy and internal energy of the reacting flow.

Table of Contents

List of Figures

List of Tables

DECLARATION OF AUTHORSHIP

I, ……., [please print name]

declare that the thesis entitled [enter title]

……

……

and the work presented in the thesis are both my own, and have been generated by me as the result of my own original research. I confirm that:

- this work was done wholly or mainly while in candidature for a research degree at this University;
- where any part of this thesis has previously been submitted for a degree or any other qualification at this University or any other institution, this has been clearly stated;
- where I have consulted the published work of others, this is always clearly attributed;
- where I have quoted from the work of others, the source is always given. With the exception of such quotations, this thesis is entirely my own work;
- I have acknowledged all main sources of help;
- where the thesis is based on work done by myself jointly with others, I have made clear exactly what was done by others and what I have contributed myself;
- none of this work has been published before submission, **or** [delete as appropriate] parts of this work have been published as: [please list references]

Signed: ……..

Date:…….

Acknowledgements

This project was supported in part by the BRE Trust and the EPSRC (Grant No: EP/E011640/1). The computing resource on the UK national supercomputing facilities HPCx and HECToR are from the UK Consortium on Computational Combustion for Engineering Applications (COCCFEA) (EPSRC Grant No: EP/D080223/1) and the UK Turbulence Consortium (UKTC) (EPSRC Grant No: EP/D044073/1).

I would like to express the grateful thanks to both my supervisors, Prof. Kai H. Luo at the University of Southampton and Prof. Suresh Kumar at the BRE Global Limited, for bringing me into the mysterious but amazing world of multiphase combustion. What they have offered me is much more than the technical support. Especially, I have been enjoying so much in the communication with them from both the academic and industrial views on same technical issues.

The supporting teams at the Daresbury Laboratory, the NAG and the Cray Excellence Centre for the UK supercomputing facilities deserve special thanks. Their help is professional, prompt and patient.

I cherish the colleagueship and friendship in these years, and would like to put all these names in the bottom of my heart instead of consuming another half a page to list them out.

Finally, I would like to thank my wife, who has been with me during the whole tough but enjoyable period of my PhD. I will forever remember your encourage and support when I felt helpless, depressed and frustrated. Please believe if we can make this PhD possible, then we must be able to make anything possible.

Notation

A_d	Droplet surface area $\left(A_\mathrm{d}=\pi D_\mathrm{d}^2\right)$
A_T	Total surface area of droplets exposed to the gas
B_M	Spalding number for mass transfer $\left\{B_\mathrm{M}=\left(Y_\mathrm{v,surf}-Y_\mathrm{v,far}\right)/\left(1-Y_\mathrm{v,surf}\right)\right\}$
c	Speed of sound
c_p	Heat capacity at constant pressure
c_v	Heat capacity at constant volume
C_d	Dynamic coefficient of the Smagorinsky model
C_D	Coefficient for the inter-phase drag
C_I	Dynamic coefficient of the Yoshizawa model
C_T, C_Y	Dynamic coefficients of the eddy-diffusivity models
CFL	Courant-Friedrichs-Lewy number
D	Mass diffusivity; Dissipation
D_d	Droplet diameter
e	Internal energy per unit mass $\left(e=h_\mathrm{r}^0+c_\mathrm{v}T\right)$
E_a	Activation energy for reaction
E_T	Total energy per unit volume $\left\{E_\mathrm{T}=\rho\left(e+u_i u_i/2\right)\right\}$
f	Correction coefficient to the Stokes drag; Frequency

f_c	Collision frequency of the reactant molecular
F_{2D}, F_{3D}	Amplitude of the initial 2D and 3D disturbances used for the temporal mixing layer; Defined as ratio of the disturbance circulations to the approximated circulation due to the mean velocity.
F_{drag}	Stokes drag force exerted on droplets
g	Gravitational acceleration
$G(x)$	Convolution kernel function for filtering operations
h	Enthalpy; Grid spacing; Jet nozzle width
h_{fg}	Latent heat of evaporation
h_t	Convective heat transfer coefficient
H_M	Specific driving potential for mass transfer
I_v, II_v, III_v	Source terms due to droplet evaporation for the transport equation of the mixture fraction variance $\widetilde{Z''^2}$
k	Thermal conductivity
K	Model coefficient for the filtered reaction rate $\overline{\omega_T}$
l, L	Length
$L_i(x)$	Basic functions in the Lagrangian interpolation scheme
L_x, L_y, L_z	Computational domain size
m	Mass
$\dot{m}_d$	Droplet evaporation rate
MLR	Mass Loading Ratio, defined as the initial ratio of droplet mass to oxidizer mass in Chapter IV, the ratio of the mass flow rate of droplets to that of the gas fuel at the jet nozzle in Chapter V, and the ratio of the mass flow rate of droplets at the sprinkler nozzle to that of the gas fuel at the jet nozzle in Chapter VI.
n_x, n_y, n_z	Grid point numbers

n_{d}	droplet number density
N_{d}	Total number of droplets in the computational domain
N_{s}	Total number of species existed in the chemical reaction
N_{R}	Number of physical droplets represented by one computational droplet
p	Pressure
P	Production
q	Heat flux per unit area
$\mathbf{Q}$	Conservative flow variables $\left\{\mathbf{Q}=\left(\rho,\rho u,\rho v,\rho w,\rho E_{\mathrm{T}},\rho Y_{\mathrm{f}},\rho Y_{\mathrm{o}},\rho Y_{\mathrm{v}}\right)^{\mathrm{T}}\right\}$
Q_{h}	Heat of combustion
R	Gas constant for the ideal gas law [unit: J/(kg K)]
$\overline{R}$	Universal gas constant for the ideal gas law [unit: J/(mol K)]
S	Density ratio of the fuel stream at the jet nozzle to the ambient air
S^{+}, S^{-}	Source terms due to droplet evaporation for the transport equation of the mixture fraction variance $\widetilde{Z''^2}$ $\left(\overline{\rho_{\mathrm{g}}}\widetilde{S^{+}}=I_{\mathrm{v}}+II_{\mathrm{v}},\ \overline{\rho_{\mathrm{g}}}\widetilde{S^{-}}=III_{\mathrm{v}}\right)$
$\lvert S\rvert$	Magnitude of the strain rate $\left(\lvert S\rvert^2=2S_{pq}S_{pq}\right)$
S_{ij}	Strain rate $\left\{S_{ij}=\left(\partial u_i/\partial x_j+\partial u_j/\partial x_i\right)/2\right\}$
S_{ms}, S_{mo}, S_{en}	Droplet source terms due to mass, momentum and energy coupling with the carrier phase
SG_{mo}, SG_{en}, SG_{sp}	Subgrid terms in the momentum, energy and species equations
t	Time
T	Temperature; Time period

T_{f}	Adiabatic flame temperature
T_{B}	Normal boiling temperature of the liquid phase
u, v, w, U	Velocity
V	Grid cell volume in DNS
V_{f}	Filtering volume in LES
W	Molecular weight
$\dot{W}_{\mathrm{v}}$	Source terms due to droplet evaporation for the transport equation of the mixture fraction $\tilde{Z}$ $\left(\rho_{\mathrm{g}}\dot{W}_{\mathrm{v}} = S_{\mathrm{ms}}\right)$
x_i	Cartesian coordinate directions. [i=1 ↔ streamwise (x); i=2 ↔ cross-stream (y); i=3 ↔ spanwise (z)] for temporally developing flows in Chapter IV; [i=1 ↔ spanwise (x); i=2 ↔ lateral (y); i=3 ↔ streamwise (z)] for spatially developing flows in Chapters V and VI.
Y	Species mass fraction
Z	mixture fraction
$\Delta h^0_{\mathrm{f},i}$	Mass enthalpy of formation of species i
Δt	Time step
Δx, Δy, Δz	Grid spacing
$\overline{\Delta}$	Grid (F-level) filter width
$\hat{\Delta}$	Test (G-level) filter width
$\hat{\overline{\Delta}}$	FG-level filter width
ℓ	Amplitude variations of the characteristic waves
Da	Damköhler number, defined as the ratio of flow characteristic time to chemical characteristic time. $\left\{Da = t^*_{\mathrm{r}} f^*_{\mathrm{c}} \left(\rho^*_{\mathrm{r}}/W^*_{\mathrm{r}}\right)^{\upsilon_{\mathrm{f}}+\upsilon_{\mathrm{o}}-1}\right\}$
Fr	Froude number, defined as the ratio of inertial force to gravitational force. $\left\{Fr = u^{*2}_{\mathrm{r}} \big/ \left(g^*_{\mathrm{r}} l^*_{\mathrm{r}}\right)\right\}$

M_c	Convective Mach number $\left\{M_c = \left(U^*_{0,US} - U^*_{0,LS}\right) / \left(c^*_{0,US} + c^*_{0,LS}\right)\right\}$
Ma	Mach number, defined as the speed of an objective relative to a fluid medium, divided by the speed of sound in that medium. $\left(Ma = u^*_r / c^*_r = u^*_r / \sqrt{\gamma R^* T^*_r}\right)$
Nu	Nusselt number, measuring the importance of convective heat transfer compared with conductive heat transfer. $\left(Nu = h^*_t D^*_d / k^*\right)$
Pr	Prandtl number, defined as the ratio of momentum diffusivity and thermal diffufisivity. $\left(Pr = \nu^* / \alpha^* = c^*_{p,g} \mu^* / k^*\right)$
Pr_t	SGS turbulent Prandtl number
Re	Reynolds number, defined as the ratio of inertial force to viscous force. $\left(Re = u^*_r l^*_r / \nu^*_r = \rho^*_r u^*_r l^*_r / \mu^*_r\right)$
Ri	Richardson number, defined as the ratio of buoyancy to inertial force. $\left\{Ri = (1-S)/S \bullet g^*_r l^*_r / u^{*2}_r = g'^*_r l^*_r / u^{*2}_r\right\}$
Sc	Schmidt number, defined as the ratio of momentum diffusivity and mass diffusivity. $\left\{Sc = \nu^* / D^* = \mu^* / \left(\rho^* D^*\right)\right\}$
Sc_t	SGS turbulent Schmidt number
Sh	Sherwood number, defined as the ratio of a characteristic lengthscale to the mass-diffusive boundary layer thickness. $\left(Sh = \beta^* D^*_d / D^*\right)$
Sr	Strouhal number – dimensionless frequency. $\left(Sr = f^* l^*_r / u^*_r\right)$
St	Stokes number, defined as the ratio of momentum response time of droplets to flow characteristic time. $\left\{St_0 = \tau^*_d / \tau^*_g = Re\, \rho_d D^2_d / (18\mu)\right\}$
Ze	Zel'dovich number – dimensionless activation energy for reaction. $\left\{Ze = E^*_a / \left(\bar{R}^* T^*_r\right)\right\}$

Greek symbols

α	Parameter controlling the filtering effect in compact filtering schemes; Thermal diffusivity
α_1, α_2	Subgrid terms in the energy equation
β	Overall mass transfer coefficient
γ	Specific heat ratio
δ_{ij}	Kronecker delta
δ_ω	Vorticity thickness
$\delta(x)$	Delta function
η	Subgrid species flux; Kolmogorov scale
ϑ	Momentum thickness
ϑ_1	Ratio of the constant-pressure heat capacity of gas to that of droplets
ϑ_2	Ratio of molecular weight of the gas phase to that of the vapour
λ	Disturbance wavelength
μ	Dynamic viscosity
μ_t	Turbulent dynamic viscosity
ν	Kinematic viscosity
ν_t	Turbulent Kinematic viscosity
ξ	Subgrid heat flux
Π_d	Second invariant of the deformation tensor (Squires & Eaton 1990)
ρ	Density
σ_{ij}	Viscous stress tensor
τ	Characteristic time scale
τ_{ij}	Subgrid stress tensor

τ_{kk}	Subgrid kinetic energy
υ	Stoichiometric coefficients for a reaction
χ	Scalar dissipation rate; Mole fraction of the vapour
$\dot{\omega}_i$	Mass production rate of species i
ω_T, RR	Reaction rate

Subscripts

0	Initial states
a	Free stream
atm	Atmosphere
av	Averaging zone
c	Convection
d	Droplet phase
eq	Equilibrium state
f	Fuel
far	Far field
g	Gas phase
i	i-th component (i = 1, 2, 3)
LS	Lower Stream of the temporal mixing layer
o	Oxidizer
p	Product
s, surf	Droplet surface
sat	Saturation state
sp	Sponge layer
st	Stoichiometric
US	Upper Stream of the temporal mixing layer

v	Liquid vapour
r	Reference quantities for nondimensionalization

Superscripts

*	Dimensional variables
′	First order derivative
′′	Second order derivative; Favre fluctuation $\left(f'' = f - \tilde{f}\right)$

Cap Symbols

“ $\dot{}$ ”	Time rate of change ($\partial/\partial t$)
“ $\bar{}$ ”	Reynolds averaging for DNS in Chapter IV; Normal filtering for LES in Chapters V and VI.
“ $\tilde{}$ ”	Favre averaging for DNS in Chapter IV; Favre filtering for LES in Chapters V and VI. $\left(\widetilde{f} = \overline{\rho_{\mathrm{g}} f} \big/ \overline{\rho_{\mathrm{g}}}\right)$
“ $\approx$ ”	Double tilde $\left(\widetilde{\widetilde{f}} = \overline{\overline{\rho_{\mathrm{g}} f}} \big/ \overline{\rho_{\mathrm{g}}}\right)$
“ $\frown$ ”	Functions based on known normal-filtered and Favre-filtered variables $\left\{\widehat{f} = f\left(\overline{\rho_{\mathrm{g}}}, \widetilde{f}_1, \cdots, \widetilde{f}_n\right)\right\}$
“ $\hat{}$ ”	Filtering based on the test filter volume; Compact filtering
“ $\widehat{\widehat{\ }}$ ”	Filtering operation defined as $\widehat{\widehat{f}} = \widehat{\overline{\rho_{\mathrm{g}} f}} \big/ \widehat{\overline{\rho_{\mathrm{g}}}}$

Miscellaneous

$\langle\ \rangle$	Reynolds averaging (= “ $\bar{}$ ”)
$\langle f \vert g \rangle$	Conditional averaging; Function f is averaged in the space of variable g.

Chapter I - Introduction

I.A Project Background

Multiphase reactive flows have been of theoretical and practical interest for a long time. Reaction due to the multiphase mixture of gas reactants and liquid water appears in a number of industrial combustors and domestic devices. In the field of fire suppression, the use of water mist to extinguish fires has received considerable interest since the banning of halogen-based agents for environment protection reasons (Tatem *et al.* 1994; Grant *et al.* 2000). In gas turbines, water or steam injection together with fuel has been used to control the NO_x formation since the 1960s (Jonsson & Yan 2005) and more recently as a part of the strategy to achieve zero-emission power plants (Richards *et al.* 2005). Another new development is the hybrid Solid-Oxide Fuel Cell (SOFC) gas turbine systems, in which the unspent exhaust fuel diluted in CO_2 and water steam from the SOFC is fed into the gas turbine combustor for further reactions to increase the overall rate of energy utilization (Kee *et al.* 2005).

Besides, spray combustion has attracted much attention due to the practical importance of enhancing the combustion efficiency and reducing the emission level in combustors such as internal combustion engines. Study of the relevant fundamental physics, however, is still in the infant stage (Réveillon & Vervisch 2000, 2005; Domingo *et al.* 2005).

Owing to the complex unsteady interactions among vortex dynamics, turbulent mixing, chemical reaction and evaporating droplets at vastly disparate spatial and temporal scales, a systematic understanding of such multiscale, multiphysics systems is still far from being achieved. The problem is also scientifically interesting and computationally challenging.

The present project therefore aims to obtain a better understanding of the complex physio-chemical phenomena linked to the local nonlinear interactions via high fidelity numerical techniques, and is only concerned with the gas-water reactive systems.

I.B Literature Review

In this overview, we focus on previous numerical studies. Relevant experimental studies will be referred to here and also throughout the course of the thesis.

I.B.1 Planar Jets

The free jet is an important prototype flow with a broad range of engineering applications. Although a common phenomenon in nature, it has taken researchers a long time to understand in depth its turbulent characteristics. Nowadays, it is widely adopted for fundamental studies of many important phenomena coupled with turbulence, such as jet flame, gas-solid or gas-liquid two-phase jet flows, *etc*. In the present study, a three-dimensional (3D) turbulent reactive jet laden with evaporating droplets serves as one of the basic physical models for investigating the interactions among turbulence, reaction and evaporation.

The planar jet has been extensively investigated in a series of experimental studies, in which the key parameters, *i.e.*, the jet spreading rate, mean velocity and Reynolds stress profiles, etc., have been measured (Gutmark & Wygnanski 1976; Ramaparian & Chandrasekhara 1985), and the near field vortex dynamics has been explored (Hussain & Clark 1977; Thomas & Chu 1989). On the other hand, numerical simulations of a planar jet with desirable accuracy in both space and time, *i.e.*, by Direct Numerical Simulation (DNS) or Large-Eddy Simulation (LES), have not yet been fully exploited. One of the main difficulties arises from the boundary conditions (BCs), especially at the outflow boundary, where the flow information outside the computational domain is completely unknown. Those boundary schemes based on the characteristic wave analysis (Thompson 1987, 1990; Poinsot & Lele 1992) are now recognized as a standard procedure to deal with this problem, although they

are far from perfect due to the assumption that the propagation of characteristic waves is one-dimensional. Artificial boundary conditions suitable for turbulent shear flows were reviewed by Colonius (2004) recently. While appropriate for inflow and radiation boundaries, the linearized BCs are often not accurate enough for outflow boundaries, where *ad hoc* approaches, like absorbing layers, are necessary. Besides, the inflow condition with properly preset turbulent properties is a prerequisite to simulate a "naturally" developed jet using DNS/LES. This is especially important in order to compare with the experimental data. Various methods have been proposed and tested (Stanley *et al*. 2002; Kempf *et al.* 2005; Kornev & Hassel 2007).

LES of a planar jet at both low and high Reynolds numbers, *i.e.*, Re=3000 and 30000, was performed by Le Ribault *et al.* (1999) using the standard Smagorinsky, dynamic Smagorinsky, and dynamic mixed models. Only the subgrid Reynolds stresses were modelled and all other subgrid terms were neglected. Through comparison with the experimental results for the jet half width, centreline velocity decay, mean velocity and turbulent intensities, and the analysis of key parameters of different subgrid scale (SGS) models, such as dynamic model coefficients and subgrid dissipation, it was concluded that the dynamic Smagorinsky model can fulfil the requirement for an economic but accurate LES. With the same physical parameters, a decent DNS was performed by Stanley *et al*. (2002) at Re=3000. It was claimed to be "the first computational study of spatially evolving three-dimensional planar turbulent jets utilizing direct numerical simulation". To trigger the turbulence generation in the near field, the divergence-free density, pressure and velocity fluctuation fields, the latter generated by a 3D energy spectrum characterizing isotropic turbulence, were imposed at the inflow plane. Comprehensive comparisons with experimental data were made for all the key jet parameters. Instantaneous flow structures were revealed by vorticity visualization, and the mixing process was studied through the evolution of a passive scalar. Akhavan *et al.* (2000) investigated the grid/subgrid scale (GS/SGS) interactions in a temporally evolving planar jet in both physical and spectral space using DNS and LES. A new SGS model is then designed based on the analysis. Da Silva & Métais (2002) analyzed the effects of large-scale coherent structures upon GS/SGS interactions based on filtered DNS results of a planar jet

at Re=3000 using *a priori* analysis. The contribution of each term of the transport equations for the GS and SGS kinetic energy was investigated both statistically and topologically. It was found that most of the interactions take place within or next to the vortex cores, not randomly distributed in space. Moreover, the local equilibrium assumption was found to be invalid due to the different locations of viscous dissipation of SGS kinetic energy and forward/backward GS/SGS energy transfer. Recently, the dominance of the two linearly unstable modes, *i.e.*, the sinuous and varicose modes, in the near field of a two-dimensional (2D) incompressible variable-density planar jet was revisited by Ravier *et al.* (2006) using DNS.

I.B.2 Buoyant Plumes

When the jet flow is subjected to a density or temperature difference from that of the ambient, the buoyancy force on the light or hot fluids becomes important or even dominant. The role played by buoyancy can be measured by the Froude (Fr) or Richardson (Ri) number, defined by the ratio of inertial force to the gravitational force. Accordingly, three different types of flow can be attained, *i.e.* $Fr << 1$, $Fr \sim 1$ or $Fr >> 1$.

O'Hern *et al.* (2005) measured in detail the mean and turbulent statistics of a turbulent round buoyant helium plume in both the Reynolds- and Favre-averaged framework. Desjardin *et al.* (2004) performed LES for the same plume. The fully dynamic subgrid models, which are quite similar to those adopted in the present study, revealed the transitional phenomenon close to the plume base impressively. Both the mean and Root-Mean-Square (RMS) properties of velocity and species concentration compared well with the experimental results of O'Hern *et al.* (2005). In both $Fr << 1$ plumes, the instability mechanism is introduced by the large density difference between the different species, *e.g.*, helium and air, and the buoyancy term is dominant compared to vortex stretching, which is the general vorticity production mechanism in non-buoyant flows.

In contrast, density variation can also be introduced by temperature difference between the jet core and the ambient flow with identical species. The oscillation behaviour in the near field of both heated round and planar air jets at $Ri << 1$ and $Re = 4000 \sim 5000$ was investigated by Monkewitz and co-workers (1990; 1993). Even though the effects of buoyancy is negligible compared to those of momentum due to the small Richardson numbers, global instability was found when the ratio of jet exit to ambient density falls below 0.7 for the round jet, and below 0.9 for the planar counterpart. The oscillations of velocity, temperature and pressure signals in the near field with regular frequency spectra become self-exited, despite the strictly controlled low turbulent intensity levels imposed at the inflow plane, and the large scale vortex structures appear much closer to the jet nozzle in comparison with high-Reynolds-number jets.

The final typical type of plume-related flow is characterised by $Fr \sim 1$, in which the momentum and buoyancy effects are competitive and consequently these are generally referred to as "forced plumes". The baroclinic torque, induced by misalignments of the density and pressure gradients, is another important mechanism for vorticity production, which may be of the same magnitude as the buoyancy term in the vorticity transport equation (Jiang & Luo 2000a). Luo and co-workers (Jiang & Luo 2000a, 2000b, 2001a, 2001b; Zhou *et al.* 2001a, 2001b, 2002) studied the vorticity dynamics, mixing and entrainment properties for both thermal and reactive plumes under various jet base configurations (*e.g.* circular or non-circular) with DNS and LES. In reactive plumes, the density inhomogeneity effects are amplified by combustion. The intricate interactions among instabilities, vortex dynamics, mixing, entrainment, turbulence and combustion through buoyancy in reactive plumes were investigated by Luo (2004). The common "puffing" or "flickering" phenomenon near the flame base was well captured and identified as the consequence of compound effects of buoyancy and baroclinic torque, which is in turn triggered by density inhomogeneity. The buoyancy instability is therefore a global, absolute instability. The higher entrainment rate in non-circular jets with higher aspect ratios was first explained by the extended Biot-Savart instability, *i.e.*, the vorticity along the major axis is larger than that along the minor axis, and this trend becomes stronger in jets with higher-aspect-ratio rectangular base configurations.

I.B.3 Non-Premixed Flames

Turbulent combustion problems are usually divided into two categories, *i.e.*, premixed and non-premixed flames, depending on whether or not fuel and oxidant are well mixed before reaction. Compared to premixed flames (Pope 1987), turbulent non-premixed flames (Bilger 1989) may be more difficult to understand and describe due to the molecular diffusion of reactants and simultaneous interaction with turbulence (Poinsot & Veynante 2005). A free jet flame is an ideal physical model for both experimental and numerical studies. An experimental database on simple jet flames, piloted jet flames, bluff body flames and swirl flames is being built and enlarged at Sandia National Laboratories (http://www.ca.sandia.gov/TNF/). Turbulent combustion models for both premixed and non-premixed flames based on the Reynolds Averaged Navier-Stokes (RANS) approach were reviewed by Veynante & Vervisch (2002). In theory, DNS is an ideal tool for accurate flame simulations, in which no physical models for turbulence and combustion are involved. However, its limitations are dictated by the capacities of present supercomputers. To fully resolve the turbulent and chemical scales, the product of Reynolds number by Damköhler number, measuring the ratio of typical turbulent to chemical time scales, must be less than a quantity related to the number of grid points (Poinsot & Veynante 2005). In this sense, the infinitely-fast-chemistry assumption or large Damköhler number in DNS should be used with caution. Under these circumstances, DNS is mainly used for flame simulations with extremely simple geometry configurations, model testing and validation for LES and RANS (Vervisch & Poinsot 1998).

Combining the advantage and discarding the disadvantage of DNS and RANS, LES has appeared as a promising tool for flame simulations in the last decade. The LES results of a turbulent non-premixed piloted jet flame, Sandia Flame D (Sheikhi *et al.* 2005) and Sydney bluff-body flame (Kempf *et al.* 2006) were reported recently, both reproducing the mean and rms experimental statistics quite well. Janicka & Sadiki (2005) systematically reviewed work on combustion-LES (CLES), showing that CLES was evolving into a powerful tool for the simulation of combustion systems of practical importance.

A common concern of the combustion community is the quality of LES. Since numerically filter width is typically coupled with grid spacing, a grid-independent LES solution is therefore difficult to determine (Janicka & Sadiki 2005). In this sense, to quantitatively measure the quality of LES results is not as straightforward as in DNS. Vreman (1995) designed a method to separate the numerical and model errors. Poinsot & Veynante (2005) have proposed a series of formula containing both resolved and modelled contributions when comparison against Reynolds- or Favre-averaged results is needed. Difficulties will emerge, however, if some quantities are not explicitly modelled in simulations, *e.g.*, the subgrid variance of a scalar field, *i.e.*, $\overline{\rho}\left(\widetilde{f^2}-\widetilde{f}^2\right)$. Pope (2004) suggested that at least 80% of the total turbulent kinetic energy (TKE) should be resolved for an adaptive LES, which puts a strict constraint on the grid spacing. The same issue was revisited by Klein (2005).

The modelling efforts for CLES are continuing. At present, most of the SGS combustion models originate from RANS. Generally speaking, two different classes of SGS combustion models are under development, *i.e.*, conserved scalar approach and direct closure approach. In the conserved scalar approach, the closure problem of the chemical source terms appeared in the energy and species equations is circumvented by introducing another conserved or passive scalar, mixture fraction, a measure of the local equivalence ratio. With infinitely-fast-chemistry assumption, all the species mass fractions and the temperature can be obtained if the mixture fraction is known, while for finite rate chemistry, another key parameter, scalar dissipation rate, is introduced, which controls mixing and determines the filtered reaction rate. The state relationships for the reactive scalars as functions of mixture fraction and scalar dissipation rate are provided by various models, *e.g.*, steady and unsteady flamelet models, flamelet/progress variable method, conditional moment closure, and transported FDF (Filtered Density Function) models (Pitsch 2006). In the direct closure approach, the filtered reaction rate, which is a nonlinear function of species mass fractions and temperature, is directly modelled. The simplest approach is to adopt the same form as in DNS, *i.e.*, neglecting the subfilter contributions. DesJardin & Frankel (1998) developed

scale similarity reaction rate models purely through filtering, and Luo (2004) extended their applications in modelling the filtered radiation source terms.

I.B.4 Two-Phase Flows

Numerical models for gas-solid or gas-liquid two-phase flows have developed along two parallel paths according to the manner in which the dispersed phase is treated (Crowe *et al.* 1996). In the two-fluid approach, the particle/droplet phase is assumed as a continuum and similar equations for mass, momentum and energy conservations as the fluid flow are built for particles/droplets based on the volume-averaged procedure. On the other hand, every particle/droplet possesses its own governing equations in the Lagrangian approach (Crowe *et al.* 1977), although the hypothesis of "computational particle/droplet", which represents a parcel of physical particles/droplets, must be made for some scenarios, in which the mass loading ratio (*MLR*) of the second phase is extremely high. With the development of computational facilities, the Lagrangian approach prevailed in the last two decades due to its more realistic representations of physical particles/droplets.

The interaction between the dispersed and carrier phase has received considerable interest due to its significance in industrial applications. The particle/droplet dispersion is controlled by the local velocity fluctuations due to turbulence and by the ordered motion of large-scale turbulent structures. For diluted two-phase flow, i.e., $MLR < 1\%$, the effects of particles/droplets on flow turbulence are generally ignored and one-way coupling algorithm is adopted. Tang *et al.* (1992) distinguished dramatically different dispersion behaviour of solid particles with different Stokes number in a spatially developing plane wake using a direct vortex method. Especially, the "preferential concentration" (Squires & Eaton 1991) of the $St=1$ particles was identified. Elghobashi & Truesdell (1992) performed DNS to investigate quantitatively the particle dispersion in a decaying isotropic turbulence using mean-square relative velocity, Lagrangian velocity autocorrelation, mean-square displacement and particle turbulent diffusivity, all of which are widely used in particle dispersion research.

As the *MLR* becomes higher, particles/droplets, in turn, can affect the turbulence either by increasing the turbulence energy or increasing the dissipation rate. The numerical methodology is referred to as "two-way coupling" if mutual interactions between the two phases are both accounted for. The pioneering work of turbulence modulation by particles can be traced back to Squires & Eaton (1990) and Elghobashi & Truesdell (1993), although a thorough understanding is still far from being achieved. A general criterion can be stated as: "small particles tend to attenuate the turbulence while larger particles augment the turbulence level" (Crowe *et al.* 1998). Diverse findings, however, often appear, possibly because the above conclusion was drawn in highly idealized homogeneous or isotropic turbulent flows. The physical mechanisms of turbulent modulation may change with the streamwise distance (Michioka *et al.* 2005), which can be only explored in realistic inhomogeneous multiphase turbulent flows. Other suggested criteria for the suppression and enhancement of turbulence (Crowe *et al.* 1998), based on: (i) the length scale ratio of particle diameter and characteristic size of turbulent eddy and (ii) relative particle Reynolds number, have been overthrown by a recent experimental study on a gas-particle pipe flow with various Reynolds numbers (Hadinoto *et al.* 2005).

The point-source approximation was adopted in all the above studies, *i.e.*, the particle size was assumed to be smaller than the Kolmogorov length scale. From the numerical point of view, this technique already involves a "subgrid" approximation (Boivin *et al.* 2000). To fully resolve the two-phase flow field, which becomes important when the particle size is comparable or bigger than the Kolmogorov length scale, the boundary layer adhered to the particle surface and wake effects need to be taken into consideration. Prohibited by extremely high computational cost required for, *e.g.*, moving boundaries and unstructured grid generation, the relevant research has been severely circumscribed. Burton & Eaton (2005) performed fully resolved simulations of the interaction between a fixed particle, whose size was approximately twice the size of the single-phase Kolmogorov length scale, and decaying homogeneous isotropic turbulence using an overlapping grid composed of a Cartesian background grid and a body-fitted spherical grid. A homogeneous flow field disturbed by solid particles was fully resolved by Kajishima (2004). In this scenario, the ratio of

particle diameter to grid spacing was ten, while the ratio of grid spacing to Kolmogorov length scale was two to four. Resorting to the immersed boundary methods (Mittal & Iaccarino 2005), the number of tracked particles was up to 2048.

For gas-liquid two-phase flows, the mutual interactions between the two phases become even more complicated due to the additional evaporating process, since the evaporated liquid vapour contributes to momentum/energy exchange and species redistribution. Research efforts on evaporating multiphase flows started to flourish in recent years. DNS was employed by Mashayek *et al.* (1997) to investigate dispersion of both non-evaporating and evaporating particles in dilute stationary isotropic incompressible turbulent flow with one-way coupling algorithm. Miller & Bellan (1999) performed DNS of a confined 3D temporal mixing layer laden with evaporating hydrocarbon droplets. Complete two-way couplings of mass, momentum and energy were taken into account. The liquid *MLR* was found to be the dominant parameter governing flow modulations, while variations in the initial Stokes number over the range $0.5 \leq St_0 \leq 2$ did not cause significant modulations of either first- or second-order gas phase statistics. Okong'o & Bellan (2004) did a detailed budget analysis for the complete filtered LES equations based on the DNS database of a droplet-laden temporal mixing layer. A simplified set of LES equations was then derived while keeping the leading order SGS terms. Constant coefficients for Smagorinsky, gradient and scale-similarity models were calibrated according to the filtered DNS results. In the LES study of a temporal mixing layer laden with evaporating droplets, Leboissetier *et al.* (2005) found that a 32-fold reduction in computational droplets compared to the number of physical drops can be used without degradation of accuracy, while a 64-fold reduction leads to a slight decrease in accuracy. DNS of two-phase spatial 3D laminar jets with different inlet geometric configurations was performed by Abdel-Hameed & Bellan (2002). It was found that the droplet source terms took the place of vortex stretching/tilting and turned into the crucial contributions for production of streamwise vorticity, one main source of enhancing entrainment. Moreover, for both the average and rms magnitudes of spanwise, streamwise vorticity and enstrophy, the difference between circular and noncircular two-phase jets is not as considerable as in single phase jets, further proving the main contribution for the vorticity genera-

tion and fine scale formation was from the momentum interaction with the drops. Furthermore, the axis-switching is no longer present in two-phase jets.

I.B.5 Multilateral Interactions

Inherent in multiphase reactive flows is the multilateral interactions among mixing, entrainment, turbulence, buoyancy, combustion, evaporation and the second dispersed phase, which opens up an extremely sophisticated but practically significant and scientifically interesting research area.

One main effect of turbulence on non-premixed combustion is to modify the flame structure by altering the local strain and twisting the flame surface (Tieszen 2001), which is contributed by buoyancy effects as well. In a DNS study of comparison between buoyant and non-buoyant flames, Elghobashi *et al.* (1999) found that the wrinkled buoyant flame surface reduced the distances between the isosurfaces of the mixture fraction F, thus augmenting the local ∇F and the scalar dissipation rate, and consequently the reaction rate. All these mutual interactions are bidirectional. In a DNS study of supersonic partially premixed diffusion flame by Luo (1999), the pressure-strain term was found to be a key parameter in both the Reynolds stress and TKE budgets, which helps to transfer energy from the streamwise to the transverse and spanwise directions, thus reducing anisotropy, and convert chemical energy into turbulence energy, *i.e.*, combustion-generated turbulence. Meanwhile, the buoyancy effect is magnified by combustion, together with dilatation, a sink term in the vorticity transport equation, and high viscosity in high temperature regions. Since combustion produces baroclinic torque, dilatation and broadened viscous diffusion, the vorticity and, in turn, the turbulence level could be either strengthened or weakened (Tieszen 2001). The augmented molecular viscosity also tends to decrease the local Reynolds number, thus modifying mixing and impacting the large scales of turbulence, which control entrainment, couple tightly with the buoyancy effects and determine the small-scale environment where mixing and combustion ultimately occur (Dimotakis 2005).

As stated in Section I.B.4, in two-phase flows, the particle/droplet dispersion is controlled by the local velocity fluctuations due to turbulence and by the ordered motion of large-scale turbulent structures, while particles/droplets can affect the turbulence either by increasing the turbulence energy or increasing the dissipation rate (Crowe *et al.* 1996). If the dispersed phase is evaporative, the liquid vapour will contribute to both momentum and energy exchange with the carrier phase, and redistribute the gas mixture species, an important mechanism for combustion control besides the cooling effects of droplets. As pointed out by Abdel-Hameed & Bellan (2002), the droplet source term took the place of vortex stretching/tilting term and became the dominant contribution in the vorticity transport equation.

Very few studies have been done on the interaction mechanism in evaporating multiphase reactive flows, in which all the above coupling coexists. Recently, DNS of a spatially developing reactive planar mixing layer has been performed to study the effects of fine solid particles on flow turbulence with the assumption of no temperature variation (Michioka *et al.* 2005). The effects of turbulence on vaporization, mixing and combustion of liquid-fuel sprays were investigated using the RANS approach by Sadiki *et al.* (2005).

I.C Organization of the Thesis

This thesis is organized as follows: Chapter II presents the DNS/LES governing equations for both the gas and droplet phases, in Eulerian and Lagrangian frames, respectively, and the dynamic subgrid models for the flow terms and the scale similarity model for the reaction term adopted in this study. The derivation of the governing equations for evaporating two-phase reactive flows is shown in the Appendix. Chapter III shows the numerical details for both phases, including the spatial and temporal discretizations, the compact filter scheme, the interpolation formula and the boundary condition schemes, followed by the parallel algorithm designed for the two-phase flow simulations. DNS is performed to investigate the droplet effects on a 3D temporal reacting shear layer in Chapter IV. Chapters V and VI present the LES study of two simplified realistic applications of multiphase reacting flows.

They are, respectively, a 3D turbulent reacting jet diluted with evaporating droplets and a 3D turbulent reacting plume suppressed by water droplets. The interactions among turbulence, combustion and evaporating droplets under various initial Stokes numbers (St_0) and mass loading ratios (MLR_0) are investigated using both instantaneous and statistical analysis. Finally, a summary of the thesis and the recommendation for future work are given in Chapter VII.

Chapter II – Mathematical Formulations

II.A Governing Equations

II.A.1 The Gas Phase

The reacting flow field is described with the compressible time-dependant Navier-Stokes equations together with chemical species transport equations, in both of which the coupling terms due to the chemical reaction and dispersed phase are taken into account. The detailed derivation of the governing equations for multiphase reactive flows can be found in the Appendix. For completeness, they are rewritten here as

(1) Mass Conservation:

$$\frac{\partial \rho_{\mathrm{g}}^{*}}{\partial t^{*}}+\frac{\partial\left(\rho_{\mathrm{g}}^{*} u_{\mathrm{g},i}^{*}\right)}{\partial x_{i}^{*}}=S_{\mathrm{ms}}^{*} \tag{II.1}$$

(2) Momentum Conservation:

$$\frac{\partial\left(\rho_{\mathrm{g}}^{*} u_{\mathrm{g},i}^{*}\right)}{\partial t^{*}}+\frac{\partial}{\partial x_{j}^{*}}\left(\rho_{\mathrm{g}}^{*} u_{\mathrm{g},i}^{*} u_{\mathrm{g},j}^{*}+p^{*} \delta_{ij}-\sigma_{ij}^{*}\right)+\left(\rho_{\mathrm{a}}^{*}-\rho_{\mathrm{g}}^{*}\right) g_{i}^{*}=S_{\mathrm{mo},i}^{*} \tag{II.2}$$

(3) Energy Conservation:

$$\frac{\partial E_{\mathrm{T}}^{*}}{\partial t^{*}}+\frac{\partial\left\{\left(E_{\mathrm{T}}^{*}+p^{*}\right) u_{\mathrm{g},i}^{*}+q_{i}^{*}-u_{\mathrm{g},j}^{*} \sigma_{ij}^{*}\right\}}{\partial x_{i}^{*}}+\left(\rho_{\mathrm{a}}^{*}-\rho_{\mathrm{g}}^{*}\right) g_{i}^{*} u_{\mathrm{g},i}^{*}=-\sum_{n=1}^{N_{\mathrm{s}}} \Delta h_{\mathrm{f},n}^{0,*} \dot{\omega}_{n}^{*}+S_{\mathrm{en}}^{*} \tag{II.3}$$

(4) Species Conservation:

$$\frac{\partial\left(\rho_{\mathrm{g}}^{*} Y_{n}\right)}{\partial t^{*}}+\frac{\partial\left(\rho_{\mathrm{g}}^{*} Y_{n} u_{\mathrm{g},i}^{*}\right)}{\partial x_{i}^{*}}-\frac{\partial}{\partial x_{i}^{*}}\left(\rho_{\mathrm{g}}^{*} D^{*} \frac{\partial Y_{n}}{\partial x_{i}^{*}}\right)=\dot{\omega}_{n}^{*} \tag{II.4}$$

$$\frac{\partial\left(\rho_{\mathrm{g}}^{*}Y_{\mathrm{v}}\right)}{\partial t^{*}}+\frac{\partial\left(\rho_{\mathrm{g}}^{*}Y_{\mathrm{v}}u_{\mathrm{g},i}^{*}\right)}{\partial x_{i}^{*}}-\frac{\partial}{\partial x_{i}^{*}}\left(\rho_{\mathrm{g}}^{*}D^{*}\frac{\partial Y_{\mathrm{v}}}{\partial x_{i}^{*}}\right)=S_{\mathrm{ms}}^{*} \tag{II.5}$$

where the total energy per unit volume

$$E_{\mathrm{T}}^{*}=\rho_{\mathrm{g}}^{*}\left(e_{\mathrm{g}}^{*}+\frac{u_{\mathrm{g},i}^{*}u_{\mathrm{g},i}^{*}}{2}\right) \tag{II.6}$$

The internal energy per unit mass including the contribution of the vapour from the liquid droplets reads

$$e_{\mathrm{g}}^{*}=c_{\mathrm{v,g}}^{*}T_{\mathrm{g}}^{*}+Y_{\mathrm{v}}h_{\mathrm{v}}^{0^{*}} \tag{II.7}$$

where h_{v}^{0} is the reference enthalpy for the vapour, the magnitude of which is taken to be same as the latent heat of evaporation, h_{fg}, in the present study. The shear stress tensor is defined by the Newtonian fluid assumption,

$$\sigma_{ij}^{*}=2\mu^{*}\left\{\frac{1}{2}\left(\frac{\partial u_{\mathrm{g},i}^{*}}{\partial x_{j}^{*}}+\frac{\partial u_{\mathrm{g},j}^{*}}{\partial x_{i}^{*}}\right)-\frac{1}{3}\delta_{ij}\frac{\partial u_{\mathrm{g},k}^{*}}{\partial x_{k}^{*}}\right\} \tag{II.8}$$

The molecular viscosity μ is assumed to follow a power law, *i.e.*,

$$\frac{\mu^{*}}{\mu_{\mathrm{r}}^{*}}=\left(\frac{T_{\mathrm{g}}^{*}}{T_{\mathrm{g,r}}^{*}}\right)^{0.76} \tag{II.9}$$

The heat flux vector follows the Fourier's law,

$$q_{i}^{*}=-k^{*}\frac{\partial T_{\mathrm{g}}^{*}}{\partial x_{i}^{*}} \tag{II.10}$$

The state relationship for ideal gas

$$p^{*}=\rho_{\mathrm{g}}^{*}R^{*}T_{\mathrm{g}}^{*} \tag{II.11}$$

is also needed to close the whole system. Equation (II.4) is solved for Y_{f}^{*} and Y_{o}^{*}, while $Y_{\mathrm{p}}^{*}=1-Y_{\mathrm{f}}^{*}-Y_{\mathrm{o}}^{*}-Y_{\mathrm{v}}^{*}$.

A few assumptions are made to simplify the calculations to be presented, while the key characteristics of the multiphase reactive flows are maintained simultaneously. These assumptions include:

(1) The Prandtl and Schmidt number are assumed to be constant (Eq. II.23), both of which are taken to be 0.7 in the present study, leading to a unity Lewis number.

(2) The molecular weights of different species are identical, which leads to the Frozen-Species State Equation (FSSE; Poinsot & Veynante 2005) (II.11).

(3) The heat flux due to species mass fraction gradients (*Dufour* effect) and the mass diffusion due to temperature gradients (*Soret* effect) are not considered in this study.

(4) Radiation is not modelled in the present study. The combustion parameters are selected to compensate for radiative heat loss, so that the peak temperature is in the range of typical small laboratory fires or flames.

In the context of simulating a non-premixed reactive jet laden with evaporating droplets (Chapter V) and a reacting plume suppressed by water droplets (Chapter VI), Eqs. (II.1)-(II.11) are normalized by the following reference quantities: (1) ρ_{r}^{*}: the ambient oxidant density; (2) u_{r}^{*}: the fuel jet velocity; (3) $p_{\mathrm{r}}^{*}=\rho_{\mathrm{r}}^{*}u_{\mathrm{r}}^{*2}$; (4) l_{r}^{*}: the jet slot nozzle width; (5) $t_{\mathrm{r}}^{*}=l_{\mathrm{r}}^{*}/u_{\mathrm{r}}^{*}$; (6) T_{r}^{*}: the environmental oxidant temperature; (7) $e_{\mathrm{r}}^{*}=h_{\mathrm{r}}^{*}=u_{\mathrm{r}}^{*2}$; (8) μ_{r}^{*}: the viscosity of the environmental oxidant. As for the temporal mixing layers studied in Chapter IV, the reference quantities are the same as above except that u_{r}^{*} is the velocity difference between the fuel and oxidizer streams ΔU_{0}^{*}, and l_{r}^{*} is the initial vorticity thickness $\delta_{\omega,0}^{*}$.

The final forms of the non-dimensional governing equations for both DNS and LES can be written as

$$\frac{\partial\overline{\rho_{\mathrm{g}}}}{\partial t}+\frac{\partial\left(\overline{\rho_{\mathrm{g}}}\widetilde{u_{\mathrm{g},i}}\right)}{\partial x_{i}}=\overline{S_{\mathrm{ms}}} \tag{II.12}$$

$$\frac{\partial\left(\overline{\rho_{\mathrm{g}}}\widetilde{u_{\mathrm{g},i}}\right)}{\partial t}+\frac{\partial}{\partial x_{j}}\left(\overline{\rho_{\mathrm{g}}}\widetilde{u_{\mathrm{g},i}}\widetilde{u_{\mathrm{g},j}}+\bar{p}\delta_{ij}-\widetilde{\sigma_{ij}}\right)+\frac{\left(\rho_{\mathrm{a}}-\overline{\rho_{\mathrm{g}}}\right)g_{i}}{Fr}=\overline{S_{\mathrm{mo},i}}+SG_{\mathrm{mo},i} \tag{II.13}$$

$$\frac{\partial \overline{E_{\mathrm{T}}}}{\partial t}+\frac{\partial}{\partial x_i}\left\{\left(\overline{E_{\mathrm{T}}}+\overline{p}\right)\widetilde{u_{\mathrm{g},i}}+\widehat{q_i}-\widetilde{u_{\mathrm{g},j}}\widehat{\sigma_{ij}}\right\}+\frac{\left(\rho_{\mathrm{a}}-\overline{\rho_{\mathrm{g}}}\right)\widetilde{u_{\mathrm{g},i}}g_i}{Fr}=Q_{\mathrm{h}}\overline{\omega_{\mathrm{T}}}+\overline{S_{\mathrm{en}}}+SG_{\mathrm{en}} \tag{II.14}$$

$$\frac{\partial\left(\overline{\rho_{\mathrm{g}}}\widetilde{Y_n}\right)}{\partial t}+\frac{\partial}{\partial x_i}\left\{\overline{\rho_{\mathrm{g}}}\widetilde{u_{\mathrm{g},i}}\widetilde{Y_n}-\frac{1}{ReSc}\left(\widehat{\mu}\frac{\partial\widetilde{Y_n}}{\partial x_i}\right)\right\}=-\upsilon_n W_n\overline{\omega_{\mathrm{T}}}+SG_{\mathrm{sp},n} \tag{II.15}$$

$$\frac{\partial\left(\overline{\rho_{\mathrm{g}}}\widetilde{Y_{\mathrm{v}}}\right)}{\partial t}+\frac{\partial}{\partial x_i}\left\{\overline{\rho_{\mathrm{g}}}\widetilde{u_{\mathrm{g},i}}\widetilde{Y_{\mathrm{v}}}-\frac{1}{ReSc}\left(\widehat{\mu}\frac{\partial\widetilde{Y_{\mathrm{v}}}}{\partial x_i}\right)\right\}=\overline{S_{\mathrm{ms}}}+SG_{\mathrm{sp,v}} \tag{II.16}$$

where

$$\overline{E_{\mathrm{T}}}=\overline{\rho_{\mathrm{g}}}\left(\widetilde{e_{\mathrm{g}}}+\frac{\widetilde{u_{\mathrm{g},i}}\widetilde{u_{\mathrm{g},i}}}{2}\right) \tag{II.17}$$

$$\widetilde{e_{\mathrm{g}}}=\frac{\widetilde{T_{\mathrm{g}}}}{\gamma(\gamma-1)Ma^2}+\widetilde{Y_{\mathrm{v}}}h_{\mathrm{v}}^0 \tag{II.18}$$

$$\widehat{\sigma_{ij}}=2\frac{\widehat{\mu}}{Re}\left\{\frac{1}{2}\left(\frac{\partial\widetilde{u_{\mathrm{g},i}}}{\partial x_j}+\frac{\partial\widetilde{u_{\mathrm{g},j}}}{\partial x_i}\right)-\frac{1}{3}\delta_{ij}\frac{\partial\widetilde{u_{\mathrm{g},k}}}{\partial x_k}\right\} \tag{II.19}$$

$$\widehat{\mu}=\widetilde{T}_{\mathrm{g}}^{0.76} \tag{II.20}$$

$$\widehat{q_i}=-\frac{\widehat{\mu}}{(\gamma-1)Ma^2PrRe}\frac{\partial\widetilde{T_{\mathrm{g}}}}{\partial x_i} \tag{II.21}$$

$$\overline{p}=\frac{\overline{\rho_{\mathrm{g}}}\widetilde{T_{\mathrm{g}}}}{\gamma Ma^2} \tag{II.22}$$

$$Re=\frac{\rho_{\mathrm{r}}^*u_{\mathrm{r}}^*l_{\mathrm{r}}^*}{\mu_{\mathrm{r}}^*};\ Ma=\frac{u_{\mathrm{r}}^*}{\sqrt{\gamma R^*T_{\mathrm{r}}^*}};\ Pr=\frac{c_{\mathrm{p,g}}^*\mu^*}{k^*};\ Sc=\frac{\mu^*}{\rho^*D^*};\ Fr=\frac{u_{\mathrm{r}}^{*2}}{g_{\mathrm{r}}^*l_{\mathrm{r}}^*} \tag{II.23}$$

For DNS, the subgrid terms $SG_{\mathrm{mo},i}$, SG_{en}, $SG_{\mathrm{sp},n}$ and $SG_{\mathrm{sp,v}}$ vanish, and all the cap symbols are not used; While for LES, $\overline{f}$ and $\widetilde{f}$ designate the normal and Favre filtering, defined as $\widetilde{f}=\overline{\rho_{\mathrm{g}}f}/\overline{\rho_{\mathrm{g}}}$, respectively, and $\widehat{f}$ is a composite variable evaluated with filtered quantities. The subgrid terms induced by $\overline{f}-\widehat{f}$ are ignored due to their secondary contributions

compared to those listed in Eqs. (II.13), (II.14), (II.15) and (II.16), which will be discussed in detail in Section (II.A.5).

II.A.2 The Reaction Scheme

Equations (II.1)-(II.5) can be used for a generalised multispecies, multistep reaction, while in the present study, an idealized one-step irreversible reaction,

$$\upsilon_{\mathrm{f}} F + \upsilon_{\mathrm{o}} O \rightarrow \upsilon_{\mathrm{p}} P \tag{II.24}$$

with finite-rate chemistry base on the Arrhenius law is employed for the chemical reaction. With properly calibrated parameters, the one-step irreversible Arrhenius kinetics with unity reaction order is capable of representing the main features of partially premixed hydrocarbon combustion (Fernández-Tarrazo *et al.* 2006). Of particular interest in this project is the effect of evaporating droplets on gas temperature and reaction rate, rather than detailed species diffusion, production and reduction required for the study of emission, justifying the choice of the simplified reaction scheme.

The normalized reaction rate ω_{T} in Eqs. (II.14) and (II.15) takes the following form (Luo 1999)

$$\omega_{\mathrm{T}} = Da \left(\frac{\rho_{\mathrm{g}} Y_{\mathrm{f}}}{W_{\mathrm{f}}} \right)^{\upsilon_{\mathrm{f}}} \left(\frac{\rho_{\mathrm{g}} Y_{\mathrm{o}}}{W_{\mathrm{o}}} \right)^{\upsilon_{\mathrm{o}}} \exp\left(-\frac{Ze}{T_{\mathrm{g}}} \right) \tag{II.25}$$

The highly nonlinear function $\omega_{\mathrm{T}}(Y_{\mathrm{f}}, Y_{\mathrm{o}}, T_{\mathrm{g}})$ poses a direct difficulty on the filtering operation in LES, which is circumvented in the conserved scalar approach (Pitsch 2006) by introducing a passive scalar, mixture fraction. For the finite-rate reaction scheme expressed by Eq. (II.25), to properly account for the SGS contribution is crucial for the filtered reaction rate $\overline{\omega_{\mathrm{T}}}$ required in the context of LES. However, to model the interaction between evaporating droplets, whose size is below the grid scale, and chemical reaction at the SGS level is challenging and still under development (Pera 2006). Moreover, the production of vapour impedes combustion and thus induces considerable flame quench. This is completely different from the situations in spray combustion, for which evaporation enhances combustion.

With these considerations, $\overline{\omega_{\mathrm{T}}}$ is directly modelled by the Scale Similarity Filtered Reaction Rate Model (SSFRRM) developed by DesJardin & Frankel (1998),

$$\overline{\omega_{\mathrm{T}}} = \overline{\omega_{\mathrm{T}}\left(\overline{\rho_{\mathrm{g}}}, \widetilde{T}_{\mathrm{g}}, \widetilde{Y}_{\mathrm{f}}, \widetilde{Y}_{\mathrm{o}}\right)} + K\left\{\overline{\overline{\omega_{\mathrm{T}}\left(\overline{\rho_{\mathrm{g}}}, \widetilde{T}_{\mathrm{g}}, \widetilde{Y}_{\mathrm{f}}, \widetilde{Y}_{\mathrm{o}}\right)}} - \overline{\omega_{\mathrm{T}}\left(\overline{\overline{\rho_{\mathrm{g}}}}, \widetilde{\widetilde{T}}_{\mathrm{g}}, \widetilde{\widetilde{Y}}_{\mathrm{f}}, \widetilde{\widetilde{Y}}_{\mathrm{o}}\right)}\right\} \quad \text{(II.26)}$$

where $\widetilde{\widetilde{f}}$ is computed as $\overline{\overline{\rho_{\mathrm{g}} f}} \big/ \overline{\rho_{\mathrm{g}}}$. The two terms on the RHS represent the grid scale (GS) and subgrid scale (SGS) contributions, respectively. It was found that for the GS part, the filtered resolved reaction rate $\overline{\omega_{\mathrm{T}}\left(\overline{\rho_{\mathrm{g}}}, \widetilde{T}_{\mathrm{g}}, \widetilde{Y}_{\mathrm{f}}, \widetilde{Y}_{\mathrm{o}}\right)}$ performed better than the resolved one $\omega_{\mathrm{T}}\left(\overline{\rho_{\mathrm{g}}}, \widetilde{T}_{\mathrm{g}}, \widetilde{Y}_{\mathrm{f}}, \widetilde{Y}_{\mathrm{o}}\right)$ in a 2D LES of non-premixed reactive jet (DesJardin & Frankel 1998). In this sense, a stabilization process has been included in this model (Poinsot & Veynante 2005). Ideally, the similarity constant K should incorporate length scale effects (Poinsot & Veynante 2005). In the present study, K is set to be 1 as in Kurose *et al.* (2001).

The non-dimensional heat release parameter Q_{h} in Eq. (II.14) is defined as

$$Q_{\mathrm{h}} = \upsilon_{\mathrm{f}} W_{\mathrm{f}} \Delta h^{0}_{\mathrm{f,f}} + \upsilon_{\mathrm{o}} W_{\mathrm{o}} \Delta h^{0}_{\mathrm{f,o}} - \upsilon_{\mathrm{p}} W_{\mathrm{p}} \Delta h^{0}_{\mathrm{f,p}} \quad \text{(II.27)}$$

for a one-step irreversible chemical reaction (II.24) (Luo 1999).

II.A.3 The Droplet Phase

The dispersed droplet phase is tracked in the Lagrangian frame, *i.e.*, every droplet possesses its own mass, momentum and energy equations. In comparison with the Eulerian method, the advantage of the Lagrangian method attributes mainly to its ability to provide detailed information on droplet-fluid interaction. Moreover, the models for the effective viscosity and thermal conductivity of the droplet phase are not required, and the boundary condition setting is straightforward. On the other hand, the capability of the Lagrangian method is compromised by the computational cost. It is necessary to trace a huge amount of droplets in the flow field to get meaningful statistical results for some scenarios (Sankaran & Menon 2002).

Several assumptions have been made to make the computations feasible:

(1) The volume fraction of the dispersed phase is negligible, *i.e.*, the two-phase flow is dilute;

(2) The dispersed phase is composed of discrete, non-connected and spherical droplets;

(3) The collisions, breakup and coalescence of droplets are ignored;

(4) Since the ratio of the continuous phase density to the droplet material density is very small, 10^{-3} in the present study, only the drag and gravitational force are retained in the Basset-Boussinesq-Oseen (BBO) equation for droplet motion.

The derivation of the governing equations for the droplet phase using the Reynolds Transport Theorem can be found in Crowe et al. (1998) and are not repeated here. They are summarized as follows,

(1) Mass Conservation:

$$\dot{m}_{\mathrm{d}}^{*} \equiv \frac{dm_{\mathrm{d}}^{*}}{dt^{*}} = -Sh\pi D_{\mathrm{d}}^{*}\rho_{\mathrm{g}}^{*}D^{*}H_{\mathrm{M}} = -\frac{1}{3}\frac{Sh}{Sc}\frac{m_{\mathrm{d}}^{*}}{\tau_{\mathrm{d}}^{*}}H_{\mathrm{M}} \tag{II.28}$$

(2) Momentum Conservation:

$$\frac{dv_{\mathrm{d},i}^{*}}{dt^{*}} = \frac{F_{\mathrm{drag},i}^{*}}{m_{\mathrm{d}}^{*}} + g_{i}^{*} = \frac{f}{\tau_{\mathrm{d}}^{*}}\left(u_{\mathrm{g},i}^{*} - v_{\mathrm{d},i}^{*}\right) + g_{i}^{*} \tag{II.29}$$

(3) Energy Conservation:

$$m_{\mathrm{d}}^{*}c_{\mathrm{d}}^{*}\frac{dT_{\mathrm{d}}^{*}}{dt^{*}} = h_{\mathrm{t}}^{*}A_{\mathrm{d}}^{*}\left(T_{\mathrm{g}}^{*} - T_{\mathrm{d}}^{*}\right) + \frac{dm_{\mathrm{d}}^{*}}{dt^{*}}h_{\mathrm{fg}}^{*} \tag{II.30}$$

$$\Rightarrow \frac{dT_{\mathrm{d}}^{*}}{dt^{*}} = \frac{1}{3\tau_{\mathrm{d}}^{*}}\left\{\frac{Nu}{Pr}\theta_{1}\left(T_{\mathrm{g}}^{*} - T_{\mathrm{d}}^{*}\right) - \frac{Sh}{Sc}\frac{h_{\mathrm{fg}}^{*}}{c_{\mathrm{d}}^{*}}H_{\mathrm{M}}\right\} \tag{II.31}$$

where the Sherwood and Nusselt number are defined as

$$Sh = 2.0 + 0.552Re_{\mathrm{d}}^{1/2}Sc^{1/3} \tag{II.32}$$

$$Nu = \frac{h_{\mathrm{t}}^{*}D_{\mathrm{d}}^{*}}{k^{*}} = 2.0 + 0.552Re_{\mathrm{d}}^{1/2}Pr^{1/3} \tag{II.33}$$

The droplet Reynolds number, Re_{d}, is

$$Re_{\mathrm{d}} = \frac{\rho_{\mathrm{g}}^{*} \left| \mathbf{u}_{\mathrm{g}}^{*} - \mathbf{v}_{\mathrm{d}}^{*} \right| D_{\mathrm{d}}^{*}}{\mu^{*}} = Re \frac{\rho_{\mathrm{g}} \left| \mathbf{u}_{\mathrm{g}} - \mathbf{v}_{\mathrm{d}} \right| D_{\mathrm{d}}}{\mu} \tag{II.34}$$

The characteristic responsive time of droplets, τ_{d}^{*}, is

$$\tau_{\mathrm{d}}^{*} = \frac{\rho_{\mathrm{d}}^{*} D_{\mathrm{d}}^{*2}}{18\mu^{*}} \tag{II.35}$$

The Stokes drag exerted on droplets, $F_{\mathrm{drag},i}^{*}$, is

$$F_{\mathrm{drag},i}^{*} = -\frac{1}{2} C_{\mathrm{D}} A_{\mathrm{d}}^{*} \rho_{\mathrm{g}}^{*} \left(v_{\mathrm{d},i}^{*} - u_{\mathrm{g},i}^{*} \right) \left| \mathbf{v}_{\mathrm{d}}^{*} - \mathbf{u}_{\mathrm{g}}^{*} \right| = f \frac{m_{\mathrm{d}}^{*}}{\tau_{\mathrm{d}}^{*}} \left(u_{\mathrm{g},i}^{*} - v_{\mathrm{d},i}^{*} \right) \tag{II.36}$$

The correction coefficient to Stokes drag, f, is

$$f = 1 + 0.15 Re_{\mathrm{d}}^{0.687} \tag{II.37}$$

which is reasonably good for Re_{d} up to 800 (Crowe *et al.* 1998).

The droplet evaporation is described by the classical rapid mixing model (Spalding 1953). The non-equilibrium effect was found significant when the initial droplet size is very small ($D_{\mathrm{d},0}^{*}$ <50 μm) (Miller *et al.* 1998) in high-temperature environments and thus is not accounted for in the present study. Other advanced evaporation models (Miller *et al.* 1998; Sazhin 2006) are not considered because of the extra computational cost.

The specific driving potential for mass transfer, H_{M}, is

$$H_{\mathrm{M}} = \ln\left(1 + B_{\mathrm{M,eq}}\right) \tag{II.38}$$

The equilibrium Spalding transfer number for mass, $B_{\mathrm{M,eq}}$, is

$$B_{\mathrm{M,eq}} = \frac{Y_{\mathrm{s,eq}} - Y_{\mathrm{v}}}{1 - Y_{\mathrm{s,eq}}} \tag{II.39}$$

The mass fraction of the vapour at the droplet surface, $Y_{\mathrm{s,eq}}$, is

$$Y_{\mathrm{s,eq}} = \frac{\chi_{\mathrm{s,eq}}}{\chi_{\mathrm{s,eq}} + \left(1 - \chi_{\mathrm{s,eq}}\right)\theta_2} \tag{II.40}$$

The surface equilibrium mole fraction of the vapour, $\chi_{s,eq}$, is given by the Clausius-Clapeyron equation,

$$\chi_{s,eq} = \frac{p^*_{sat}}{p^*} = \frac{p^*_{atm}}{p^*} \exp\left\{ \frac{h^*_{fg}}{\bar{R}^* / W^*_v} \left(\frac{1}{T^*_B} - \frac{1}{T^*_d} \right) \right\} \tag{II.41}$$

With the same reference quantities for the gas phase equations, the normalized droplet equations can be expressed as

$$\dot{m}_d \equiv \frac{dm_d}{dt} = -\frac{1}{3} \frac{Sh}{Sc} \frac{m_d}{St} H_M \tag{II.42}$$

$$\frac{dv_{d,i}}{dt} = \frac{F_{drag,i}}{m_d} + \frac{g_i}{Fr} = \frac{f}{St} \left(u_{g,i} - v_{d,i} \right) + \frac{g_i}{Fr} \tag{II.43}$$

$$\frac{dT_d}{dt} = \frac{\theta_1}{3St} \left\{ \frac{Nu}{Pr} \left(T_g - T_d \right) - (\gamma - 1) Ma^2 \frac{Sh}{Sc} H_M h_{fg} \right\} \tag{II.44}$$

where the Stokes number is defined as the ratio between the characteristic droplet and flow time scale, *i.e.*,

$$St = \frac{\tau^*_d}{\tau^*_g} = Re \tau_d = Re \frac{\rho_d D_d^2}{18 \mu} \tag{II.45}$$

The non-dimensional Stokes drag force, $F_{drag,i}$, can be written as

$$F_{drag,i} = f \frac{m_d}{St} \left(u_{g,i} - v_{d,i} \right) \tag{II.46}$$

The normalized Clausius-Clapeyron equation reads

$$\chi_{s,eq} = \frac{p_{sat}}{p} = \frac{p_{atm}}{p} \exp\left\{ \frac{\gamma Ma^2}{\theta_2} h_{fg} \left(\frac{1}{T_B} - \frac{1}{T_d} \right) \right\} \tag{II.47}$$

A parcel of physical droplets is represented by one computational droplet in LES to reduce the computational cost. The same equations, (II.42)-(II.44), are employed for the computational droplets. Since only the GS variables are known, a key issue in the framework of LES of two-phase flows is how to obtain the fully resolved gas phase properties at the droplet locations, as demanded by Eqs. (II.42)-(II.44). The SGS contributions are consid-

ered to be especially important for small droplets. The same issue will be confronted as the filtered droplet source terms, $\overline{S_{\text{ms}}}$, $\overline{S_{\text{mo},i}}$ and $\overline{S_{\text{en}}}$, on the RHS of Eqs. (II.12), (II.13), (II.14) and (II.16), are evaluated. A detailed discussion on this respect can be found in the following section.

II.A.4 The Droplet Source Terms

The detailed derivation of the coupling terms, S^*_{ms}, $S^*_{\text{mo},i}$ and S^*_{en}, on the RHS of Eqs. (II.1), (II.2), (II.3) and (II.5) due to the kinetic and thermodynamic effects of droplets on the carrier phase can be found in the Appendix. They are rewritten here as follows,

$$S^*_{\text{ms}} = -\frac{1}{V^*}\sum_k \dot{m}^*_{\text{d},k} \tag{II.48}$$

$$S^*_{\text{mo},i} = -\frac{1}{V^*}\sum_k \left(F^*_{\text{drag},k,i} + \dot{m}^*_{\text{d},k} v^*_{\text{d},k,i} \right) \tag{II.49}$$

$$S^*_{\text{en}} = -\frac{1}{V^*}\sum_k \left\{ \begin{array}{l} h^*_{\text{t},k} A^*_{\text{d},k} \left(T^*_{\text{g},k} - T^*_{\text{d},k} \right) + \dot{m}^*_{\text{d},k} h^*_{\text{fg}} + F^*_{\text{drag},k,i} v^*_{\text{d},k,i} + \\ \dot{m}^*_{\text{d},k} c^*_{\text{d}} T^*_{\text{d},k} + \frac{1}{2}\dot{m}^*_{\text{d},k} v^*_{\text{d},k,i} v^*_{\text{d},k,i} \end{array} \right\} \tag{II.50}$$

while the normalized source terms take the following forms,

$$S_{\text{ms}} = -\frac{1}{V}\sum_k \dot{m}_{\text{d},k} \tag{II.51}$$

$$S_{\text{mo},i} = -\frac{1}{V}\sum_k \left(F_{\text{drag},k,i} + \dot{m}_{\text{d},k} v_{\text{d},k,i} \right) \tag{II.52}$$

$$\begin{aligned} S_{\text{en}} = -\frac{1}{V}\sum_k \Bigg\{ & \frac{1}{3}\frac{Nu}{(\gamma-1)Ma^2 Pr}\frac{m_{\text{d},k}}{St_k}\left(T_{\text{g},k} - T_{\text{d},k} \right) + F_{\text{drag},k,i} v_{\text{d},k,i} \\ & + \frac{1}{\theta_1(\gamma-1)Ma^2}\dot{m}_{\text{d},k} T_{\text{d},k} + \dot{m}_{\text{d},k} h_{\text{fg}} + \frac{1}{2}\dot{m}_{\text{d},k} v_{\text{d},k,i} v_{\text{d},k,i} \Bigg\} \end{aligned} \tag{II.53}$$

S_{ms}, $S_{\text{mo},i}$ and S_{en} represent the rate of change of mass, momentum and total energy of droplets. In Eq. (II.53), the first and fourth terms in the bracket are due to the convective heat exchange rate between the two phases and the latent heat portion needed to drive

evaporation, which combine to represent the rate of change of the internal energy of droplet; The second term is owing to the rate of change of the kinetic energy of droplet; The third and final terms come from the initial internal and kinetic energy of droplet which is transferred into the gas phase after it evaporates.

In the context of LES, the filtered source terms, $\overline{S}$, need to be evaluated. First, it is necessary to clarify the mathematical definition of the filtering operation on a discrete function S in the filtering volume V_f, which is given by Okong'o & Bellan (2004) as follows:

$$\overline{S(\mathbf{x})}=\int_{V_\mathrm{f}} S_\mathrm{d}\delta(\mathbf{y}-\mathbf{X})G(\mathbf{x}-\mathbf{y})d\mathbf{y} \tag{II.54}$$

where $S_\mathrm{d}\delta(\mathbf{y}-\mathbf{X})$ is the point-source contribution from the droplet and δ is the delta function. If G is a top-hat filter, as in the present study, then

$$\overline{S}=\frac{1}{V_\mathrm{f}}\sum_k S_{\mathrm{d},k} \tag{II.55}$$

It is noteworthy that $\overline{S}$ is not obtained by directly filtering the DNS source terms S_ms, $S_{\mathrm{mo},i}$ and S_en. Consequently, the only difference between S in DNS and $\overline{S}$ in LES exists in the local discretization volume, which is the grid cell volume, V, in DNS while filtering volume, V_f, in LES. However, the unfiltered variables of the gas phase, such as $u_{\mathrm{g},i}$, $T_{\mathrm{g},i}$, $Y_{\mathrm{v},i}$, *etc.*, are not available in LES and must be modelled from the GS flow field, which is generally referred to as a "deconvolution" procedure (Ferziger & Peric 2004). The prerequisite to make the "point-source" approximation (Boivin *et al.* 1998), which has been adopted in most of the DNS/LES studies of two-phase flows as well as in the present study, is that the particle/droplet size is comparable to or even less than the Kolmogorov scale, so the interaction between the two phases is expected to be active within the SGS range, *i.e.*, the SGS effects on the dispersed phase is considered to be crucial. At present, most of the modelling efforts on this respect have been focused on incompressible gas-solid two-phase flows (Yuu *et al.* 2001; Segura *et al.* 2004; Kuerten & Vreman 2005; Shotorban & Mashayek 2005), in which only the reconstruction of flow velocities is of concern. The SGS velocity was modelled through purely mathematical manipulation by Yuu *et al.* (2001), Kuerten & Vreman (2005)

and Shotorban & Mashayek (2005), while Segura *et al.* (2004) inherited the modelling strategy from the RANS approach (Faeth 1987), *i.e.*, the SGS turbulence is assumed to be isotropic and the SGS velocity component is generated by a random number sampled from a zero-mean Gaussian Probability Density Function (PDF). The same method was employed by Sankaran & Menon (2002) for the SGS velocity reconstruction in LES of spray combustion in swirling flows, while the SGS thermodynamic quantities were left unmodelled. All these SGS quantities are, however, important to properly reflect the kinetic and thermodynamic behaviours of droplets in LES of gas-liquid two-phase reactive flows. In an *a priori* analysis with DNS results of a droplet-laden temporal mixing layer, Miller & Bellan (2000) extended the Gaussian subgrid PDF method to all the SGS quantities. Unfortunately, the filtered DNS results revealed that the Y_v subgrid PDF deviated substantially from the standard Gaussian distribution. Encouraging results emerged after a deterministic model was designed by Okong'o & Bellan (2004). However, in the subsequent *a posteriori* LES of the same droplet-laden temporal mixing layer by Leboissetier *et al.* (2005) and a droplet-laden spatial jet by Leboissetier *et al.* (2004), this model was not adopted due to the concern of unpredicted model errors. It is worth noting that Okong'o & Bellan (2004) found the baseline model, in which the SGS effects are neglected, performed better than the random model based on the Gaussian subgrid PDF. Under such circumstances, it was decided in the present study to use the filtered flow field in place of the unfiltered flow field in calculating the source terms, amounting to neglecting the direct SGS effects on droplet evolution, as done by Boivin *et al.* (2000), Yamamoto *et al.* (2001), Leboissetier *et al.* (2004) and Leboissetier *et al.* (2005).

II.A.5 The Subgrid Terms

II.A.5-a Subgrid Terms

In LES, filtering operations produce the subgrid terms, which must be modelled. The subgrid terms $SG_{mo,i}$ in Eq. (II.13), SG_{en} in Eq. (II.14), $SG_{sp,n}$ in Eq. (II.15) and $SG_{sp,v}$ in Eq. (II.16) are defined as

$$SG_{\mathrm{mo},i} = -\frac{\partial\left(\overline{\rho}_{\mathrm{g}}\tau_{ij}\right)}{\partial x_j} \tag{II.56}$$

$$SG_{\mathrm{en}} = -\alpha_1 - \alpha_2 = -\widetilde{u}_{\mathrm{g},i}\frac{\partial\left(\overline{\rho}_{\mathrm{g}}\tau_{ij}\right)}{\partial x_j} - \frac{1}{\gamma(\gamma-1)Ma^2}\frac{\partial\left(\overline{\rho}_{\mathrm{g}}\xi_j\right)}{\partial x_j} \tag{II.57}$$

$$SG_{\mathrm{sp},k} = -\frac{\partial\left(\overline{\rho}_{\mathrm{g}}\eta_{j,k}\right)}{\partial x_j} \tag{II.58}$$

respectively, where the subgrid stress tensor τ_{ij} is

$$\tau_{ij} = \widetilde{u_{\mathrm{g},i}u_{\mathrm{g},j}} - \widetilde{u}_{\mathrm{g},i}\widetilde{u}_{\mathrm{g},j} \tag{II.59}$$

The subgrid heat flux ξ_j is

$$\xi_j = \widetilde{u_{\mathrm{g},j}T_{\mathrm{g}}} - \widetilde{u}_{\mathrm{g},j}\widetilde{T}_{\mathrm{g}} \tag{II.60}$$

The subgrid species flux $\eta_{j,k}$ is

$$\eta_{j,k} = \widetilde{u_{\mathrm{g},j}Y_k} - \widetilde{u}_{\mathrm{g},j}\widetilde{Y}_k \tag{II.61}$$

It is well recognized that the subgrid fluxes τ_{ij}, ξ_j and $\eta_{j,k}$ are the main subgrid contributions to the momentum, energy and species equations. The derivation of the filtered energy equation follows the same manipulations done by Vreman (1995), leading to six subgrid terms in total. Besides the subgrid heat flux term α_2, α_1 represents the kinetic energy transfer from resolved to subgrid scales, and is therefore considered to be important and kept in Eq. (II.57). The subgrid viscous dissipation term α_4,

$$\alpha_4 = \overline{\sigma_{ij}\frac{\partial u_{\mathrm{g},i}}{\partial x_j}} - \overline{\sigma}_{ij}\frac{\partial \widetilde{u}_{\mathrm{g},i}}{\partial x_j} \tag{II.62}$$

is physically important for high-Reynolds-number flows and generally modelled by a calibrated ratio between the cube of the SGS velocity scale and a length scale, *e.g.*, the filter width, or based on the scale similarity hypothesis (Vreman *et al.* 1995). The calibrated model coefficients obtained by Martin *et al.* (2000) for a homogeneous isotropic turbulence is much lower than those by Vreman *et al.* (1995) for a compressible mixing layer. Martin *et*

al. (2000) thus suggested that dynamic procedures are generally needed to accurately predict the contribution of α_4. Ghosal *et al.* (1995) argued that the standard Germano Identity methodology is not suitable for α_4, which takes effects predominantly at small scales. A dynamic model is then developed for generalized inhomogeneous turbulent flows. An additional transport equation for subgrid kinetic energy, however, is needed to be solved. Vreman (1995) proposed a dynamic procedure which is based on the global balance of the integrated subgrid kinetic energy equation. As a consequence, the model coefficient depends on time only, which can be generally referred to as a "semi-dynamic" coefficient. These sort of dynamic models are believed to be suitable only for temporally developing flows (Vreman 1995; Lenormand *et al.* 2000; Gago *et al.* 2003). For spatially developing flows as in the present study, a model coefficient with no variation on space is far from being satisfactory. Under these circumstances, the subgrid dissipation term α_4 is not explicitly modelled in the present study of turbulent flows at an intermediate Reynolds number (4000), as in Zhou *et al.* (2001a) and Larchevêque *et al.* (2003).

All the other subgrid terms are ignored due to their secondary contributions compared to those enumerated in Eqs. (II.56), (II.57) and (II.58).

II.A.5-b Subgrid Models

The subgrid stress tensor τ_{ij} is modelled by Smagorinsky (1963),

$$\overline{\rho}_{\mathrm{g}}\left(\tau_{ij}-\frac{\delta_{ij}}{3}\tau_{kk}\right)\simeq-2\overline{\rho}_{\mathrm{g}}\nu_{\mathrm{t}}\left(\widehat{S_{ij}}-\frac{\delta_{ij}}{3}\widehat{S_{kk}}\right)=-2\overline{\rho}_{\mathrm{g}}C_{\mathrm{d}}\overline{\Delta}^{2}\left|\widehat{S}\right|\left(\widehat{S_{ij}}-\frac{\delta_{ij}}{3}\widehat{S_{kk}}\right) \quad \text{(II.63)}$$

the subgrid kinetic energy τ_{kk} by Yoshizawa model (Yoshizawa 1986),

$$\overline{\rho}_{\mathrm{g}}\tau_{kk}\simeq 2\overline{\rho}_{\mathrm{g}}C_{\mathrm{I}}\overline{\Delta}^{2}\left|\widehat{S}\right|^{2} \quad \text{(II.64)}$$

and the subgrid heat flux ξ_j and species flux $\eta_{j,k}$ by eddy-diffusivity models (Moin *et al.* 1991)

$$\overline{\rho}_{\mathrm{g}}\xi_{j}\simeq-\frac{\overline{\rho}_{\mathrm{g}}\nu_{\mathrm{t}}}{Pr_{\mathrm{t}}}\frac{\partial\widetilde{T}_{\mathrm{g}}}{\partial x_{j}}=-\overline{\rho}_{\mathrm{g}}C_{\mathrm{T}}\overline{\Delta}^{2}\left|\widehat{S}\right|\frac{\partial\widetilde{T}_{\mathrm{g}}}{\partial x_{j}} \quad \text{(II.65)}$$

$$\overline{\rho_{\mathrm{g}}}\eta_{j,k} \simeq -\frac{\overline{\rho_{\mathrm{g}}}\nu_{\mathrm{t}}}{Sc_{\mathrm{t},k}}\frac{\partial \widetilde{Y_k}}{\partial x_j} = -\overline{\rho_{\mathrm{g}}}C_{Y_k}\overline{\Delta}^2\left|\widetilde{S}\right|\frac{\partial \widetilde{Y_k}}{\partial x_j} \tag{II.66}$$

II.A.5-c Model Coefficients

All the model coefficients C_{d}, C_{I}, C_{T} and C_{Y_k} are dynamically determined during the course of simulations based on the Germano Identity (GI) procedure designed by Germano *et al.* (1991) and later extended by Vreman (1995) as Generalised Germano Identity (GGI), which is briefly summarized as follows.

A subgrid term τ_{f} on the grid filter level (F-level) can be generally expressed as

$$\tau_{\mathrm{f}} = \overline{f(\mathbf{w})} - f\left(\overline{\mathbf{w}}\right) \tag{II.67}$$

where f is an arbitrary nonlinear function and $\mathbf{w}$ is a vector function of space and time. A test filter ($\hat{\Delta} \geq \overline{\Delta}$) is then introduced and denoted as a G-level filter. The consecutive application of these two filters corresponds to a filter on the FG-level. The subgrid term on the FG-level reads

$$T_{\mathrm{f}} = \widehat{\overline{f(\mathbf{w})}} - f\left(\widehat{\overline{\mathbf{w}}}\right) \tag{II.68}$$

Then the following identity can be derived,

$$L_{\mathrm{f}} = T_{\mathrm{f}} - \widehat{\tau_{\mathrm{f}}} = \widehat{f\left(\overline{\mathbf{w}}\right)} - f\left(\widehat{\overline{\mathbf{w}}}\right) = C_{\mathrm{dyn}}M_{\mathrm{f}} \tag{II.69}$$

where L_{f} and M_{f} can be explicitly calculated. The dynamic coefficient C_{dyn} is finally determined by the least squares approach (Lilly 1992),

$$C_{\mathrm{dyn}} = \frac{\left\langle L_{\mathrm{p}}M_{\mathrm{p}}\right\rangle}{\left\langle M_{\mathrm{q}}M_{\mathrm{q}}\right\rangle} \tag{II.70}$$

The averaging procedure is applied in homogeneous directions to avoid numerical instabilities (Germano *et al.* 1991).

All the model coefficients can be dynamically determined through GGI. For C_{d},

$$f\left(\rho_{\mathrm{g}},u_{\mathrm{g}}\right)=\rho_{\mathrm{g}}u_{\mathrm{g},i}u_{\mathrm{g},j} \tag{II.71}$$

$$L_{\mathrm{f}}=L_{ij}=\widehat{\overline{\rho_{\mathrm{g}}}\widetilde{u}_{\mathrm{g},i}\widetilde{u}_{\mathrm{g},j}}-\frac{\widehat{\overline{\rho_{\mathrm{g}}}\widetilde{u}_{\mathrm{g},i}}\,\widehat{\overline{\rho_{\mathrm{g}}}\widetilde{u}_{\mathrm{g},j}}}{\widehat{\overline{\rho_{\mathrm{g}}}}} \tag{II.72}$$

$$\begin{aligned}M_{\mathrm{f}}=M_{ij}=&-2\hat{\bar{\Delta}}^{2}\widehat{\overline{\rho_{\mathrm{g}}}}\left|S\left(\widehat{\tilde{\mathbf{u}}}_{\mathrm{g}}\right)\right|\left\{S_{ij}\left(\widehat{\tilde{\mathbf{u}}}_{\mathrm{g}}\right)-\frac{\delta_{ij}}{3}S_{kk}\left(\widehat{\tilde{\mathbf{u}}}_{\mathrm{g}}\right)\right\}\\&+2\bar{\Delta}^{2}\widehat{\overline{\rho_{\mathrm{g}}}\left|S\left(\tilde{\mathbf{u}}_{\mathrm{g}}\right)\right|\left\{S_{ij}\left(\tilde{\mathbf{u}}_{\mathrm{g}}\right)-\frac{\delta_{ij}}{3}S_{kk}\left(\tilde{\mathbf{u}}_{\mathrm{g}}\right)\right\}}\end{aligned} \tag{II.73}$$

where $\widehat{\tilde{f}}$ is defined as

$$\widehat{\tilde{f}}=\frac{\widehat{\overline{\rho_{\mathrm{g}}f}}}{\widehat{\overline{\rho_{\mathrm{g}}}}}=\frac{\widehat{\overline{\rho_{\mathrm{g}}}\tilde{f}}}{\widehat{\overline{\rho_{\mathrm{g}}}}} \tag{II.74}$$

so

$$C_{\mathrm{d}}=\frac{\left\langle\left(L_{ij}-\frac{\delta_{ij}}{3}L_{kk}\right)M_{ij}\right\rangle}{\left\langle M_{kl}M_{kl}\right\rangle}=\frac{\left\langle L_{ij}M_{ij}\right\rangle}{\left\langle M_{kl}M_{kl}\right\rangle} \tag{II.75}$$

since

$$\delta_{ij}M_{ij}=M_{nn}=0 \tag{II.76}$$

For C_{I},

$$f\left(\rho_{\mathrm{g}},\mathbf{u}_{\mathrm{g}}\right)=\rho_{\mathrm{g}}u_{\mathrm{g},k}u_{\mathrm{g},k} \tag{II.77}$$

$$L_{\mathrm{f}}=L_{kk}=\widehat{\overline{\rho_{\mathrm{g}}}\widetilde{u}_{\mathrm{g},k}\widetilde{u}_{\mathrm{g},k}}-\frac{\widehat{\overline{\rho_{\mathrm{g}}}\widetilde{u}_{\mathrm{g},k}}\,\widehat{\overline{\rho_{\mathrm{g}}}\widetilde{u}_{\mathrm{g},k}}}{\widehat{\overline{\rho_{\mathrm{g}}}}} \tag{II.78}$$

$$M_{\mathrm{f}}=M_{\mathrm{I}}=2\hat{\bar{\Delta}}^{2}\widehat{\overline{\rho_{\mathrm{g}}}}\left|S\left(\widehat{\tilde{\mathbf{u}}}_{\mathrm{g}}\right)\right|^{2}-2\widehat{\bar{\Delta}^{2}\overline{\rho_{\mathrm{g}}}\left|S\left(\tilde{\mathbf{u}}_{\mathrm{g}}\right)\right|^{2}} \tag{II.79}$$

The realizability conditions proposed by Vreman (1995) imply

$$C_{\mathrm{I}}\geq\frac{\sqrt{3}}{2}C_{\mathrm{d}} \tag{II.80}$$

so

$$C_{\mathrm{I}} = \max\left(\frac{\sqrt{3}}{2} C_{\mathrm{d}}, \frac{\langle L_{kk} M_{\mathrm{I}} \rangle}{\langle M_{\mathrm{I}} M_{\mathrm{I}} \rangle} \right) \tag{II.81}$$

For C_{T},

$$f\left(\rho_{\mathrm{g}}, \mathbf{u}_{\mathrm{g}}, T_{\mathrm{g}}\right) = \rho_{\mathrm{g}} u_{\mathrm{g},j} T_{\mathrm{g}} \tag{II.82}$$

$$L_{\mathrm{f}} = L_j = \widehat{\widetilde{\rho_{\mathrm{g}} u_{\mathrm{g},j}} \widetilde{T_{\mathrm{g}}}} - \frac{\widehat{\widetilde{\rho_{\mathrm{g}} u_{\mathrm{g},j}}} \widehat{\widetilde{\rho_{\mathrm{g}} T_{\mathrm{g}}}}}{\widehat{\rho_{\mathrm{g}}}} \tag{II.83}$$

$$M_{\mathrm{f}} = M_j = -\hat{\bar{\Delta}}^2 \widehat{\rho_{\mathrm{g}}} \left| S\left(\widehat{\mathbf{u}_{\mathrm{g}}}\right) \right| \frac{\partial \widehat{\widetilde{T_{\mathrm{g}}}}}{\partial x_j} + \widehat{\bar{\Delta}^2 \overline{\rho_{\mathrm{g}}} \left| S\left(\widetilde{\mathbf{u}_{\mathrm{g}}}\right) \right| \frac{\partial \widetilde{T_{\mathrm{g}}}}{\partial x_j}} \tag{II.84}$$

$$C_{\mathrm{T}} = \frac{C_{\mathrm{d}}}{Pr_{\mathrm{t}}} = \frac{\langle L_i M_i \rangle}{\langle M_j M_j \rangle} \tag{II.85}$$

Finally, for C_{Y_k},

$$f\left(\rho_{\mathrm{g}}, \mathbf{u}_{\mathrm{g}}, Y_k\right) = \rho_{\mathrm{g}} u_{\mathrm{g},j} Y_k \tag{II.86}$$

$$L_{\mathrm{f}} = L_{j,k} = \widehat{\widetilde{\rho_{\mathrm{g}} u_{\mathrm{g},j}} \widetilde{Y_k}} - \frac{\widehat{\widetilde{\rho_{\mathrm{g}} u_{\mathrm{g},j}}} \widehat{\widetilde{\rho_{\mathrm{g}} Y_k}}}{\widehat{\rho_{\mathrm{g}}}} \tag{II.87}$$

$$M_{\mathrm{f}} = M_{j,k} = -\hat{\bar{\Delta}}^2 \widehat{\rho_{\mathrm{g}}} \left| S\left(\widehat{\mathbf{u}_{\mathrm{g}}}\right) \right| \frac{\partial \widehat{\widetilde{Y_k}}}{\partial x_j} + \widehat{\bar{\Delta}^2 \overline{\rho_{\mathrm{g}}} \left| S\left(\widetilde{\mathbf{u}_{\mathrm{g}}}\right) \right| \frac{\partial \widetilde{Y_k}}{\partial x_j}} \tag{II.88}$$

$$C_{Y_k} = \frac{C_{\mathrm{d}}}{Sc_{\mathrm{t},k}} = \frac{\langle L_{i,k} M_{i,k} \rangle}{\langle M_{j,k} M_{j,k} \rangle} \tag{II.89}$$

II.B Chapter Summary

A formulation system for DNS/LES of gas-liquid two-phase reactive flows has been designed. The gas flow field is described by the full 3D time-dependant compressible Navier-Stokes equations, while the dispersed phase is tracked in the Lagrangian frame. Arrhenius-

type finite-rate chemistry is employed for the chemical reaction. The interactions among turbulence, combustion, buoyancy and evaporating droplets are taken into account through various source/sink terms built in the gas phase governing equation. In the context of LES, in order to capture the highly local interactions, fully dynamic Smagorinsky, Yoshizawa, eddy-diffusivity models, in which the model coefficients vary with time and space, have been developed for subgrid stress tensor, subgrid kinetic energy, subgrid heat and species flux, respectively. The filtered reaction rate is modelled by a scale similarity model. Finally, the SGS effects on the droplet motion and evaporation are neglected in the present study.

Chapter III – Numerical Techniques

III.A Spatial Discretizations

III.A.1 Spatial Derivatives (Sandham & Reynolds 1989)

High-order compact schemes with spectral-like resolution (Lele 1992) are adopted for the discretization of spatial derivatives. To facilitate the computation, the tri-diagonal scheme family has been employed, which can be solved by the direct Thomas solver. For the first order derivative, the scheme for internal points can be written in the following form,

$$f'_{i-1} + af'_i + f'_{i+1} = b\frac{f_{i+1} - f_{i-1}}{2h} + c\frac{f_{i+2} - f_{i-2}}{4h} \qquad (i \neq 1,2,n-1,n) \qquad \text{(III.1)}$$

where the coefficients are

$$a = 3, b = \frac{2+4a}{3}, c = \frac{4-a}{3} \qquad \text{(III.2)}$$

corresponding to a sixth-order scheme. For the boundary and next to boundary points along non-periodic directions,

$$af'_1 + f'_2 = \frac{-5f_1 + 4f_2 + f_3}{h} \qquad \text{(III.3)}$$

$$f'_1 + af'_2 + f'_3 = \frac{3f_1 - 3f_3}{h} \qquad \text{(III.4)}$$

are third- and fourth-order schemes, respectively, while along periodic directions, Eq. (III.1) can be used for all the grid points. In the framework of finite difference methods, two consecutive applications of a first derivative gives a much worse representation of the high wave numbers than a single second derivative computation (Sandham & Reynolds 1989). A Padé scheme with the same 3-4-6-4-3 frame is therefore used for the second order derivative,

$$f''_{i-1} + af''_i + f''_{i+1} = b\frac{f_{i+1} - 2f_i + f_{i-1}}{h^2} + c\frac{f_{i+2} - 2f_i + f_{i-2}}{4h^2} \qquad \text{(III.5)}$$

$$af''_1 + f''_2 = \frac{13f_1 - 27f_2 + 15f_3 - f_4}{h^2} \qquad (i = 1, n) \qquad \text{(III.6)}$$

$$f''_1 + af''_2 + f''_3 = \frac{f_1 - 2f_2 + 12f_3}{h^2} \qquad (i = 2, n\text{-}1) \qquad \text{(III.7)}$$

where the coefficients are

$$a = 5.5, b = \frac{4a - 4}{3}, c = \frac{10 - a}{3} \qquad \text{(III.8)}$$

The cross derivative terms are evaluated using two successive applications of the first derivative formula.

With ideally low dissipation and dispersion errors, these spatial schemes have been applied successfully in DNS studies on various scenarios, *e.g.*, compressible temporal mixing layer with various Mach numbers (Sandham & Reynolds 1989), supersonic partially premixed diffusion flames (Luo 1999), buoyancy-driven reactive plumes (Jiang & Luo 2000a), *etc.*

III.A.2 Numerical Filtering

The finite difference schemes generate their largest errors at the highest wave numbers supported by the computational grid, $1/(2h)$. A fourth-order compact filter (Lele 1992) is therefore introduced in the present study to eliminate these high wave number errors, which can be written as

$$\alpha\hat{f}_{i-1} + \hat{f}_i + \alpha\hat{f}_{i+1} = af_i + \frac{b}{2}\left(f_{i+1} + f_{i-1}\right) + \frac{c}{2}\left(f_{i+2} + f_{i-2}\right) \qquad \text{(III.9)}$$

where the coefficients are

$$a = \frac{1}{8}(5 + 6\alpha), b = \frac{1}{2}(1 + 2\alpha), c = -\frac{1}{8}(1 - 2\alpha) \qquad \text{(III.10)}$$

In Eq. (III.9), by reducing α towards 0.5 the filtering effect is confined more and more towards the shorter waves, and α=0.5 corresponds to no filtering effect at all. In this study, α is set to 0.4983 as in Le Ribault *et al.* (1999).

The fourth-order Padé-type boundary filter derived by Gaitonde & Visbal (2000) is employed to close the whole filter scheme. For the next to boundary point i=2, the filtering scheme can be written as

$$\alpha \hat{f}_1 + \hat{f}_2 + \alpha \hat{f}_2 = \sum_{k=1}^{5} a_k f_k \qquad \text{(III.11)}$$

where the coefficients are

$$a_1 = \frac{1+14\alpha}{16}, a_2 = \frac{3+2\alpha}{4}, a_3 = \frac{3+2\alpha}{8}, a_4 = \frac{-1+2\alpha}{4}, a_5 = \frac{1-2\alpha}{16} \qquad \text{(III.12)}$$

The numerical filtering operation is not imposed at the boundary point i=1, since it is the responsibility of boundary conditions to set flow variables at boundaries (Gaitonde & Visbal 2000).

As a necessary component, various types of numerical filters are now being used in different applications to damp the high wave number spurious oscillations in DNS/LES (Le Ribault *et al.* 1999; Leboissetier *et al.* 2004; Schmitt 2005). However, it is crucial to keep the influence of the dissipative effect of the numerical filter as weak as possible in LES, where the SGS models are expected to play the dominant role to dissipate the kinetic energy when grid spacing is increased. To this end, the whole LES flow field is filtered once every four time steps. It was found that the filtering effect is very similar if the filtering frequency is once per four or eight time steps, but further increasing the filtering frequency results in smoothing the flow field. The filtering frequency is much less in DNS, *i.e.*, once every 32 time steps, since the grid resolution is improved and thus more high frequency wave components are accurately solved by a same compact finite-difference scheme.

III.A.3 The Interpolation Scheme

The knowledge of gas phase flow variables at the local droplet position is required by the Lagrangian droplet transport equations. Since the droplet locations will not coincide with the grid points in general, an interpolation scheme is therefore needed. In the present study, a fourth-order Lagrangian interpolation scheme (Balachandar & Maxey 1989) is employed, which is summarized as follows for completeness.

A one-dimensional fourth-order Lagrangian interpolation scheme can be expressed as

$$f(x)=\sum_{i=0}^{3} f(x_i)L_i(x) \tag{III.13}$$

The basic functions $L_i(x)$ depends on the location of x:

(1) If $x_0<x_1\le x<x_2<x_3$, set $\xi=(x-x_1)/h$ $(0\le\xi<1)$, where $h=x_{i+1}-x_i$, i=0,1,2, then

$$L_0(x)=\frac{1}{6}\left(-\xi^3+3\xi^2-2\xi\right),\ L_1(x)=\frac{1}{2}\left(\xi^3-2\xi^2-\xi+2\right)$$

$$L_2(x)=\frac{1}{2}\left(-\xi^3+\xi^2+2\xi\right),\ L_3(x)=\frac{1}{6}\left(\xi^3-\xi\right) \tag{III.14}$$

(2) If $x_0\le x<x_1<x_2<x_3$, set $\xi=(x-x_0)/h$ $(0\le\xi<1)$, then

$$L_0(x)=\frac{1}{6}\left(-\xi^3+6\xi^2-11\xi+6\right),\ L_1(x)=\frac{1}{2}\left(\xi^3-5\xi^2+6\xi\right)$$

$$L_2(x)=\frac{1}{2}\left(-\xi^3+4\xi^2-3\xi\right),\ L_3(x)=\frac{1}{6}\left(\xi^3-3\xi^2+2\xi\right) \tag{III.15}$$

(3) If $x_0<x_1<x_2\le x<x_3$, set $\xi=(x-x_2)/h$ $(0\le\xi<1)$, then

$$L_0(x)=\frac{1}{6}\left(-\xi^3+\xi\right),\ L_1(x)=\frac{1}{2}\left(\xi^3+\xi^2-2\xi\right)$$

$$L_2(x)=\frac{1}{2}\left(-\xi^3-2\xi^2+\xi+2\right),\ L_3(x)=\frac{1}{6}\left(\xi^3+3\xi^2+2\xi\right) \tag{III.16}$$

Equation (III.13) can be extended to the 3D case as

$$f(x,y,z)=\sum_{i=0}^{3}\sum_{j=0}^{3}\sum_{k=0}^{3} f(x_i,y_j,z_k)L_i(x)L_j(y)L_k(z) \tag{III.17}$$

Equations (III.14)-(III.16) are designed for a uniform grid system. The interpolation formula for non-uniform grids can be derived in a similar way.

It is worth noting that pursuing high-order interpolation accuracy results in considerable CPU time due to the intensive floating-point calculations involved in the interpolation scheme. As shown by Miller & Bellan (2000), the Lagrangian interpolation was a major consumer (40%) of the simulation time of droplet calculations.

III.B Time Advancement

III.B.1 The Gas Phase (Sandham & Reynolds 1989)

The time advancement of the gas phase flow variables is accomplished by a fully explicit third-order three-stage low-storage Runge-Kutta scheme derived by Wray (1986), which can be expressed as

$$Q_{1,i}^{\text{new}} = a_{1,i}\Delta t Q_{1,i}^{\text{old}} + Q_{2,i}^{\text{old}}, Q_{2,i}^{\text{new}} = a_{2,i}\Delta t Q_{1,i}^{\text{old}} + Q_{2,i}^{\text{old}} \qquad (i=1,2,3) \qquad \text{(III.18)}$$

where Q_1 and Q_2 are identical and represent the conservative flow variables at the beginning of every time step. Q_1 is then used to calculate and store the RHS. Finally Eq. (III.18) is used to update Q_1 and Q_2. The constants a_1 and a_2 are

$$(a_1,a_2)_{,1} = \left(\frac{2}{3},\frac{1}{4}\right), (a_1,a_2)_{,2} = \left(\frac{5}{12},\frac{3}{20}\right), (a_1,a_2)_{,3} = \left(\frac{3}{5},\frac{3}{5}\right) \qquad \text{(III.19)}$$

III.B.2 The Droplet Phase

The droplet transport equations (II.42)-(II.44) are advanced by the semi-analytical approach (Ling *et al.* 2001; Göz *et al.* 2004), taking into the consideration of stability, efficiency and accuracy. It is directly from the solution of the Ordinary Differential Equation (ODE)

$$\frac{dy}{dt} = k_1 y + k_2 \qquad \text{(III.20)}$$

where k_1 and k_2 are assumed to be two constants in Eqs. (II.42)-(II.44) during the integration over a small time step. Consequently, the crucial parameter for the semi-analytical approach is the ratio of the time step to the droplet responsive time, which should be always small during the course of simulations.

III.B.3 The Time Step

The time step limitation for stability is estimated on a model convection-diffusion equation (Sandham & Reynolds 1989),

$$\Delta t = \frac{CFL}{D_c + D_\mu} \tag{III.21}$$

where

$$D_c = \pi c \left(\frac{1}{\Delta x} + \frac{1}{\Delta y} + \frac{1}{\Delta z} \right) + \pi \frac{|u_i|}{\Delta x_i} \tag{III.22}$$

$$D_\mu = \frac{\pi^2 \mu / \rho}{(\gamma - 1) Ma^2 RePr} \left(\frac{1}{\Delta x^2} + \frac{1}{\Delta y^2} + \frac{1}{\Delta z^2} \right) \tag{III.23}$$

For linear equations the CFL number for the third-order Runge-Kutta method, Eqs. (III.18) and (III.19), could be chosen up to $\sqrt{3}$. In the present study, a small CFL number, 1.5, is used for all the simulations.

The time step Δt from Eq. (III.21) is used for the droplet transport as well. The kinematical, thermal and evaporating responsive time scales of the droplets are all closely related to the Stokes number *St*, and thus the ratio of the time step Δt to the characteristic droplet time scale, $\Delta t/St$ in the non-dimensional context, for every droplet is monitored throughout the whole simulation period and found to be smaller than 1 for all the cases. In addition, each droplet is monitored not to cross over one grid spacing in all the three directions within one time step.

III.C Boundary Conditions for the Reacting Jets and Plumes

The boundary conditions (BCs) employed for the temporal multiphase reacting shear layers in Chapter IV are periodic in the streamwise and spanwise directions, while in the cross-stream direction the adiabatic slip wall (Poinsot & Lele 1992) is used.

For spatially-developing flows such as the reacting jets in Chapter V and reacting plumes in Chapter VI, to set BCs for open domain simulations is a difficult topic. Nowadays, the Non-Reflecting BCs (NRBC) proposed by Thompson (1987, 1990) and improved by Poinsot & Lele (1992) have been well recognized as a standard approach to tackle this problem, which is based on characteristic wave analysis. Simply speaking, at free-stream boundaries, the amplitudes of those incoming characteristic waves are set to zero or derived from known information, while the amplitudes of outgoing characteristic waves are calculated based on the flow variables at internal grid points. The detailed derivation for NRBC has been given by Sandham & Reynolds (1989). The same process is repeated here to take into account the influence of evaporation in multiphase reactive flows. To simplify the writing work, the subscript "g" for the gas phase is neglected in this section. The BCs presented in the following subsections have been used for both DNS and LES, *i.e.*, the subgrid terms in LES are assumed to have small influence on the BCs.

The gas phase governing equations can be cast into the following vector form,

$$\frac{\partial \mathbf{Q}}{\partial t}+\frac{\partial \mathbf{F}}{\partial x}=\mathbf{RHS} \tag{III.24}$$

where $\mathbf{Q}$ is the conservative flow variables,

$$\mathbf{Q}=\left(\rho,\rho u,\rho v,\rho w,\rho E_{\mathrm{T}},\rho Y_{\mathrm{f}},\rho Y_{\mathrm{o}},\rho Y_{\mathrm{v}}\right)^{\mathrm{T}} \tag{III.25}$$

where the total energy E_{T} for evaporating two-phase flows can be written as

$$E_{\mathrm{T}}=\frac{p}{\gamma-1}+\rho Y_{\mathrm{v}}h_{\mathrm{v}}^{0}+\rho\frac{u_i u_i}{2} \tag{III.26}$$

Suppose x is the normal direction at the boundary. All the irrelevant terms, including derivatives in y and z directions, source/sink terms due to chemical reaction and the dispersed phase, viscous terms, *etc.*, are put in **RHS**. Since the characteristic analysis is more convenient with non-conservative independent variables **U**,

$$\mathbf{U} = \left(\rho, u, v, w, d, Y_{\mathrm{f}}, Y_{\mathrm{o}}, Y_{\mathrm{v}}\right)^{\mathrm{T}} \tag{III.27}$$

where d is defined by

$$d = p\rho^{-\gamma} \tag{III.28}$$

Eq. (III.24) is transformed into the following form,

$$\frac{\partial \mathbf{U}}{\partial t} + \mathbf{A}\frac{\partial \mathbf{U}}{\partial x} = \mathbf{R}^{-1}(\mathbf{RHS}) \tag{III.29}$$

where

$$\mathbf{R} = \frac{\partial \mathbf{Q}}{\partial \mathbf{U}} = \begin{bmatrix} 1 & 0 & 0 & 0 & 0 & 0 & 0 & 0 \\ u & \rho & 0 & 0 & 0 & 0 & 0 & 0 \\ v & 0 & \rho & 0 & 0 & 0 & 0 & 0 \\ w & 0 & 0 & \rho & 0 & 0 & 0 & 0 \\ a & \rho u & \rho v & \rho w & \dfrac{\rho^{\gamma}}{\gamma - 1} & 0 & 0 & \rho h_{\mathrm{v}}^{0} \\ Y_{\mathrm{f}} & 0 & 0 & 0 & 0 & \rho & 0 & 0 \\ Y_{\mathrm{o}} & 0 & 0 & 0 & 0 & 0 & \rho & 0 \\ Y_{\mathrm{v}} & 0 & 0 & 0 & 0 & 0 & 0 & \rho \end{bmatrix} \tag{III.30}$$

$$\mathbf{R}^{-1}=\begin{bmatrix} 1 & 0 & 0 & 0 & 0 & 0 & 0 & 0 \\ -\frac{u}{\rho} & \frac{1}{\rho} & 0 & 0 & 0 & 0 & 0 & 0 \\ -\frac{v}{\rho} & 0 & \frac{1}{\rho} & 0 & 0 & 0 & 0 & 0 \\ -\frac{w}{\rho} & 0 & 0 & \frac{1}{\rho} & 0 & 0 & 0 & 0 \\ b & -\frac{u(\gamma-1)}{\rho^{\gamma}} & -\frac{v(\gamma-1)}{\rho^{\gamma}} & -\frac{w(\gamma-1)}{\rho^{\gamma}} & \frac{\gamma-1}{\rho} & 0 & 0 & -\frac{h_{\mathrm{v}}^{0}(\gamma-1)}{\rho^{\gamma}} \\ -\frac{Y_{\mathrm{f}}}{\rho} & 0 & 0 & 0 & 0 & \frac{1}{\rho} & 0 & 0 \\ -\frac{Y_{\mathrm{o}}}{\rho} & 0 & 0 & 0 & 0 & 0 & \frac{1}{\rho} & 0 \\ -\frac{Y_{\mathrm{v}}}{\rho} & 0 & 0 & 0 & 0 & 0 & 0 & \frac{1}{\rho} \end{bmatrix} \tag{III.31}$$

$$\frac{\partial \mathbf{F}}{\partial \mathbf{U}}=\begin{bmatrix} u & \rho & 0 & 0 & 0 & 0 & 0 & 0 \\ u^{2}+\gamma d\rho^{\gamma-1} & 2\rho u & 0 & 0 & \rho^{\gamma} & 0 & 0 & 0 \\ uv & \rho v & \rho u & 0 & 0 & 0 & 0 & 0 \\ uw & \rho w & 0 & \rho u & 0 & 0 & 0 & 0 \\ e & f & \rho uv & \rho uw & \frac{\gamma p^{\gamma} u}{\gamma-1} & 0 & 0 & \rho u h_{\mathrm{v}}^{0} \\ uY_{\mathrm{f}} & \rho Y_{\mathrm{f}} & 0 & 0 & 0 & \rho u & 0 & 0 \\ uY_{\mathrm{o}} & \rho Y_{\mathrm{o}} & 0 & 0 & 0 & 0 & \rho v & 0 \\ uY_{\mathrm{v}} & \rho Y_{\mathrm{v}} & 0 & 0 & 0 & 0 & 0 & \rho w \end{bmatrix} \tag{III.32}$$

$$\mathbf{A}=\mathbf{R}^{-1}\frac{\partial \mathbf{F}}{\partial \mathbf{U}}=\begin{bmatrix} u & \rho & 0 & 0 & 0 & 0 & 0 & 0 \\ \frac{c^{2}}{\rho} & u & 0 & 0 & \rho^{\gamma-1} & 0 & 0 & 0 \\ 0 & 0 & u & 0 & 0 & 0 & 0 & 0 \\ 0 & 0 & 0 & u & 0 & 0 & 0 & 0 \\ 0 & 0 & 0 & 0 & u & 0 & 0 & 0 \\ 0 & 0 & 0 & 0 & 0 & u & 0 & 0 \\ 0 & 0 & 0 & 0 & 0 & 0 & u & 0 \\ 0 & 0 & 0 & 0 & 0 & 0 & 0 & u \end{bmatrix} \tag{III.33}$$

$$a=\frac{\partial E_{\mathrm{T}}}{\partial \rho}=\frac{c^{2}}{\gamma-1}+h_{\mathrm{v}}^{0}Y_{\mathrm{v}}+\frac{u_{i}u_{i}}{2} \tag{III.34}$$

$$b=\frac{\gamma-1}{\rho^{\gamma}}\left(-\frac{\gamma d\rho^{\gamma-1}}{\gamma-1}+\frac{u_i u_i}{2}\right) \tag{III.35}$$

$$e=\frac{\partial\left\{\left(E_{\mathrm{T}}+p\right)u\right\}}{\partial\rho}=\frac{\gamma^2 d\rho^{\gamma-1}u}{\gamma-1}+h_{\mathrm{v}}^0 Y_{\mathrm{v}}u+\frac{u^3+uv^2+uw^2}{2} \tag{III.36}$$

$$f=\frac{\partial\left\{\left(E_{\mathrm{T}}+p\right)u\right\}}{\partial u}=\frac{\gamma d\rho^{\gamma}}{\gamma-1}+h_{\mathrm{v}}^0\rho Y_{\mathrm{v}}+\frac{\rho}{2}\left(3u^2+v^2+w^2\right) \tag{III.37}$$

And,

$$\frac{\partial\mathbf{F}}{\partial x}=\mathbf{R}\mathbf{A}\frac{\partial\mathbf{U}}{\partial x}=\mathbf{R}\left(\mathbf{T}^{-1}\mathbf{\Lambda}\mathbf{T}\right)\mathbf{S}\frac{\partial\mathbf{V}}{\partial x}=\mathbf{R}\mathbf{T}^{-1}\left(\mathbf{\Lambda}\mathbf{T}\mathbf{S}\frac{\partial\mathbf{V}}{\partial x}\right)=\mathbf{R}\mathbf{T}^{-1}\vec{\ell} \tag{III.38}$$

where matrix $\mathbf{A}$ is diagonalized by $\mathbf{T}^{-1}$ and $\mathbf{T}$,

$$\mathbf{T}^{-1}=\begin{bmatrix} \frac{1}{2c^2} & -\frac{1}{c^2} & 0 & 0 & \frac{1}{2c^2} & 0 & 0 & 0 \\ -\frac{1}{2\rho c} & 0 & 0 & 0 & 0 & \frac{1}{2\rho c} & 0 & 0 \\ 0 & 0 & 1 & 0 & 0 & 0 & 0 & 0 \\ 0 & 0 & 0 & 1 & 0 & 0 & 0 & 0 \\ 0 & \rho^{-\gamma} & 0 & 0 & 0 & 0 & 0 & 0 \\ 0 & 0 & 0 & 0 & 0 & 1 & 0 & 0 \\ 0 & 0 & 0 & 0 & 0 & 0 & 1 & 0 \\ 0 & 0 & 0 & 0 & 0 & 0 & 0 & 1 \end{bmatrix} \tag{III.39}$$

The diagonal elements of matrix $\mathbf{\Lambda}$ are (u-c, u, u, u, u+c, u, u, u), *i.e.*, the characteristic velocities $\boldsymbol{\lambda}$, the sign of which determines the propagating direction of different characteristic waves. The transformation of $\mathbf{U}$ to $\mathbf{V}$

$$\mathbf{V}=\left(\rho,u,v,w,p,Y_{\mathrm{f}},Y_{\mathrm{o}},Y_{\mathrm{v}}\right)^{\mathrm{T}} \tag{III.40}$$

is purely due to easier mathematical expressions with pressure p. $\mathbf{S}$ is the transformation matrix. The amplitude variations of the characteristic waves crossing the boundary $\vec{\ell}$ are defined by

$$\vec{\ell} = \begin{bmatrix} \ell_1 \\ \ell_2 \\ \ell_3 \\ \ell_4 \\ \ell_5 \\ \ell_6 \\ \ell_7 \\ \ell_8 \end{bmatrix} = \begin{bmatrix} (u-c)\left(\dfrac{\partial p}{\partial x} - \rho c \dfrac{\partial u}{\partial x}\right) \\ u\left(\dfrac{\partial p}{\partial x} - c^2 \dfrac{\partial \rho}{\partial x}\right) \\ u\dfrac{\partial v}{\partial x} \\ u\dfrac{\partial w}{\partial x} \\ (u+c)\left(\dfrac{\partial p}{\partial x} + \rho c \dfrac{\partial u}{\partial x}\right) \\ u\dfrac{\partial Y_{\mathrm{f}}}{\partial x} \\ u\dfrac{\partial Y_{\mathrm{o}}}{\partial x} \\ u\dfrac{\partial Y_{\mathrm{v}}}{\partial x} \end{bmatrix} \tag{III.41}$$

From Eq. (III.38), it can be seen that the normal derivative terms $\partial \mathbf{F}/\partial x$ at the boundary depend on $\vec{\ell}$, which is in turn determined by the propagating direction of the characteristic waves, *i.e.*, ℓ_i is calculated by (III.41) for outward waves, while for inward waves, ℓ_i is determined by Local One-Dimensional Inviscid (LODI) relations proposed by Poinsot & Lele (1992), usually denoted as NSCBC (Navier-Stokes Characteristic Boundary Conditions) approach, or set to zero if no flow information outside the computational domain can be speculated according to the definition of NRBC (Thompson 1987, 1990).

III.C.1 The Inflow Boundary

At the inflow boundary, only ℓ_1 is outward and can be computed from interior grid points, so seven physical BCs for ℓ_2 - ℓ_8 are needed to produce a definite numerical solution, which are given by the inflow velocity, species mass fraction and temperature profiles. The vertical velocity w_0, $Y_{\mathrm{f},0}$ and $Y_{\mathrm{o},0}$ at the inflow boundary are described by hyperbolic tangent profiles,

$$f_0 = \frac{f_1 + f_2}{2} - \frac{f_1 - f_2}{2} \tanh\left(\frac{\left| y - 0.5L_y \right| - 0.5h}{2\theta} \right) \tag{III.42}$$

where the subscripts "1" and "2" represent the jet core and free stream, respectively. The temperature is correlated with w through Crocco-Buseman relation (White 1991),

$$T_{g,0} = 0.5(\gamma - 1) Ma^2 \left\{ w(w_1 + w_2) - w^2 - w_1 w_2 \right\} + \frac{w(T_1 - T_2) + w_1 T_2 - w_2 T_1}{w_1 - w_2} \tag{III.43}$$

u_0, v_0 and $Y_{v,0}$ are set to zero. Random periodic sinusoidal disturbances are superimposed onto u_0 to introduce 3D effects.

Since temperature is an important parameter in combustion simulations, it is preferable to manually set the temperature profiles at the inflow boundary and leave the density as a "soft" variable, which is determined by LODI relations as shown by Poinsot & Lele (1992).

Droplets enter the computational domain with the fuel jet through the slot nozzle. The initial droplet velocities $\mathbf{v}_{d,0}$ are identical to the local gas phase velocities, and the initial temperature $T_{d,0}$ equals the ambient temperature. The spacing between droplets in all the three directions is set to be equal to obtain a homogeneous initial distribution.

III.C.2 The Lateral Boundaries

At the lateral boundaries, all the flow variables, except the normal velocity, which is crucial for entrainment, are set to be identical with the constant ambient data. According to LODI relations, $\ell_2 = \ell_3 = \ell_4 = \ell_6 = \ell_7 = \ell_8 = 0$. For subsonic flows, the propagation directions of ℓ_1 and ℓ_5 are definite. Whether they are inward or outward waves depends on the location of the boundary, as shown in Fig. III-1. Once one of them is determined as an outward wave, the other can be calculated from the LODI relation for constant pressure, $\ell_1 + \ell_5 = 0$ (Poinsot & Lele 1992). By this means, the normal velocity is treated as a "soft" variable at the lateral boundaries, which is ideal to account for the entrainment effect. This

lateral BC is proposed by Jiang & Luo (2000a) and works well for DNS of buoyant and reactive plumes.

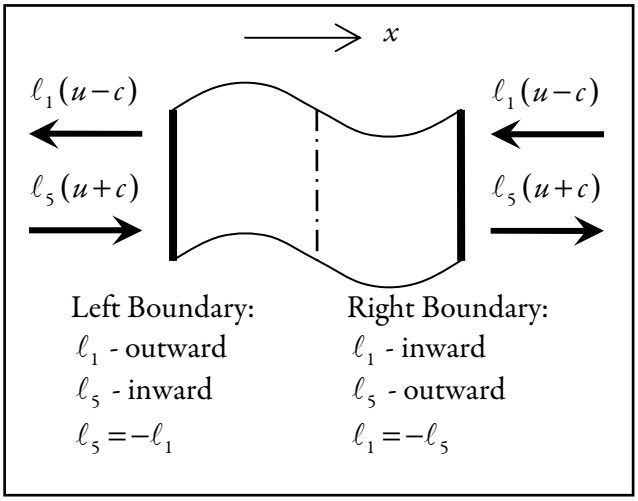

Figure III-1: Illustration of lateral boundary conditions.

III.C.3 The Spanwise (Periodic) Boundaries

The spanwise boundaries are periodic for 3D planar jet simulations. In this sense, no BCs are needed at the spanwise boundaries for the gas phase. As for the dispersed phase, when a droplet leaves one end of the periodic boundary, a new one with identical properties as the leaving one is put at the corresponding position at the other end.

III.C.4 The Outflow Boundary

The outflow BC for DNS/LES is difficult to design since the flow information outside the computational domain is completely unknown or cannot be deduced. Thompson's NRBC is employed in the present study, *i.e.*, for all the inward waves, ℓ_i's are set to zero to follow the "non-reflecting" spirit for DNS/LES in an infinite free domain. However, as stated by Colonius (2004), such linearized BCs are generally not competent for a spatially evolving flow as in this study due to the numerical wave reflections at the outflow boundary. A sponge layer (Sandhu & Sandham 1994) is then attached at the end of the physical do-

main to damp the wave reflections. A forcing term is added into the solution vector, $\mathbf{Q}$, of the Navier-Stokes equations in the sponge layer, and the new solution, $\mathbf{Q}_{sp}$, can be written as

$$\mathbf{Q}_{sp} = \mathbf{Q} - d_f(x)(\mathbf{Q} - \mathbf{Q}_{av}) \tag{III.44}$$

where $d_f(x)$ is the empirical damping function,

$$d_f(x) = 0.6\exp\left\{-7.0\left[(x_e - x)/(x_e - x_s)\right]^{4.0}\right\} \tag{III.45}$$

x_s and x_e represent the coordinates of the start and end of the sponge layer respectively. $\mathbf{Q}_{av}$ is the averaged value of $\mathbf{Q}$ over a small physical region just in front of the sponge layer. The sponge layer approach together with Thompson's NRBC at the end of the computational domain was found to be very effective to control the wave reflection at the outflow boundary and deployed in all the simulations.

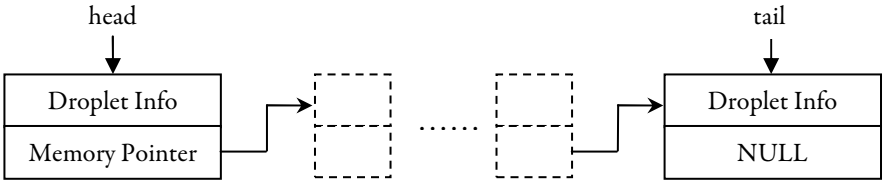

Figure III-2: Data structure of droplets.

III.D Parallel Algorithm

III.D.1 The Data Structure of Droplets

The dispersed phase consists of discrete droplets, whose number can be increased by continuously supply at the jet nozzle, decreased by evaporation and moving out of the computational domain. In this sense, it is completely different from the gas phase, which is described numerically by a "field" with fixed grid points. The data structure of "array" for a flow field is not appropriate to store the droplet data. The data structure used for discrete droplets in the present study is the "linked list" shown in Fig. III-2, which is capable of making full use of the discontinuous parts of the computer memory. Meanwhile, to update the droplet in-

formation, add a new droplet to the list or delete an old droplet from the list is all in a straightforward way.

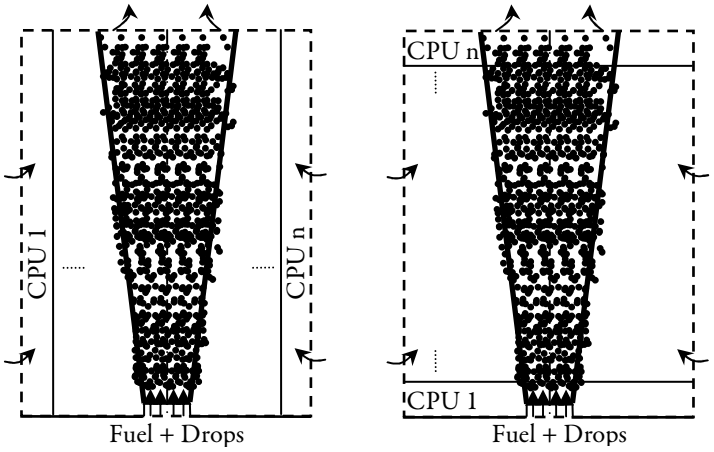

Figure III-3: Two parallel strategies for two-phase simulations: left-(a), right-(b).

III.D.2 The Parallel Algorithm

The MPI (Message Passing Interface: http://www-unix.mcs.anl.gov/mpi/) algorithm is utilized for the code parallelism. Due to the implicit compact schemes used for spatial derivatives, the domain is divided just in one direction, as shown in Fig. III-3. Either option can be chosen for the gas phase parallelism with no evident performance difference. However, with the concern of load balance among respective CPUs, Fig. III-3b is optimal for two-phase simulations. An important issue which should be taken into consideration, if the parallel strategy in Fig. III-3b is followed, is the droplets' transferring between adjacent CPUs at the end of every time step, which may lead to huge communication time among CPUs and deteriorate the parallel performance. This problem is circumvented in the code by using non-blocking MPI functions. The key idea of non-blocking communication mechanism is to overlap the computation and communication time. Therefore, the droplet transferring is started at the end of each time step, while the ending stage of the transferring is put at the next time step, just after the advancement of gas phase variables is finished and before the droplet code is executed, since the whole process of updating the flow variables

does not require any droplet information except for the droplet source terms. In such a way, the droplet transferring among CPUs is overlapped with the gas phase updating process, and the parallel performance is greatly improved in comparison with that using blocking communication mechanism.

III.E Chapter Summary

The numerical techniques for DNS/LES of multiphase reactive flows have been presented in this chapter. Sixth-order compact finite difference schemes are employed for both first and second derivative discretizations. A fourth-order compact filter is introduced to diminish the high wave number numerical errors. To optimize the effect of the numerical filter, the filtering parameter α is set to 0.4983 (α=0.5 corresponds to no filtering effect), and the flow field is filtered once every four time steps in LES and once every thirty-two time steps in DNS. In two-phase simulations, gas properties are needed at the droplet locations, which are obtained by a fourth-order Lagrangian interpolation scheme. The explicit third-order three-stage low-storage Runge-Kutta scheme is employed for the carrier phase, with the semi-analytical approach for the droplet phase. The numerical stability for all the two-phase simulations is ensured by setting a small CFL number, 1.5, and meanwhile, keeping the ratio of the time step to the characteristic droplet responsive time always small. The boundary condition schemes are based on the characteristic wave analysis and follow the "non-reflecting" criterion for infinite free domain simulations. The BCs for the inflow and lateral boundaries stem from the NSCBC approach. The spanwise direction is periodic. At the outflow boundary, a sponge layer is attached at the end of the physical domain to damp numerical wave reflections. In addition, the NRBC is deployed at the end of the computational domain. This combined method is found to be very effective to control the wave reflections through the outflow boundary. The initial conditions for various simulations will be discussed in the following chapters whenever necessary.

The data structure of linked list is proposed to record the droplet data according to its discrete characteristic. An efficient parallel algorithm based on the non-blocking communication mechanism in MPI has been designed for two-phase simulations.

Chapter IV – DNS of Droplet Effects on a Reacting Shear Layer

IV.A Introduction

The present study is motivated by several technological applications, such as the humidified gas turbines (Jonsson & Yan 2005), the hybrid Solid-Oxide Fuel Cell (SOFC) - gas turbine system (Kee *et al.* 2005), fire control and extinguishment in the field of fire suppression (Grant *et al.* 2000). All these applications involve combustion diluted by water droplets/mist. Much of the previous work has been dedicated to studying the interactions between droplets/particles and turbulence in non-reacting flow (Boivin *et al.* 1998; Mashayek 1998; Ling *et al.* 2001; Hu *et al.* 2002), and multitude interactions in spray combustion (Réveillon & Vervisch 2000; Sadiki et al. 2005; Sreedhara & Huh 2007; Wang & Rutland 2007; Réveillon & Demoulin 2007). Fundamental investigations of the interactions among mixing, reaction, droplet dynamics and evaporation in a multiphase combustion system with water dilution have been few and far between. One key feature is that evaporation of non-reactant droplets has inhibition effects on combustion through cooling, diluting and separating the fuel and the oxidizer, as compared with fuel preparation through evaporation in spray combustion. Many questions, in particular how combustion models should be modified to account for liquid water dilution, remain unanswered.

The present chapter reports a fundamental study of the complex interaction in multiphase combustion with liquid droplets dilution in a simple configuration, *i.e.*, a three-dimensional temporally-developing reacting shear layer with the oxidizer stream laden with evaporating droplets. It features fully resolved DNS for gaseous combustion coupled with a

Lagrangian approach for evaporating droplets. Grid-resolution-independent results have been obtained in cases without and with droplets. The study aims to elucidate evaporating droplet effects on micromixing, scalar transport and combustion. A comprehensive parametric study has been conducted by varying the initial Stokes number (St_0) and mass loading ratio (MLR_0). Detailed field analysis has been conducted to examine the complex nonlinear interactions among droplet dynamics, evaporation, turbulence and combustion, and so on. Effects of evaporating droplets on averaged flow and combustion quantities have also been presented. In particular, the conditional scalar dissipation rate is found to be enhanced by evaporating droplets, which suggests that they can promote micromixing and combustion under certain conditions, in addition to their roles in combustion suppression. The transport equation for the mixture fraction variance $\widetilde{Z''^2}$ has been analyzed, with a focus on the vaporization-related source terms. Such source terms exhibit more complex local variations in the present shear-flow configuration, compared with the case in the homogeneous decaying turbulence configuration of Réveillon and Vervisch (2000).

IV.B Methodology

The complete set of nondimensionalized governing equations includes the time-dependent compressible Navier-Stokes equations, the transport equations for the gas fuel, gas oxidizer, water vapour, and the evaporating droplets. The governing equations for the gaseous phase are solved in the Eulerian frame based on a well established DNS code (Luo 1999). The discrete phase is treated in the Lagrangian frame. To describe the droplets evaporation, the classical rapid mixing model (Spalding 1953) is selected for its simplicity compared with other advanced models (Miller *et al.* 1998; Sazhin 2006). The gravitational effects on droplets are not included. The two-way coupling between the continuum and the discrete phase is included in the source terms, which account for mass, momentum and heat exchange (see Chapter II or Xia *et al.* 2008).

The temporal mixing layer configuration is selected for its prototype value for combustion research and the ease with which statistics can be obtained (Luo 1999; Miller & Bellan 1999). Computational cost is another consideration, which cannot be eased by access to the

latest teraflops computers if DNS of spatially developing two-phase reacting flows is the target. The letters *x*, *y*, *z* or numbers 1, 2, 3 refer to the streamwise, cross-stream and spanwise directions throughout this chapter. The fuel is in the upper stream and the oxidiser laden with droplets in the lower stream moving in the opposite direction. The initial profiles of the gas streamwise velocity $u_{g,1}$, mass fractions of fuel Y_f and oxidizer Y_o, and droplet number density n_d are determined by an error function, $f(x_2)=f_{LS}+0.5\left\{1+\mathrm{erf}\left(\pi^{1/2}x_2/\delta_{\omega,0}\right)\right\}\left(f_{US}-f_{LS}\right)$, where subscripts "LS" and "US" illustrate the lower stream and upper stream, respectively. $\delta_{\omega,0}$ is the initial vorticity thickness of the shear layer, $\delta_\omega(t)=\Delta U_0\Big/\left|\partial\widetilde{u_{g,1}}/\partial x_2\right|_{max}$, in which $\Delta U_0=|U_{LS}-U_{US}|=2U_0$ and the tilde "$\tilde{}$" designates a Favre-averaged quantity, $\widetilde{f}=\overline{\rho_g f}\,/\,\overline{\rho_g}=\left\langle\rho_g f\right\rangle\Big/\left\langle\rho_g\right\rangle$. "$\bar{}$" and "$\langle\ \rangle$" are used for Reynolds-average interchangeably in this chapter. The initial velocities $u_{g,2}$, $u_{g,3}$, and vapour mass fraction Y_v are set to 0. Both two-dimensional (2D) and three-dimensional (3D) instabilities are excited through an initial vorticity perturbation (Rogers & Moser 1992; Moser & Rogers 1993), which is transformed into a velocity perturbation through a Jacobi iterative solver (Miller & Bellan 1999). The relative amplitudes of the spanwise F_{2D} and streamwise F_{3D} perturbations are set to 0.1 and 0.0875, respectively. The water droplets are randomly distributed in the lower half domain with the gas oxidizer according to the specified number density profile, with initial droplet velocity $\mathbf{v}_{d,0}$ and temperature $T_{d,0}$ identical to the local gas velocity $\mathbf{u}_{g,0}$ and ambient temperature $T_{g,0}$, respectively.

For both continuum and discrete phases, periodic boundary conditions are set in the streamwise and spanwise directions, while adiabatic slip walls imposed in the cross-stream direction. The spatial derivatives are numerically solved by a 6th-order compact Pade scheme for the inner Cartesian grid nodes, while 4th- and 3rd-order compact schemes for the near-boundary and boundary nodes. To suppress numerical errors at the highest wave numbers, a 4th-order compact filter with coefficient α=0.4983, similar to that used by Pantano & Sarkar (2002), is applied once every 32 time steps to the conservative variables for cases in which coarse grids are used. The gas properties at the droplet locations are obtained by a 4th-order

Lagrangian interpolation scheme. The droplet source terms are allocated onto the Eulerian grid nodes according to a geometrical weight factor (Sirignano 2005; Miller & Bellan 1999). Three methods for droplet source term allocation have been compared, *i.e.*, (1) distribution onto the nearest grid node, (2) distribution according to a volume weight factor, and (3) Method (2) plus a further "smoothing" procedure (Miller & Bellan 1999). No systematic difference was found among these three methods, and Method (2) has been adopted due to its clearer physical meaning. Droplets are assumed to be completely evaporated and removed from the droplet list when its Stokes number reaches 0.075 (Miller 2001). Time advancement is achieved by a 3rd-order Runge-Kutta method with the CFL number set to 1.5. The kinematical, thermal and evaporating responsive time scales of the droplets are all closely related to the Stokes number St, and thus the ratio of the time step Δt to the characteristic droplet time scale, $\Delta t/St$ in the non-dimensional context, for every droplet is monitored throughout the whole simulation period and found to be smaller than 1 for all the cases. More details on mathematical, physical models and numerical procedures can be found in Chapter II.

For all the cases, the initial Reynolds number is $Re=\rho_{g,0}\Delta U_0\delta_{\omega,0}/\mu=500$; the convective Mach number $M_c=U_0/c_0=0.5$, where c_0 is the initial speed of sound for both streams; the Prandtl number Pr and Schmidt number Sc are assumed to be a constant of 0.697; the ratio of specific heats $\gamma=1.4$; the viscosity μ is constant. To account for finite-rate chemistry, an Arrhenius reaction is employed (Luo 1999). However, in order to deploy limited (but nonetheless substantial) computational resources for the key objectives of droplet effects, a simple one-step global reaction is used, together with a set of "representative" combustion parameters: the Damkohler number $Da=5$, Zeldovich number $Ze=3$, heat release parameter $Q_h=7.5$, and adiabatic flame temperature $T_f=4$. The latent heat of vaporization of water is $h_{fg}=19.16$ with the reference temperature being the normal boiling temperature of water (Miller *et al.* 1998).

The computational domain contains two disturbance wavelengths, *i.e.*, $L_x=2\lambda_x$ and $L_z=2\lambda_z$, in both the streamwise and spanwise directions, where $\lambda_x=1.16(2\pi)\delta_{\omega,0}$ and $\lambda_z=0.6\lambda_x$

(Rogers & Moser 1992; Moser & Rogers 1993). L_y=1.25L_x, which was found to be sufficient to minimize the effect of the slip wall boundaries on the main flow in the central domain. Table IV-1 presents the key parameters, in which St_0, MLR_0 and $N_{d,0}$ denote the initial Stokes number of droplets, $St_0 = Re\,\rho_d D_d^2/(18\mu)$, initial mass loading ratio, $MLR_0 = 2N_{d,0}m_{d,0}/\left(\rho_{g,0}L_xL_yL_z\right)$, and initial droplet number in the domain, respectively. For most of the cases listed, the computational grid consists of $n_x \times n_y \times n_z = 192\times192\times100$ points, while for Cases Ad and C1d, which are designed for the purpose of grid-independency check, the number of grid points are doubled in each direction, *i.e.*, $n_x \times n_y \times n_z = 384\times384\times200$. To limit the computational cost, only Cases A and C1 have been tested for grid resolution independence. The grid spacing is uniform in each direction. Statistics of the post-transition flow (t>80) shows that the ratio of the Kolmogorov scale η to the grid spacing $\eta/\max(\Delta x, \Delta z)$ is within the range [3, 4] for all the coarse-grid cases. Figure IV-1 shows the records of extrema of key variables for Case pairs A-Ad and C1-C1d. Excellent matching between the coarse- and fine-grid cases can be seen, indicating that the coarse grid resolution is sufficient and the numerical procedures are sound. Comparing the $T_{g,max}$ curves for the paired cases A-Ad and C1-C1d, it is clear that the presence of evaporating droplets reduce the peak gas temperature.

IV.C Results and Discussion

The instabilities, transition and interactions between turbulence and combustion in reactive mixing layers have been comprehensively studied by Luo (1999). Chemical heat release tends to inhibit the 2D flow instabilities, *i.e.*, the large-scale vortex roll-up and pairing, and thus the mixing layer growth rate as measured by the momentum thickness or vorticity thickness δ_ω. In the present studies, the presence of evaporating water droplets is found to retard the development of δ_ω. Smaller droplets (St_0=1) are more influential than large ones (St_0=4), for the same MLR_0, due to more efficient evaporation (see Fig. IV-2) through more exposed surface areas. However, in the case of C3 (St_0=4), MLR_0 is very large, and the mix-

ing layer growth is severely delayed. Therefore, all cases except C3 are approximately self-similar beyond time $t>80$, and the period $80<t<100$ is chosen for calculating statistics in later sections.

Figure IV-2 illustrates the evaporation rate as expressed by the change in total liquid droplet mass in the computational domain normalized by its initial value. The evaporation process is slow initially, due to low gas temperature and little mixing. Evaporation accelerates rapidly at just over $t=50$ when mixing between the two streams and between gas and the liquid droplets has happened to a significant extent and considerable heat has been released from the chemical reaction. Comparing the paired Cases B1-B2 or C1/C1d-C2, it is seen that the evaporation rate is not linearly proportional to MLR_0. This is more clearly demonstrated by the fact that at $t=100$ Case C3 has an evaporation rate of less than 6% compared to about 24% for Cases C1/C1d, even though Case C3 has eight times more droplets initially. For the same MLR_0, smaller droplets (smaller Stokes number) tend to have a higher evaporation efficiency but the relationship is not linear either (compare Cases B1 and C1 or B2 and C2). Therefore, there are complex nonlinear relations among evaporation, turbulence and chemical reactions, which are further discussed in later sections. It is noted that the results of Cases C1 and C1d agree with each other perfectly, further demonstrating grid-resolution sufficiency.

Figure IV-3 presents the instantaneous interactions between evaporating droplets and the reacting flow in the central spanwise plane for Case B2 at $t=100$. Previous studies have examined the roles of large-scale flow structures, turbulence, the Stokes number, etc. on the dynamics of particles (Squires & Eaton 1990; Ling *et al.* 2001) and evaporating droplets (Xia *et al.* 2008). Preferential concentration or segregation has been found in all cases, with smaller particles/droplets being affected by the flow field much more than the bigger particles/droplets. How droplets dynamics and evaporation affect turbulence and combustion is still poorly understood. Case B2 is scrutinized here, because there are a large number of droplets in the domain and the unity Stokes number ensures intense interactions of the droplets with the flow and combustion processes. The mixing layer at time $t=100$ exhibits typical features of turbulence, with the presence of some large coherent structures, well de-

veloped small scales and intermittency. In Fig. IV-3a, the stoichiometric mixture fraction Z_{st} lines are traces of the initial interfaces between the fuel and oxidizer streams. All intense reactions zones are located along the Z_{st} lines and in the vicinity. Droplets are seen to be preferentially concentrated along the Z_{st} lines, effectively interacting with combustion. Not surprisingly, these zones are also where the mass fraction of vapour Y_v is high. The fact that the reaction zones are non-continuous and can form isolated "islands" suggests that reactions at some locations may have been quenched by evaporating droplets. In Squires and Eaton (1990), particles of $St\sim1$ were found to be clustered in high-strain-rate areas while avoiding the high vorticity regions. The second invariant of the deformation tensor Π_d was proposed to distinguish these two types of regions for particle distribution. In regions where $\Pi_d>0$, the magnitude of vorticity is dominant while for $\Pi_d<0$, the magnitude of strain rate is dominant. Shown in Fig. IV-3b are regions of $\Pi_d>0$ and $\Pi_d<0$ along with the droplet distribution. It is noted that there are virtually no droplets in regions with $\Pi_d>0$. On the other hand, droplets exist in regions of either $\Pi_d<0$ or $\Pi_d=0$. The conditionally averaged droplet number density $\langle n_d | \Pi_d \rangle$ at this time is very close to 0 where $\Pi_d>0$ but shows a peak at $\Pi_d\approx-0.45$, within the section $-\delta_\omega/2<y<\delta_\omega/2$ over the whole domain, as shown in Fig. IV-4. Finally, red solid contours in Fig. IV-3a and IV-3b show that high reaction rate ω_T zones correspond to high scalar dissipation rate χ regions, underlining the importance of micromixing in enabling combustion. The vice versa is not true, suggesting that combustion may be quenched by excessive scalar dissipation or it requires more than just well-mixed mixture to react.

Figure IV-5 shows the mean gas temperature $\langle T_g \rangle$ and reaction rate $\langle \omega_T \rangle$ against the normalized cross-stream coordinate y/δ_ω at $t=100$ for all the cases. The mean value is obtained by averaging the ensemble samples in homogeneous planes. It is noted that the paired Cases A-Ad and C1-C1d have excellent agreement in $\langle T_g \rangle$, respectively, demonstrating good simulation accuracy. The agreement in $\langle \omega_T \rangle$ between Cases C1 and C1d is less good in the peak regions, but is acceptable considering how sensitive $\langle \omega_T \rangle$ is to any small variation in the simulation. One prominent feature is that the presence of evaporating droplets

in all cases reduces the peak reaction rate and temperature significantly. The St_0=1 droplets are more effective in these aspects, because they are more able than larger droplets to concentrate in the high shear regions, which happen to coincide with the intense reaction zones. Also the droplet number density is higher at St_0=1 than at St_0=4, for the same MLR_0. Increasing MLR_0 from 0.1 to 0.2 leads to a significant reduction in $\langle T_g \rangle$ and $\langle \omega_T \rangle$. Further increasing MLR_0 to 0.8 (*i.e.* Case C3) has little effect on the peak values of $\langle T_g \rangle$ and $\langle \omega_T \rangle$, due to poor evaporation (see Fig. IV-2). However, the large MLR_0 in Case C3 changes the profiles of $\langle T_g \rangle$ and $\langle \omega_T \rangle$ from double-hump and multiple-hump of other cases, respectively, into a single peak profile. This is attributed to the fact that the large droplet size (St_0=4) and high MLR_0 in Case C3 significantly reduces the spread of the mixing layer as measured by the vorticity and momentum thicknesses, causing reactions to occur in a narrow central region.

To further investigate the droplet effects on mixing and reaction, the conditionally averaged scalar dissipation rate $\langle \chi | Z \rangle$ is presented in Fig. IV-6. $\langle \chi | Z \rangle$ is a key quantity required for flamelet models (Bilger 1976), Conditional Moment Closure (CMC) models (Bilger 1993) and models based on Probability Density Function (PDF) approaches (Pope 1985) for non-premixed flames. The data shown were obtained by a method similar to that used by Pantano *et al.* (2003): the mixture fraction space is split into 32 bins, and conditional average is first performed in each homogeneous plane *x*-*z*. It is then averaged over the cross-stream direction within $-\delta_\omega/2<y<\delta_\omega/2$ and over 21 time units (t=80-100), as weak dependence of $\langle \chi | Z \rangle$ on y and t was found for all the cases studied. No data for C3 are displayed, as the case has few data in the statistically stationary regime. For Cases A-Ad without droplets, $\langle \chi | Z \rangle$ has a value of around 0.001 over the range of $0.2<Z<0.8$. Considerable modelling simplification can be obtained by assuming Z-independence of $\langle \chi | Z \rangle$ in this range. However, this may not help much in reality as Z_{st} is typically less than 0.2 for hydrocarbon fuels. In the present setup, the oxidizer stream, which is initially laden with droplets, is represented by the range $0<Z<Z_{st}=0.5$. Generally speaking, Fig. IV-6 shows that the pres-

ence of evaporating droplets tends to increase $\langle \chi | Z \rangle$, which is consistent with findings in Réveillon and Vervisch (2000) that the *unconditional* scalar dissipation rate is increased by *fuel* evaporation (note the subtle differences from the present study). Once again, smaller droplets (St_0=1, Case B1) seem to be more effective in augmenting $\langle \chi | Z \rangle$ than bigger droplets (St_0=4, Case C1), for the same MLR_0. When MLR_0 is doubled (Case B2), there is a substantial increase in $\langle \chi | Z \rangle$. Both trends indicate that the more droplets there are and the more evaporation there is, the larger the effect on $\langle \chi | Z \rangle$. These can be understood as follows. The momentum exchange through the drag force, etc. between the droplets and the gas flow occurs at small scales, which tends to enhance turbulence and consequently the scalar fluctuations. Evaporation of non-reactant droplets, in the meantime, tends to alter the local scalar concentration, making the gradient of the mixture fraction larger. Both effects lead to larger scalar dissipation rate. Once again, the matching of the profiles between paired Cases A-Ad or C1-C1d is good.

In models of turbulent non-premixed combustion, the Favre-mean mixture fraction $\widetilde{Z}$ and its variance $\widetilde{Z''^2}$ are two key parameters (Veynante & Vervisch 2002). Réveillon and Vervisch (2000) analyzed evaporation source terms for the transport equation of $\widetilde{Z''^2}$ in the context of spray combustion, and Sreedhara and Huh (2007) provided further data of the source terms in 2D decaying turbulence. Analysis has not been performed before for the case of non-reactant droplets in the context of combustion dilution or fire suppression by water droplets, as in the present study. A balance equation for $\widetilde{Z''^2}$ for the present case can be derived, following the procedures and notations in Réveillon and Vervisch (2000) as follows:

$$\partial \overline{\rho} \widetilde{Z''^2} / \partial t = P + D + I_{\mathrm{v}} + II_{\mathrm{v}} + III_{\mathrm{v}} \qquad \text{(IV.1)}$$

where P=-$2\overline{\rho}\widetilde{Z'' u''_{\mathrm{g},i}}\,\partial \widetilde{Z} / \partial x_i$ is the production, $D = -\overline{\rho\chi} = -2\mu/(ReSc)\overline{|\nabla Z''|^2}$ the dissipation, and the vaporization-related source terms are: $I_{\mathrm{v}} = 2\overline{\rho}\widetilde{Z''\dot{W}_{\mathrm{v}}} Z_{\mathrm{st}}$, $II_{\mathrm{v}} = -2\overline{\rho}\widetilde{Z''\dot{W}_{\mathrm{v}}}\widetilde{Z}$ and $III_{\mathrm{v}} = -\overline{\rho}\widetilde{Z''^2\dot{W}_{\mathrm{v}}}$. Following the practice in Réveillon and Vervisch (2000), we group

the source terms as: $\overline{\rho}\widetilde{S^+} = I_v + II_v = 2\overline{\rho}\widetilde{Z''\dot{W}_v}\left(Z_{st} - \widetilde{Z}\right)$ and $\overline{\rho}\widetilde{S^-} = III_v$. It is noted that $\overline{\rho}\widetilde{S^+}$ here contains $Z_{st} - \widetilde{Z}$ whereas Eq. (20) in Réveillon and Vervisch (2000) has $1 - \widetilde{Z}$ in the parenthesis. This apparently small difference, however, masks real difference in the effect of $\overline{\rho}\widetilde{S^+}$ on $\widetilde{Z''^2}$. In both Réveillon & Vervisch (2000) and Sreedhara & Huh (2007), $\overline{\rho}\widetilde{S^+}$ was found to be always positive, that is, a source term in spray combustion in homogeneous decaying turbulence. The terms in Eq. (IV.1) from the present shear-layer turbulence are shown in Fig. IV-7 for Case C3 at t=100. The other droplet cases show similar trends and are not presented here. It is seen that term I_v is positive on the oxidizer stream side but negative on the fuel stream side. This is different from the findings in Réveillon & Vervisch (2000) and Sreedhara & Huh (2007), in which the correlation $\widetilde{Z''\dot{W}_v}$ was always positive. One explanation might be that in homogeneous decaying turbulence where is no production term for turbulence, vaporization is the driving for fluctuations in the mixture fraction so that their correlation is always positive. The present shear flow is more complex with an additional shear production of mixture fraction fluctuations, and the sign change in $\widetilde{Z''\dot{W}_v}$ across the layer reflects that. The sign of term II_v is just opposite to that of I_v across the mixing layer. Interestingly, the combined term $\overline{\rho}\widetilde{S^+}$ is nonnegative everywhere, just as found in Réveillon & Vervisch (2000) and Sreedhara & Huh (2007). Especially, $\overline{\rho}\widetilde{S^+}$ =0 at the location where the stoichiometric mixture fraction Z_{st} is found. Term $\overline{\rho}\widetilde{S^-}$ has very small magnitude compared with that of $\overline{\rho}\widetilde{S^+}$, as reported in Réveillon & Vervisch (2000) and Sreedhara & Huh (2007). Compared with the production and dissipation terms, however, $\overline{\rho}\widetilde{S^+}$ is one order of magnitude smaller. Finally, terms of $\overline{\rho}\widetilde{S^+}$ and $\overline{\rho}\widetilde{S^-}$ integrated over the cross-stream direction over the time period $80 \le t \le 100$ for Cases B1, B2, C1, C1d and C2 are shown in Fig. IV-8. The integrated quantities are useful to show the net contribution of source/sink terms to transported quantities (Luo 1999) such as $\widetilde{Z''^2}$. Figure IV-8a shows $\overline{\rho}\widetilde{S^+}$ is dependent more on MLR_0 than on St_0, and doubling MLR_0 generates approximately doubled $\overline{\rho}\widetilde{S^+}$. Figure IV-8b shows smaller droplets (St_0=1) produce bigger

$\overline{\rho}\widetilde{S^{-}}$ for the same MLR_0. With the same St_0, increasing MLR_0 will increase the magnitude of $\overline{\rho}\widetilde{S^{-}}$ but less than two proportionally. Again, the paired Cases C1 and C1d show that the coarse-grid curves compare well with the fine-grid results.

IV.D Chapter Summary

Combustion diluted by evaporating droplets has been studied using DNS. The chosen configuration is a temporally-developing reacting shear layer with the oxidizer stream laden with evaporating droplets. The gaseous phase is described in the Eulerian frame while the discrete droplet phase is treated in the Lagrangian frame, with strong two-way coupling between the two phases through mass, momentum and energy exchange. Grid-resolution-independent results have been obtained in cases without and with droplets. A comprehensive parametric study has been conducted by varying the initial Stokes number (St_0) and mass loading ratio (MLR_0).

Using the case of unity St_0 as an example, detailed field analysis has been conducted to examine the complex nonlinear interactions among droplet dynamics, evaporation, turbulence and combustion, and so on. Droplets are found to cluster in high-strain-rate areas while avoiding the high-vorticity regions, in agreement with previous findings. As the high-strain-rate regions coincide with intense reaction zones, evaporating droplets of unity St_0 are very effective in reducing the peak reaction rate and peak temperature. Flow quantities such as the vorticity thickness are also strongly affected by the droplets. In particular, the conditional scalar dissipation rate is enhanced by evaporating droplets, which suggests that they can promote micromixing and combustion under certain conditions, in addition to their roles in combustion suppression. Other findings include: (a) Droplets of non-unity St_0 are less able to follow flow structure; (b) For the same MLR_0, smaller droplets tend to have a greater effect on flow and combustion due to their larger droplet number density and more complete evaporation; (c) Increasing MLR_0 not only reduces peak reaction rate and peak temperature but also significantly changes the profiles of reaction rate and temperature; and (d) Increasing MLR_0 beyond a certain critical vale will reduce the evaporation efficiency.

Finally, the transport equation for the mixture fraction variance $\widetilde{Z''^2}$ has been analyzed, with a focus on the vaporization-related source terms. Such source terms exhibit more complex local variations in the present shear-flow configuration, compared with the homogeneous decaying turbulence configuration of Réveillon and Vervisch (2000). However, the overall effects of these terms are similar to those found in Réveillon and Vervisch (2000), with a positive source term $\overline{\rho}\widetilde{S^+}$ and a negative sink term $\overline{\rho}\widetilde{S^-}$ especially after integration over the cross-stream direction. The source term $\overline{\rho}\widetilde{S^+}$, however, is one order of magnitude smaller than the production and dissipation terms, unlike the situation found in Réveillon and Vervisch (2000).

Table IV-1: Simulation Parameters. Re=500, M_c=0.5, Pr=Sc=0.697; Da=5, Ze=3, Q_h=7.5; h_{fg}=19.16; $L_x=2\lambda_x$, $L_y=1.25L_x$, $L_z=2\lambda_z$, and $\lambda_x=1.16(2\pi)\delta_{\omega,0}$, $\lambda_z=0.6\lambda_x$.

Cases	St_0	MLR_0	$N_{d,0}$	$n_x \times n_y \times n_z$
A	-	0	0	192×192×100
Ad	-	0	0	384×384×200
B1	1	0.1	935,010	192×192×100
B2	1	0.2	1,870,020	192×192×100
C1	4	0.1	116,880	192×192×100
C1d	4	0.1	116,880	384×384×200
C2	4	0.2	233,760	192×192×100
C3	4	0.8	935,010	192×192×100

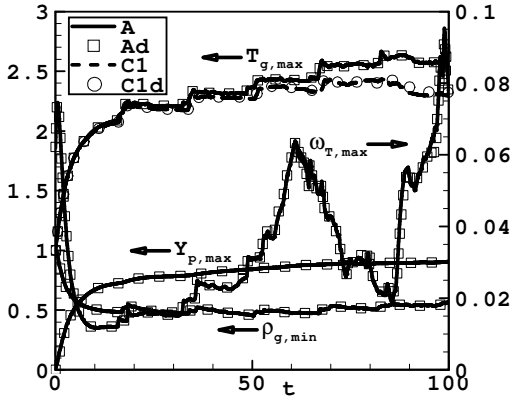

Figure IV-1: Time records of extrema of some key variables, showing grid-independence. Gas density minimum $\rho_{g,min}$, product mass fraction maximum $Y_{p,max}$, reaction rate maximum $\omega_{T,max}$, gas temperature maximum $T_{g,max}$, of the reacting mixing layer are shown for coarse-grid Case A and fine-grid Case Ad, along with $T_{g,max}$ records for droplet Cases C1 and C1d.

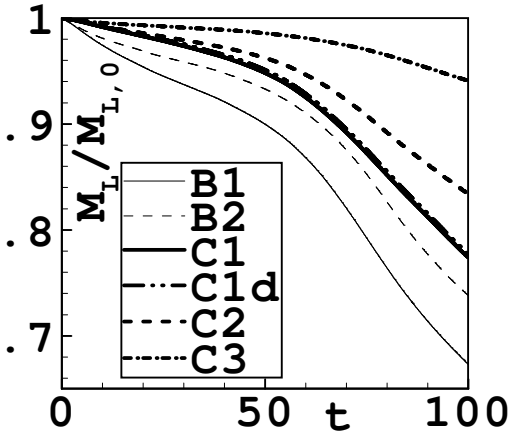

Figure IV-2: Illustration of the evaporation rate expressed by the change in total liquid droplet mass M_L in the computational domain normalized by its initial value $M_{L,0}$.

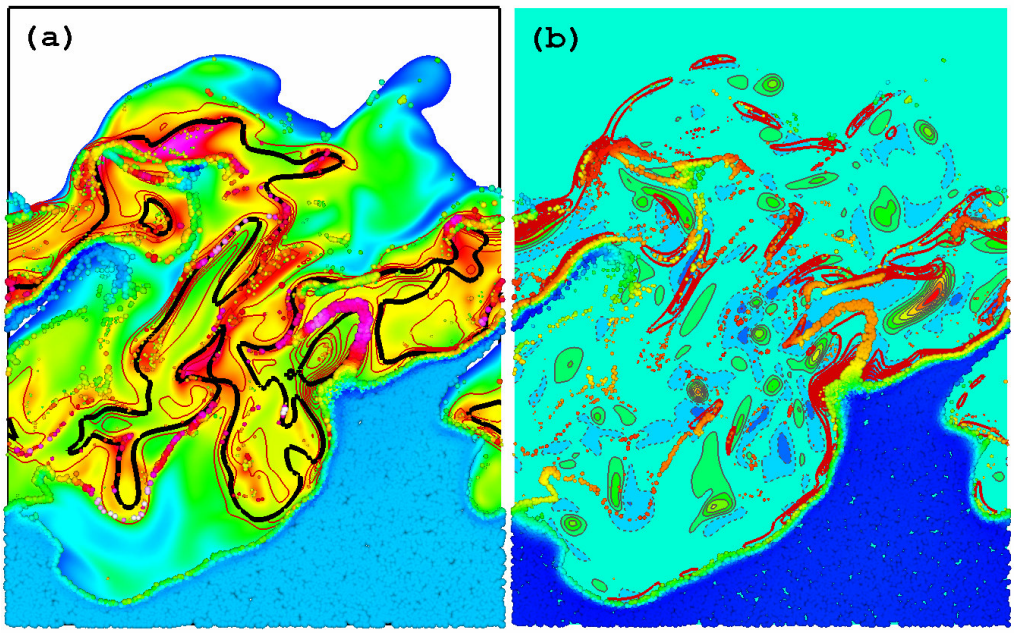

Figure IV-3: Instantaneous interactions between evaporating droplets and the reacting flow in the central spanwise plane (z=L_z/2) at t=100 for Case B2. In (a): the reaction rate ω_T is plotted by thin red contour lines, the stoichiometric mixture fraction Z_{st} by bold black lines, the vapour mass fraction Y_v by flooded contours, and droplets represented by discrete spheres. The droplets are scaled by diameter D_d and coloured by evaporation rate $\dot{m}_d$. In (b): the scalar dissipation rate χ is plotted by bold red contour lines, and the second invariant of the deformation tensor (Squires & Eaton 1990) Π_d by flooded contours. Regions with Π_d>0 and Π_d<0 are encircled by thin solid and dashed lines, representing high-vorticity and high-strain rate, respectively. In other regions Π_d≈0. Droplets are superimposed with their colours indicating the instantaneous droplet temperature T_d.

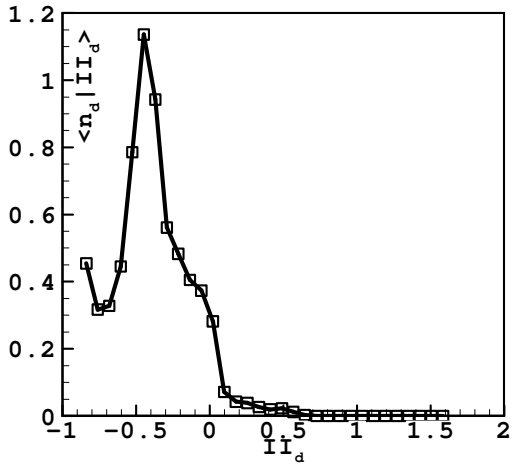

Figure IV-4: The droplet number density conditionally averaged on the second invariant of the deformation tensor $\langle n_{\mathrm{d}} | \Pi_{\mathrm{d}} \rangle$ for Case B2 at t=100.

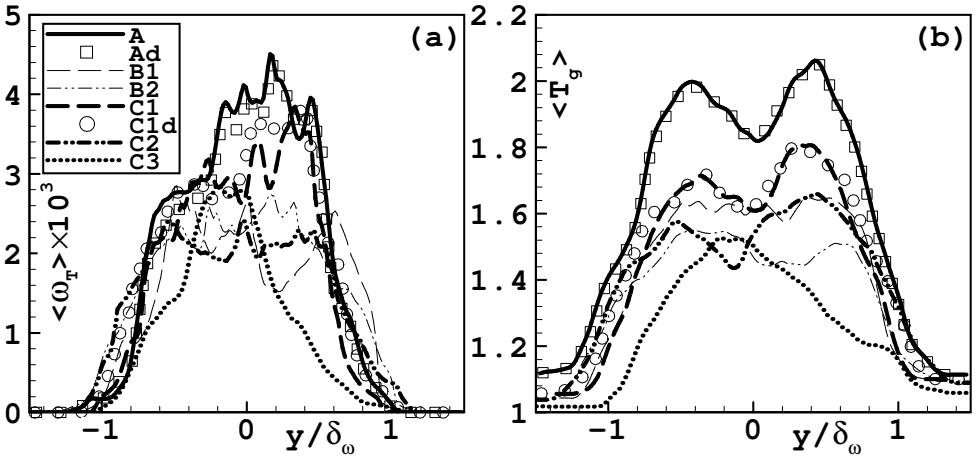

Figure IV-5: Profiles of the mean reaction rate $\langle \omega_{\mathrm{T}} \rangle$ and gas temperature $\langle T_{\mathrm{g}} \rangle$ for all cases at t=100.

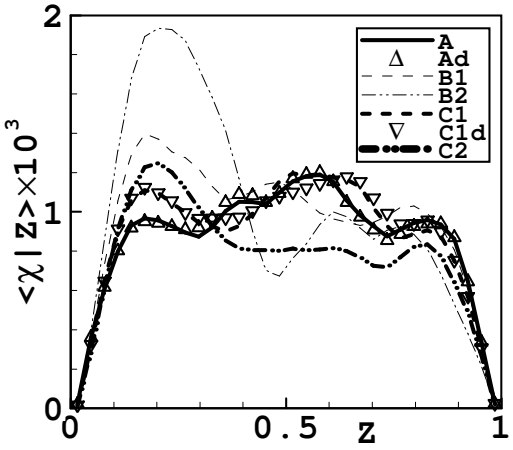

Figure IV-6: The scalar dissipation rate χ conditionally averaged on the mixture fraction Z.

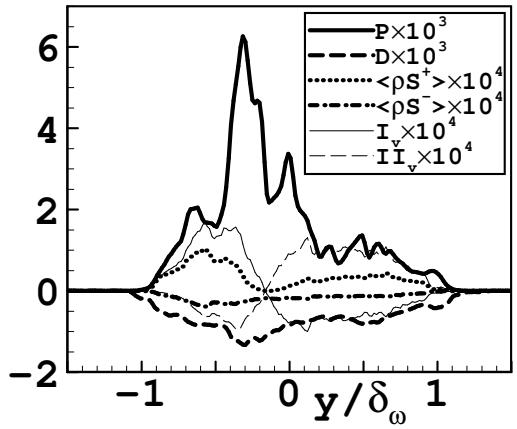

Figure IV-7: Production (P), dissipation (D) and vaporization-related sources in the transport equation of $\widetilde{Z''^2}$ for Case C3 at t=100.

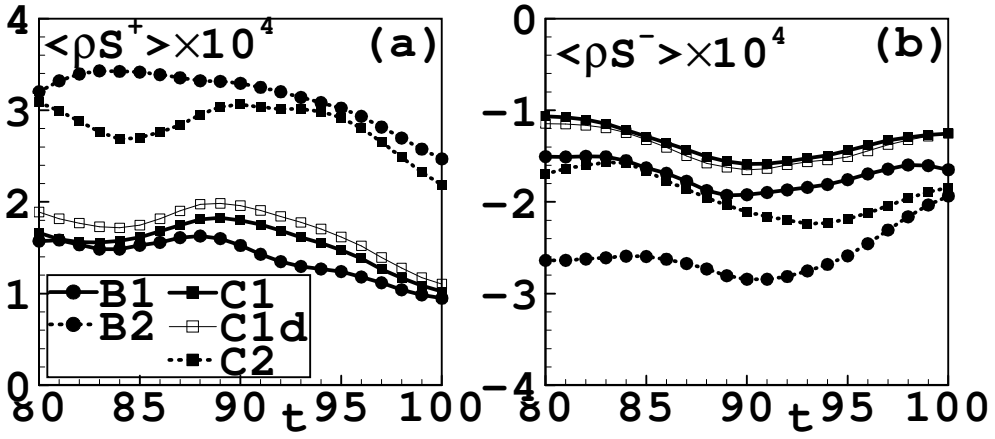

Figure IV-8: Integrated vaporization-related source term $\langle \rho S^{+} \rangle$ and the sink term $\langle \rho S^{-} \rangle$ for the balance equation of the mixture fraction variance $\widetilde{Z''^2}$.

Chapter V – LES of Turbulent Diffusion Flames Diluted with Water Droplets

V.A Introduction

Multiphase reactive flows appear in a multiplicity of engineering applications, such as water/steam diluted gas turbine combustors (Jonsson & Yan 2005) and fire suppression systems (Grant *et al.* 2000), in which complex unsteady interactions exist among vortex dynamics, entrainment, mixing, turbulence, combustion and evaporating droplets at vastly disparate scales. The problem is also scientifically interesting and computationally challenging. Nevertheless, a systematic understanding of such multiscale, multiphysics systems is still far from being achieved.

Numerical simulations of multiphase flow with or without combustion are still facing enormous challenges, as particles and droplets involved are usually much smaller than the Kolmogorov scales, the smallest scales in pure gas flow. To simulate the dispersed phase from the first principles, a Lagrangian approach tracking a millions of particles or droplets is required, which must include particle/droplet inter-collisions as well as interactions with the continuum phase. To describe the continuum gas phase, Direct Numerical Simulation (DNS) is the most accurate method, which resolves all scales down to the Kolmogorov scales. Recently, DNS of a spatially developing reactive planar mixing layer has been performed to study the effects of fine solid particles on flow turbulence with the assumption of no temperature variation (Michioka *et al.* 2005). On the other extreme, the least accurate is the Reynolds Averaged Navier-Stokes (RANS) approach which only computes the mean flow quantities while modelling the entire turbulence spectrum with turbulence models.

For example, the effects of turbulence on vaporization, mixing and combustion of liquid-fuel sprays were investigated using RANS by Sadiki *et al.* (2005). Compared with DNS and RANS, Large-Eddy Simulation (LES) is a compromise between computational cost and simulation accuracy, which is under rapid development for reacting (Janicka & Sadiki 2005) and multiphase (Boivin *et al.* 2000) flow simulations. LES simulates the large-scale flow motions accurately but model the small-scale flow motions (usually much larger than particles and droplets), *i.e.*, subgrid-scale (SGS) motions. Correctly dealing with the SGS phenomena is important for chemical reaction, particles and/or droplets. A variety of models have been proposed for SGS combustion in gas flow (Pitsch 2006). To account for the effects of particles/droplets at the SGS level requires further mathematical (Shotorban & Mashayek 2005) or physical (Segura *et al.* 2004) models. These multiphase SGS models, however, introduce modelling uncertainties (Okong'o & Bellan 2004), which needs clarification. The SGS flow effect on the statistics of non-settling colliding particles suspended in steady homogeneous isotropic turbulent flow was recently investigated by Fede and Simonin (2006). Interestingly, they found that various statistics, such as particle dispersion, particle kinetic energy and fluid kinetic energy were weakly dependent on the SGS gas velocity field. Similar findings had been obtained by Armenio *et al.* (1999) in the numerical study of a turbulent channel flow laden with tracer particles. However, for phenomena driven by the interaction between particles and the local fluid velocity, it was found that the importance of SGS flow effect was dependent on the particle size (Fede & Simonin 2006). Therefore, careful validation of LES results is crucial. However, few experiments provide results at the SGS level and in any case comparison of LES results with existing experimental data is more difficulty than intuition suggests (Veynante & Knikker 2006; Kempf 2008). An alternative route is validation against the DNS data (Okong'o & Bellan 2004; Leboissetier *et al.* 2005). Unfortunately, for three-dimensional (3D) spatially developing multiphase reactive flows as in the present study, DNS is still prohibitively expensive for present supercomputers. The third option is to conduct systematic parametric studies to reveal the trends predicted by the LES in comparison with as much theoretical and experimental results as possible. This option is adopted in the present study.

Fundamental numerical studies on multiphase phenomena have in the past adopted an idealized homogeneous (Mashayek 2000) or two-dimensional (Miller 2001) flow in the laminar and transitional regimes. For spatially evolving flows, the gas-solid non-reactive isothermal jet has been investigated extensively with numerical and experimental techniques (Yuu *et al.* 2001), with a focus on particle effects on gas-flow turbulence, *i.e.*, turbulence modulation. With the addition of chemical reaction and phase change, the vast majority of studies are concerned with spray combustion, which has applications in modern gas turbine engines and Diesel engines. Vapour effect in the spray combustion has been considered in the context of RANS (Réveillon & Vervisch 2000), LES (Pera *et al.* 2006) and DNS (Wang & Rutland 2007), respectively.

In the present chapter, a 3D turbulent reactive jet laden with non-reactive evaporating liquid droplets is studied using LES. The main objective is to investigate the suppressive effects of non-reacting water droplets on combustion. The applications include control of combustion peak temperature using water spray in gas turbine engine technology (Jonsson & Yan 2005) as well as fire suppression in the context of fire safety (Grant *et al.* 2000). The physical problems involved and objectives are different from those in spray combustion, in which the evaporating droplets take part in combustion, and the evaporation and mixing enhance combustion. The LES approach uses a dynamic procedure to obtain six subgrid model coefficients in order to capture the highly local interactions among turbulence, combustion, heat transfer and evaporation. The complex interactions are scrutinised under various initial Stokes number (St_0) and Mass Loading Ratio (MLR_0).

V.B LES Code Validation

A heated planar jet studied experimentally by Yu & Monkewitz (1993) has been simulated by LES for the purpose of code validation. Their motivation is to investigate the near field flow dynamics and the absolute instability of a hot jet. The main parameters are Re=4000, S=0.76 and Ri=3×10^{-3}, where the Richardson number Ri is defined as

$$Ri = \frac{g^* h^*}{U_0^{*2}} \frac{1-S}{S} = \frac{1}{Fr} \frac{1-S}{S} \tag{V.1}$$

The corresponding Froude number is about 105, so the buoyancy effect is insignificant in the near field of the hot jet. The computational domain is chosen as $L_x \times L_y \times L_z = 4 \times 9 \times 15$, and the grid system $n_x \times n_y \times n_z = 40 \times 90 \times 150$, leading to the uniform grid spacing 0.1, or dimensionally 1.5*mm*, in all the three directions. The sponge layer starts at z=12. No perturbation is employed for the streamwise and lateral velocity components at the inflow plane, as in the experimental setup, while random periodic sinuous waves are imposed on the spanwise velocity component to trigger the 3D effect.

Figure V-1 shows the direct comparison of the instantaneous scalar fields. The "T" frame in the experimental figure is to show the size of the slot jet nozzle width. The flow transition takes place at about z=2~2.5, which is well captured by the LES results. The correct reproduction of the location and size of the first pair of rolling-up large-scale vortices shows the satisfactory performance of the dynamic Smagorinsky model for transitional free shear flows. The global flow characteristic in the near field of the hot jet is also very similar between the computational and experimental results. The random spanwise perturbation takes effects at downstream locations. As shown in Fig. V-2b, the "mushroom" structures start to appear at z=8, and the corresponding streamwise vorticity drives the flow to develop non-symmetrically (Fig. V-1a), compared with the purely symmetrical flow pattern in the upstream regions. Figure V-3 shows the temperature iso-surfaces at t=100. Note the computational domain has been expended in this figure, *i.e.*, $L_x \times L_y \times L_z = 8 \times 31.8 \times 42.785$ with $n_x \times n_y \times n_z = 41 \times 160 \times 200$, to show the developed turbulence downstream. The flow field develops from a laminar flow at the inflow, forming large scale vortices at $z \approx 10$, and subsequently breaking up into small scale structures at $z \approx 20$.

The mean streamwise velocity and temperature profiles are presented in Figs. V-4 and V-5. Due to the low sensitivity of the probe at the low velocity regions, the ambient velocity data were not given in Fig. V-4b. The centreline velocity decay rate is well predicted by the LES results. However, the centreline temperature decay rate was found to be underesti-

mated by LES, which could be for various reasons. The most important one, in the author's opinion, is due to the inflow boundary condition. From the experimental point of view, it is always difficult to prescribe the desired inflow condition due to the environmental noise, the inherent experimental device vibrations, *etc.* On the other hand, from the numerical point of view, to give a well-posed inflow boundary condition, one flow variable should be treated as a "soft" variable and determined by the flow itself during the course of simulations (Poinsot & Lele 1992). Here, the density ρ is used for this purpose. Although the direct effect on the temperature statistics is expected to be diminished compared to an inflow BC in which the temperature itself is a "soft" variable, the variation of ρ at the inflow plane definitely affects the downstream temperature decay more severely than it affects the downstream flow velocity.

The one-point temporal velocity spectra are shown in Figs. V-6. Two peaks can be found at non-dimensional frequency (Strouhal number) equal to 0.2 and 0.3. It should be emphasized that these results are obtained without any artificial excitations at the jet nozzle. The experimental results revealed a similar tendency. However, in the region close to the nozzle, *i.e.*, z=1, Fig. V-6b shows the peak magnitude at Sr=0.3 dominates, while for the LES results, the dominant peak locates at Sr=0.2 for both heights, z=1 and 2, which indicates that the jet develops from the shear layer mode into the jet mode more quickly in LES. The one-point temporal temperature spectrum is shown in Fig. V-7. The Sr=0.3 peak dominates at a further downstream location compared to the velocity spectra, which suggests the self-similar status of the temperature will be attained later than that of the streamwise velocity. The experimental temperature spectra were not given for this case.

Compared to the first-order quantities, the second-order statistics suffer more uncertainties at the inflow BC, for instance, the unknown turbulence level at the jet nozzle in experiments. A recorded experimental profile is desirable in such a case. While this problem was found to have little influence on the mean quantities, it does have obvious effect on the second-order statistics according to the results of some test cases.

The comparison to the experimental results of a heated plane jet presented in this subsection is far from completed for the purpose of validation for a LES code simulating multi-phase reacting flows. The reasons for further validation is not pursued are two folds. First, well-established experimental data are still not available. This is due to the complexity of the flow and the limitation of the currently available experimental technology and methods. A good example was given by Bilger (2004), discussing the quality of measurement of scalar dissipation rate, and other turbulence statistics. The spatial resolution of the measurement was the key issue. The discrete evaporating droplets entail more difficulty in the measurement. Moreover, well-defined experimental results should present the detailed initial, boundary conditions and all the relevant parameters, before the statistics is given. In the third year of this project, an experimental study on turbulent non-reacting spray jets of acetone (Chen *et al.* 2006) was published, which could be considered for further validation.

Second, to numerically resolve the multi-scale flow is beyond the capability of current computational power. Despite this, the grid-independency tests have been performed in Chapter IV for DNS of a reacting shear layer interacting with droplets, showing the self-consistency of the DNS results. For LES, apart from the imperfect evaporation model for a single droplet and combustion models for gas reactions which are still under development, the current knowledge of subgrid characteristics of the interaction between reacting flows and discrete droplets is too little to perform a comparison with a realistic configuration using LES.

To this end, our strategy is to use simple models for evaporation and combustion, and concentrate on exploring the interaction mechanisms involved with the help of parametric studies. Parameters are calibrated and tuned to reproduce the main features of laboratory flames diluted with or suppressed by non-reacting droplets, *e.g.*, the gas temperature and the vapour mass fraction, and to make the simulations tractable with the available computing resources. Various simplifications have been imposed in past numerical studies (Miller & Bellan 1999, Mashayek 2000, *etc.*) to circumvent the same issue. More importantly, specific interaction is better explained by simplified configuration. A good example was given by

Réveillon and Demoulin (2007), who studied the interaction between evaporation and micro-mixing. Step-by-step improvement can be made in the future work.

V.C The Gas-Liquid Reactive Jet Configurations

A 3D free turbulent reactive planar jet laden with non-reactive evaporating liquid droplets has been simulated under different conditions shown in Table V-1. Figure V-8 presents the schematic of the computational domain and boundary conditions. The coflow is quiescent. The domain size is chosen as $L_x \times L_y \times L_z = 8 \times 31.8 \times 42.785$, where the subscripts x, y and z designate the spanwise (periodic), lateral and streamwise direction, respectively. A sponge layer starting from z=40 is added to the outflow boundary in order to suppress any unphysical wave reflections at the boundary. The slot jet nozzle at the inflow plane is of a rectangular shape, with width l_y=1 and length l_x=8. A Cartesian grid system $n_x \times n_y \times n_z = 41 \times 160 \times 200$ leads to uniform grid spacing in each direction, respectively, *i.e.*, $\Delta x \times \Delta y \times \Delta z = 0.2 \times 0.2 \times 0.215$. The grid spacing $\left(\overline{\Delta}/2\right)$ is chosen so that the cut-off wavenumber is within the inertial subrange of turbulent scales, as shown in the one-dimensional streamwise velocity spectra in Fig. V-33 (discussions on the figure deferred to later sections). Magnitudes of quantities such as resolved (ke_r) and subgrid (ke_s) kinetic energies, grid- (D_g) and subgrid-scale (D_s) dissipation rates were monitored in time and space to ensure a well-resolved LES, *i.e.*, $ke_r >> ke_s$ and $D_g << D_s$ (da Silva & Métais 2002). In the present study, the biggest droplet size $D_{d,0,max} \approx 8.5 \times 10^{-3}$, which is far smaller than the grid size, indicating that the prerequisite for the point source approximation is well fulfilled. The peak value of the local volume fraction of droplets in all the droplet cases is below the critical value of 1×10^{-3}. The dispersed phase is thus in the dilute two-phase flow regime (Crowe *et al.* 1996), and consequently droplet-droplet collisions can be neglected. Droplets enter the computational domain with the fuel jet through the slot nozzle after t=20, when the jet flame has been ignited and established in downstream regions. When a droplet leaves one end of the periodic boundary, a new one with identical properties as the leaving one is put at the corresponding

position at the other end. The simulations were performed on a Linux cluster Iridis2 at the University of Southampton using 40 processors. The parallel algorithm is based on Message Passing Interface (MPI) with the non-blocking communication mechanism.

V.D Results and Discussion

V.D.1 Combustion LES with Dynamic SGS Models

The simulation cases and parameters are listed in Table V-I. A one-step, irreversible reaction, described by the Arrhenius law, is used for the reactive cases, with Re=4000, S=0.76, Da=3, Ze=12, T_f=4, Q_h=250. Although the buoyancy effect (Fr=105) was found to be insignificant for the non-reactive hot jet, it does have profound influence on the combustion process of a turbulent reactive jet. Included in Table V-1 are the scenarios with various buoyancy configurations which are of theoretical and practical interests: Case 0a is a non-buoyant flame (Fr=∞), Case 0b a buoyant flame and Case 0c a prototype flow in industrial combustors where the gravitational force is aligned perpendicularly with the jet axis.

Figure V-8 shows the isosurface of vorticity magnitude, 0.25, of Case 0a. The present LES well captures the laminar to turbulence transition, including the first occurrence of the large spanwise vortices, as compared with the experimental results (Yu & Monkewitz 1993). Figures V-9, 10 and 11 present the 3D temperature isosurfaces of the reactive jet and the temperature contours on several cross sections at a representative time for Case 0a, 0b and 0c, respectively. Unlike the infinitely fast chemistry which implies "Mixed is burned", the reaction takes place predominantly in the turbulent region, and the flame is lifted from the jet nozzle. It can be seen that due to the promotion of the mixing effect induced by buoyancy, the reaction becomes much more intensive in Cases 0b and 0c compared to Case 0a. Moreover, the buoyancy is more effective in Case 0c than in Case 0b, since the temperature in Case 0c has reached the same level as in Case 0b, but at an earlier time. Due to the buoyancy effect on vorticity transportation (Jiang & Luo 2000a), the flow structures in Cases 0b and 0c are more "twisted" than in Case 0a, especially in Case 0c, where separated large scale structures produced by the buoyancy can be found in the y>0 region.

It is worth noting that the gravity has evident effect on droplet motion as well, especially for large droplets. As an example, shown in Fig. V-12 are the droplet trajectories for the St_0=16, MLR_0=1.7 droplets of Cases 3d and 3e, respectively. In comparison with Case 3d, where droplets are mainly controlled by inertia and show no directional inclination, all the droplet trajectories for Case 3e bend to the gravity direction. For the purpose of combustion control, since the light and hot gas product mixture will always "rise" toward the anti-gravitational direction, which is opposite to the droplets' destination, the poor performance of large droplets can be anticipated. Other unfavourable characteristics of large droplets, such as insensitivity to the flow behaviour, poor lateral dispersion, *etc.*, will be analyzed in detail in following sections.

Figures V-13a, 13b and 13c are the lateral distributions of dynamic model coefficients for Case 0b at z=15 and 30, representative transitional and turbulent downstream locations, respectively. C_d, C_I, C_T, C_{Yf}, C_{Yo} are the model coefficients in the dynamic Smagorinsky model (Germano *et al.* 1991), Yoshizawa model (Yoshizawa 1986), SGS heat and species flux models (Moin *et al.* 1991). As a reminder, $C_T=C_d/Pr_t$, $C_{Yf}=C_d/Sc_{t,f}$, $C_{Yo}=C_d/Sc_{t,o}$, where Pr_t is turbulent Prandtl number, $Sc_{t,f}$ and $Sc_{t,o}$ are turbulent Schmidt numbers for fuel and oxidizer.

One prominent feature is that these SGS model coefficients are quite non-uniform, especially in the transition regimes, where large coherent structures have big influence. Compared with simulations with constant model coefficients, the present simulation is able to capture the local features, which is important for examining turbulence-droplets-combustion interactions. Figure V-13d shows the ratio of turbulent viscosity (μ_t) to molecular viscosity (μ), which indicates the level of SGS model dissipation compared to the physical dissipation. The maximal levels approach 4 and 5 at the two heights and compare well with other LES studies (Le Ribault *et al.* 1999) under similar configurations, indicating an appropriate selection of grid spacing.

V.D.2 N_R - Number of Physical Droplets Represented by One Computational Droplet

A key issue in LES of two-phase flows by the Lagrangian approach is how to represent a huge number of physical droplets with limited computational resources. A general practice is adopting a "computational" droplet to represent a parcel of physical droplets, which are assumed to have identical properties, *i.e.*, droplet mass, evaporation rate, temperature, velocities, *etc* (Crowe *et al.* 1998). A ratio, N_R, of the physical to computational droplet numbers is defined here and a suitable N_R must be determined. A compromise must be made between numerical accuracy and computational cost, since a big N_R will lessen the simulation burden but tend to affect numerical accuracy, whereas a small N_R will have the opposite effects. It is likely that the choice of N_R is problem-dependent, which should be tested before any final simulation.

There have been only few studies on the effect of N_R on LES results of multiphase flow. The study of Leboissetier *et al.* (2005) is one example, which considered a droplet-laden temporal mixing layer and concluded that the results with N_R=8 were poor. In this study, a more realistic configuration of a spatially-developing reactive jet laden with evaporating droplets is tested using various N_R settings. Figure V-14 presents the effect of N_R on the gas temperature T_g and the product mass fraction Y_p at z=30 and t=100 for Case 3a. Very small differences among the test cases have been found considering the double-peak shape, magnitude and lateral extent of all the predicted profiles. It should be pointed out that similar tests have been done for Case 3d with N_R=8, 16 and 32, and the findings are same as those for Case 3a. No such tests have been done for Case 1a due to the huge computational cost demanded for the droplet phase as N_R decreases. Based on the above tests, N_R is set to 32 for all the cases in the present study, which is expected to retain numerical accuracy while keeping the computational cost tractable.

V.D.3 Diluted Combustion

A comparison of the averaged temperature fields at t=100 for the non-buoyant cases 0a, 1a, 3a and 3d is shown in Fig. V-15. At t=100, a well developed reacting jet diluted with evaporating droplets has been established at downstream locations. As shown, at small MLR_0 (0.1), the fields of droplet Cases 1a and 3a are very similar to that in Case 1a without droplets, in terms of the first vortex roll-up, break-down location and spreading rate, *etc*. However, Cases 1a and 3a have dramatically different effects on combustion and consequently peak temperature due to different droplet sizes. The deployment of more droplets while keeping the droplet size the same results in further suppression, as seen in Figs. V-15c and V-15d for the St_0=16 cases. Since the peak temperature in Case 3d is almost equal to the initial hot fuel temperature, combustion has been fully suppressed. Meanwhile, the lateral spreading of the jet and droplets becomes much less than in other cases, due to the lack of expansion of the mixture of hot reaction products.

Figure V-16 presents the profiles of normalized temperature fluctuation intensities for all cases at selected locations. The peak intensity values for Case 0a appear in the strong reacting area (z>30), with T_{rms} reaching almost 25% of the mean temperature. In all droplet cases, the temperature fluctuation intensity is dramatically reduced, especially in Case 3d, due to the cooling effects of droplets and lack of combustion-induced temperature fluctuations. In the near field (close to nozzle exit), droplets play a role as external disturbances on the laminar flow, which lead to higher level of flow fluctuations (not plotted) and in some locations larger temperature fluctuations. Figure V-16b shows that high values of temperature fluctuation intensity are usually distributed at the interface between the fuel and the oxidizer ambient, where there is strong combustion, similar to the double peak distribution widely observed experimentally.

V.D.4 Effects of the Initial Stokes Number

In Figs. V-17a and V-17b, the droplet distributions are shown for Cases 1a and 3a. Notably, the behaviour of droplets of different St_0 and accordingly different sizes is dramatically different. In Case 1a at the transitional region, the small (St_0=1) droplets follow the flow and

concentrate in the circumferential regions of large scale vortices or high-strain-rate regions, due to their tendency for "preferential concentration" (Squires & Eaton 1990). These are the regions where chemical reactions are strong thanks to better mixing of the fuel and oxidizer. The concentration of droplets there not only reduces the temperature through evaporation, but also separates the fuel from the oxidizer, leading to effective suppression of combustion and thus peak temperature. In the turbulent region downstream, the droplet size becomes even smaller on average, resulting in even more rapid evaporation and effective suppression of combustion, as seen in Fig. V-18b, which shows the Probability Density Function (PDF) profiles of the normalized droplet sizes at two heights, *i.e.*, Z1 = 10±1 and Z2 = 30±1, the typical transitional and turbulent regions. The PDF at Z2 shows that the droplets are smaller and have a wider spread of sizes than those at Z1. For the PDFs calculated with all the droplets in the whole domain at t=100, Fig. V-18a shows that the initially large droplets (Cases 3a and 3d) have evaporated to a lesser extend than in Case 1a. This is partly because smaller droplets (with the same MLR_0) have a larger total surface area, which enhances heat transfer and evaporation. Another reason is that larger droplets are less responsive to the flow field and less likely to concentrate in the regions with strong combustion and thus high temperature. Also shown in Fig. V-18a is that increasing MLR_0 inhibits evaporation of individual droplets, comparing the PDFs of Cases 3a and 3d. However, the total mass of the vapour produced in Case 3d is much more than in Case 3a (not shown), due to 13 times more droplets existing in the whole domain of Case 3d than in Case 3a at t=100. This leads to the different degree of reaction suppression in these two cases, as seen in Figs. V-15c and V-15d.

The different interaction modes between droplets and reaction for different cases are shown in Fig. V-19. A small cube block region, $l_x \times l_y \times l_z = 8 \times 8 \times 8$, in the downstream fully developed turbulent area is magnified for clarity. Mainly controlled by local flow motions, the smaller droplets can follow up and cover the reaction zones in an ideal pattern, as shown in Fig. V-19a. On the other hand, Figs. V-19b and V-19c show that the bigger droplets are confined within a narrow region in the y direction, due to their insensitivity to flow behaviour. In Fig. V-19b, as the bigger droplets pass through the central region, the reaction zones

are torn apart and reaction suppressed. Due to their larger inertia, they do not spread as widely as in Case 1a. Therefore, reaction survives at off-centre regions. In Fig. V-19c, due to the existence of a lot more droplets with MLR_0=1.7 compared to MLR_0=0.1 in Figs. V-19a and V-19b, the combustion is completely controlled (see Fig. V-15d), so the lateral expansion of the reaction becomes much weaker.

It is noteworthy that the gravitational effect has not been taken into consideration. If the gravity is aligned with the negative vertical direction $-z$ as in Luo (2004) and Prasad *et al.* (1998), the penetration distance of droplets will be altered. If the gravity is aligned with the lateral direction as in Xia *et al.* (2006), then the flame structures and droplet trajectories are bent towards in the $+y$ or $-y$ direction, especially for heavier droplets. Shown in Figs. V-20a and V-20b are snapshots of temperature isosurfaces together with the distribution of droplets at t=80 for the buoyant Cases 1b and 3b. The preferential concentration is again discovered for the St_0=1 droplets, with the additional influence of buoyancy on the flame and gravity on the droplets. With turbulence growing and St decreasing by evaporation, the distribution of the droplets becomes more uniform at downstream locations (z>15), but is still selective. On the contrary, the St_0=16 droplets, whose initial droplet size is four times that of St_0=1 droplets ($St_0 \sim D_{d,0}^2$), are prone to keep their initial trajectories due to their large inertia and are insensitive to the flow structures. Consequently, the lateral dispersion, a key parameter for liquid spray combustor or solid coal combustor, of St_0=16 droplets is much smaller than that of St_0=1 droplets. For fire suppression systems, the implication of this disparity is profound too. The reaction typically takes place initially in the shear layers at the interfaces of fuel and oxidizer, and then spreads to nearby regions. With the perfect matching of droplet locations with the reaction zones in Case 1b, the reaction is suppressed before it grows. The mass fraction of water vapour Y_v and the droplet number density n_d for Case 1b at the same time are plotted in Figs. V-21 and V-22. Clearly, the maximal Y_v (>0.015) and n_d are found at low-vorticity and high-strain-rate regions. The total droplet number within the computational domain for Case 1b is 234,350, which represents about 7.5 mil-

lion equivalent physical droplets. The maximal n_d is about 26, *i.e.*, more than 830 physical droplets in one grid volume. The corresponding value for Case 2 is about 4.

The non-uniform droplet distribution in Case 1b has another important consequence as far as the control of combustion is concerned. Because droplets are concentrated in the interface regions between the fuel and oxidizer where the strain rate and reaction rate are both high, the vapour produced by the droplets due to combustion together with the droplets themselves are forming an "insulation" layer, separating the fuel from oxidizer. That would prevent mixing and further reaction, leading to effective suppression of combustion. In reality, such an insulation layer would also reduce the level of thermal radiation, which plays an important role in the feedback mechanism for flame propagation, as in combustion chambers and enclosure fires.

For the St_0=16 droplets, due to their insensitivity to the flow behaviour, their performance of combustion control is quite poor. Their only possible advantage is that they may penetrate deeper into reacting zones, if their initial distribution and trajectories are right. As shown in Fig. V-20b, the droplets missed the targets (intense reaction zones) completely. Naturally, the gravitational force in the negative y-direction changes the droplet trajectories so that the droplets are moving away from the central line. Even without this influence, the narrow distribution of droplets of larger sizes would result in limited interaction between droplets and the reaction zones, as shown in Figs. V-17b, V-19b and V-19c.

Figures V-23, V-24 and V-25 present the centreline gas phase temperature (T_g), reaction rate (RR) and Y_v, averaged over the spanwise direction at t=80 for Cases 1b, 2 and 3b. The initial droplet diameters correspond to 30μm, 60μm and 120μm, respectively, all within the definition of water mist (< 200μm). It can be seen that for same MLR_0, smaller droplets are more effective in suppressing combustion. Figures V-23 and V-24 show that the fine mist in Case 1b almost completely extinguish the combustion, while in other cases combustion is simply moderated. The averaged peak temperature at t=80 is 2.4 for Case 1b, while 3.78 for Case 3b. This is partly due to the different dynamics of droplets of different sizes as discussed above. Another important factor is the total surface area of droplets (A_T) exposed to

the gas. Simple mathematics leads to $A_{T,St=1}/A_{T,St=16}=D_{d,St=16}/D_{d,St=1}=4$ for the same MLR_0. So Case 1b has four times more surface areas than Case 3b, which enhances convective heat transfer and evaporation. As shown in Fig. V-25, Y_v for Case 1b quickly rises to a much higher level compared to the other two cases. At heights beyond *z=20*, there is little vapour in Case 1b partly because combustion is suppressed in that region and partly because there are not many droplets left. Cases 2 and 3b have more uniform distributions of Y_v along the height, for the opposite reasons.

Figure V-26 illustrates the ensemble averaged droplet diameter normalised by its initial diameter along with the vertical distance at t=80. For Case 1b, D_d almost approaches its half value at z>35, showing that about 80% of the droplet mass has been evaporated. In contrast, the decrease in the droplet size for Case 3b is quite small. In Case 2, the averaged droplet size decreases with the height until the intense reaction zone at $z\approx29$. The small number of droplets that escaped from the reaction zone cause a weak peak at z=30-32, because the percentage of vaporised droplets in that range is low.

V.D.5 Effects of the Initial Mass Loading Ratio

With the same St_0, higher MLR_0, i.e., more droplets are expected to result in larger degree of combustion suppression. However, the effect is not linear. Figures V-27, 28 and 29 show the lateral profiles of T_g, RR and Y_v at z=20 for Cases 3b, 3c and 3e. Increasing MLR_0 from 0.1 to 0.85 dramatically decreases T_g and RR but increases Y_v. But increasing MLR_0 from 0.85 to 1.7 has little effect. One main reason is that the evaporation capability does not grow linearly with the droplet number in a given system. The ensemble averaged driving potential of evaporation, $<Y_{v,surf}-Y_{v,far}>$ along the vertical distance is shown in Fig. V-30. As more vapour is produced in higher MLR_0 cases, $<Y_{v,surf}-Y_{v,far}>$ decreases, so further evaporation is slowed down. This is consistent with the description of the three-stage evaporation process of a cluster of fuel droplets by Réveillon and Demoulin (2007). Therefore, the combustion suppression capability of Case 3c and 3e is very similar, despite twice as much water

as used in Case 3e. On the other hand, the lateral extent of *RR* and corresponding T_g is narrower in higher MLR_0 cases, indicating denser mixture due to higher droplet number density inhibits lateral entrainment, mixing and thus combustion.

V.D.6 Droplet Dynamics

The effects of droplets with different initial sizes on the flow field can be scrutinized via the analysis of the grid-scale (GS) kinetic energy budget, which can be written as

$$\frac{D\widehat{k}}{Dt}=\underbrace{-\widetilde{u}_{g,k}\frac{\partial\overline{p}}{\partial x_k}}_{\text{I}}+\underbrace{\frac{\partial\left(\widehat{\sigma}_{ik}\widetilde{u}_{g,i}\right)}{\partial x_k}}_{\text{II}}\underbrace{-\widehat{\sigma}_{ik}\frac{\partial\widetilde{u}_{g,i}}{\partial x_k}}_{\text{III}}\underbrace{-\frac{\partial\left(\overline{\rho}_g\tau_{ik}\widetilde{u}_{g,i}\right)}{\partial x_k}}_{\text{IV}}+\underbrace{\overline{\rho}_g\tau_{ik}\frac{\partial\widetilde{u}_{g,i}}{\partial x_k}}_{\text{V}}\underbrace{-\frac{\widetilde{u}_{g,i}\widetilde{u}_{g,i}}{2}\overline{S}_{ms}}_{\text{VI}}+\underbrace{\widetilde{u}_{g,i}\overline{S}_{mo,i}}_{\text{VII}} \tag{V.2}$$

where $\widehat{k}$ is the grid-scale kinetic energy (GSKE), representing the large-scale flow structure behaviour and playing a key role in entrainment and turbulent mixing, $\widehat{k}=\overline{\rho}_g\widetilde{u}_{g,i}\widetilde{u}_{g,i}/2$. In Eq. (V.2), term I represents the convection of pressure waves, II the viscous diffusion, III the viscous dissipation, IV the redistributive effect due to interactions between SGS stresses and velocities, V the SGS dissipation, VI the SGS effect of droplets due to evaporation, and VII the SGS effect of droplets due to momentum exchange between the two phases. The buoyancy contribution is not included to simplify the analysis.

Figure V-31 presents the contributions of the dominant terms (I, IV, V and VII) in Eq. (V.2) for all the non-buoyant cases at t=100. The combustion-generated pressure gradients due to local thermal expansion lead to the dominance of term I. For a well-resolved LES, the magnitudes of term III should be much smaller than those of term V, which has been correctly captured in all the cases, indicating a proper choice of the grid spacing in the current LES. Moreover, the effect of SGS redistribution of GSKE (term IV) has been found to be much more efficient than the GS redistribution effect (term II), which is consistent with the findings in (da Silva & Métais 2002). Since $\overline{S}_{ms}>0$, VI always acts as a "sink" and tends to decrease the GSKE. However, its magnitude has been found to be too small to trigger any

profound effect on GSKE in all the cases presented here. The droplet term due to momentum exchange (VII) plays different roles depending on the droplet initial sizes, *i.e.*, St_0. For Case 1a, thanks to the small droplet responsive time, the relative velocities between the flow and droplets are small and the effect of momentum exchange on GSKE is negligible. For the opposite reasons, the droplet momentum effect is more pronounced for Cases 3a and 3d. Even with small MLR_0 (0.1), VII has risen to the level of the SGS dissipation term V, but is still smaller than the SGS redistribution term IV. In Case 3d, in which the MLR_0 is much higher, VII becomes the second most important term after the combustion term I. To verify this conclusion, budgets of respective terms have been plotted at different downstream locations, *i.e.*, z=25, 30 and 35, for Case 3d in Figs. V-31d, V-31e and V-31f, respectively. It's worth noting that VII is usually positive, which acts as a source term for GSKE. As a consequence, the GSKE has been dramatically increased due to the existence of larger droplets. This effect is especially evident in the downstream fully developed turbulent region, where the gas streamwise velocity is getting small due to jet spreading and viscous dissipation for Case 0a. Shown in Fig. V-32 are the temporal records of the filtered streamwise velocity, $\tilde{w}$, at a centreline downstream location, $(x, y, z) = (4, 15.9, 32)$, for Cases 0a and 3d, respectively. It can be seen that the time-averaged level of $\tilde{w}$ has been augmented from 0.2 in Case 0a to about 0.6 in Case 3d after droplets reach that location at $t \approx 65$.

Although the GSKE is increased, the turbulence level in the two-phase flow is found to be decreased due to the droplet dynamic effect. As discovered by other researchers (Boivin *et al.* 1998; Okong'o & Bellan 2004), without the consideration of gravitational effect, droplets act as an additional source of dissipation, leading to a diminished turbulence level. Figure V-33 presents the one-dimensional energy spectra based on the centreline streamwise velocity, which has been averaged over the spanwise direction, at t=100. The centreline has been chosen for spectra analysis due to the high droplet number density found there, properly reflecting the droplet effect on the flow turbulence. At both ends of large and small scales, the energy density is found to be lower in Case 3d than in Case 0a. Similar findings can be obtained for other droplet cases with weaker influence on the energy spectra induced by droplets, due to either much smaller relative velocities between the two phases for Case 1a

or fewer droplets for Case 3a. It is worth noting that the temperature level in the downstream turbulent region is much lower for Case 3d than for Case 0a, so the temperature-dependent molecular viscosity is lower for Case 3d as well. With inefficient dissipation, the turbulent kinetic energy (TKE) for Case 3d tends to accumulate and reach a higher level. However, the droplet dynamic effect predominates over the thermal effect due to the viscosity decrease for this case, and thus the turbulence level becomes lower finally.

It should be pointed out that the conclusions drawn in this section have been verified at different downstream locations and time instants.

V.E Chapter Summary

A LES code with dynamic subgrid models has been developed based on the DNS code, DSTAR, of Luo (1999). To validate the code performance, the LES results of a heated planar jet have been compared with the experimental data (Yu & Monkewitz 1993). The instantaneous flow fields are very similar, including the transition location and downstream flow structures. The matching of the mean velocity profiles between the computational and experimental results is better than the mean temperature profiles, with the centreline temperature decay underestimated by the LES. The one-point temporal velocity spectra predicted by the LES agree in principle with the experimental results. It was found that the inflow BCs, *e.g.*, the initial velocity/temperature profiles and fluctuations at the inflow plane, *etc.*, is the most important factor which affects the LES results. Further validation will be carried out if suitable experimental data becomes available.

Parametric studies on LES of a 3D turbulent reactive jet laden with evaporating droplets/mist have been performed to investigate the interaction among turbulence, combustion and evaporating droplets. Dynamic procedures have been adopted in SGS models for all subgrid phenomena, except that the scale similarity model has been used for the chemical reaction rate. The model coefficients and key parameters in the LES are found to be highly non-uniform both spatially and temporarily. The developed LES methodology is able to

capture the localized features, which is essential for studying multiphase combustion systems with strong local interactions.

The dynamics of water droplets interacting reactive jets has been investigated under various Stokes numbers and mass loading ratios (MLR_0). It is found that smaller droplets or mist can seamlessly follow the flow structures into the intense reaction zones, leading to effective suppression of combustion and the peak temperature. Larger droplets are insensitive to flow fields, whose effects on combustion are highly dependent on their initial trajectories and distribution. With the same MLR_0, smaller droplets have a larger total surface area, which increases the evaporation rate and leads to more effective separation of the reaction zones from the oxidiser. For the same droplet size, increasing the MLR_0 level initially leads to strong suppression of combustion. However, further increase in the MLR_0 level beyond a critical value would inhibit evaporation due to reduced driving potential of mass transfer and thus would limit the effect of evaporation in suppression of combustion at high MLR_0's.

Detailed investigation of the grid-scale kinetic energy (GSKE) of the gas phase reveals that the droplet evaporation effect on the GSKE is small, and the droplet momentum effect depends on initial droplet sizes (St_0). Unlike the smaller droplets (St_0=1), the momentum exchange between the two phases is much stronger for the bigger droplets (St_0=16), which can have profound influence on GSKE, and consequently on mixing and entrainment of the flow field, provided that the mass loading ratio is sufficiently high. Although the molecular viscosity is much lower for the droplet cases due to the temperature decrease, droplets exhibit a strong dissipative nature, leading to a weaker turbulence level in the droplet cases than in the pure flame case.

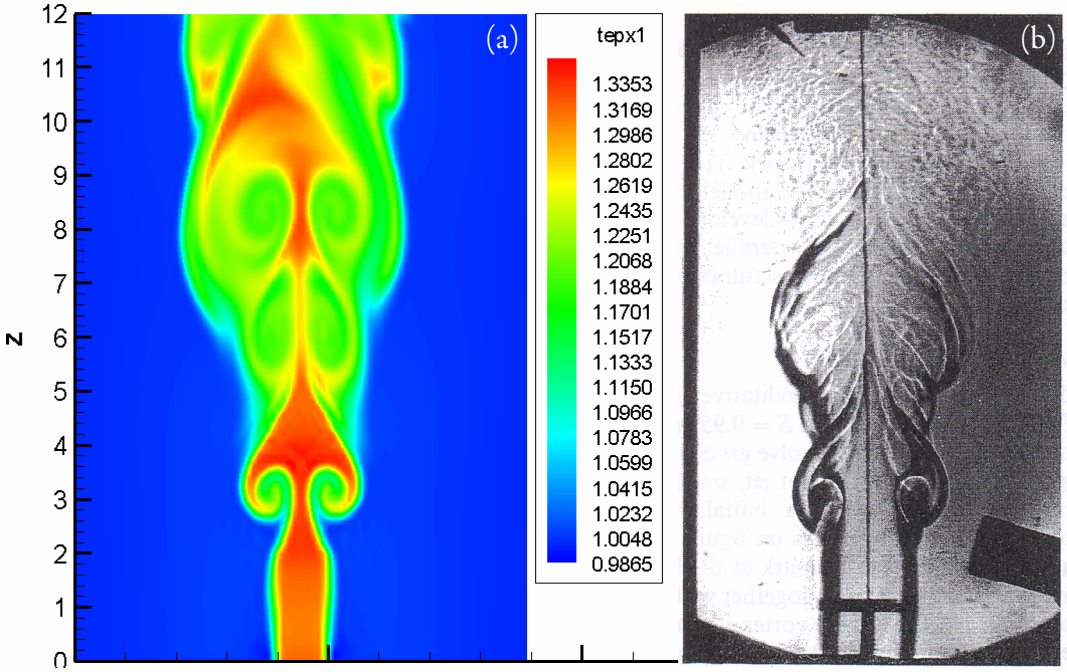

Figure V-1: Instantaneous scalar fields. (a) LES results of the temperature fields at the central plane in the spanwise direction x=2 when t=105; (b) Experimental image (Yu & Monkewitz 1993).

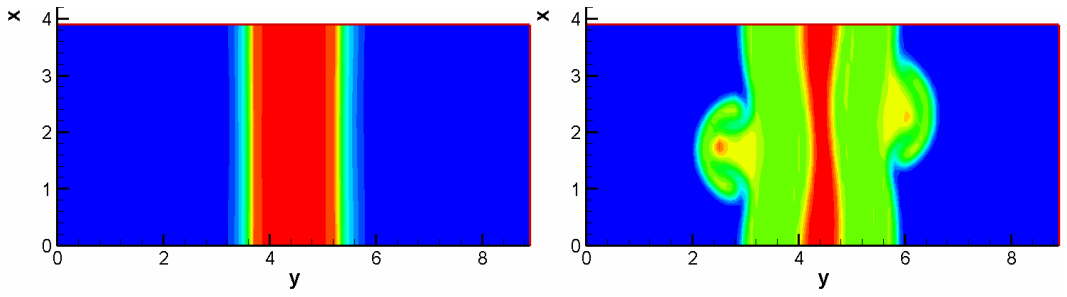

(a) $z = 4$ (b) $z = 8$

Figure V-2: Temperature fields at different vertical planes.

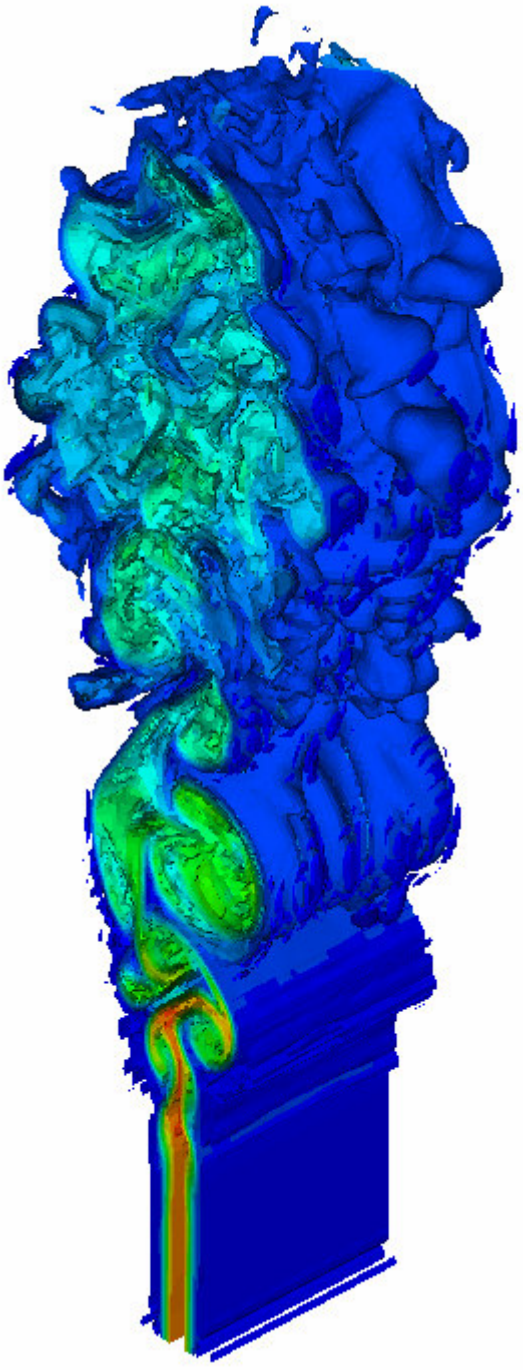

Figure V-3: Temperature iso-surfaces of the hot jet at t=100.

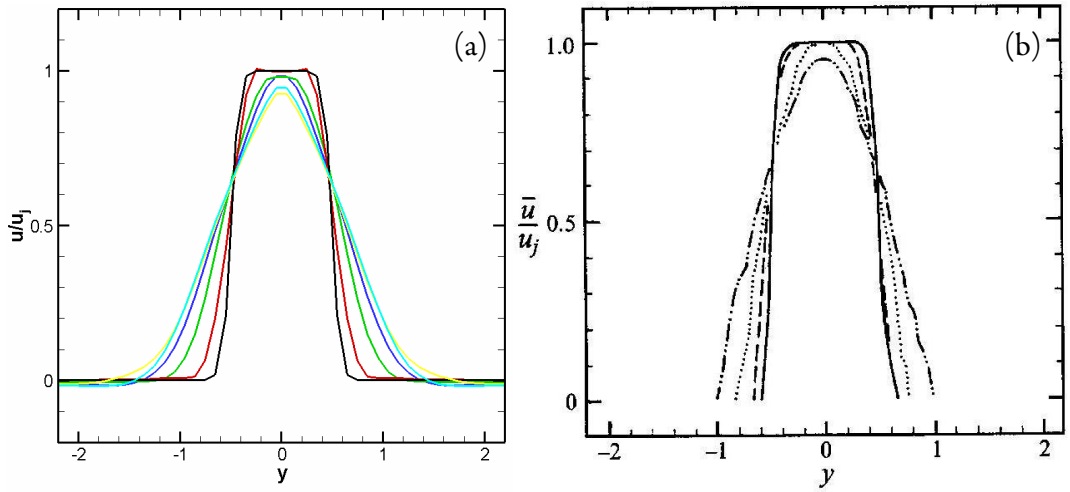

Figure V-4: Mean streamwise velocity profiles. (a) LES results: black – z=0; red – z=2; green - z=4; blue – z=6; cyan – z=8; yellow – z=10. (b) Experimental results (Yu & Monkewitz 1993): solid – z=0, dashed – z=2, dotted – z=4, dashdotdot – z=6.

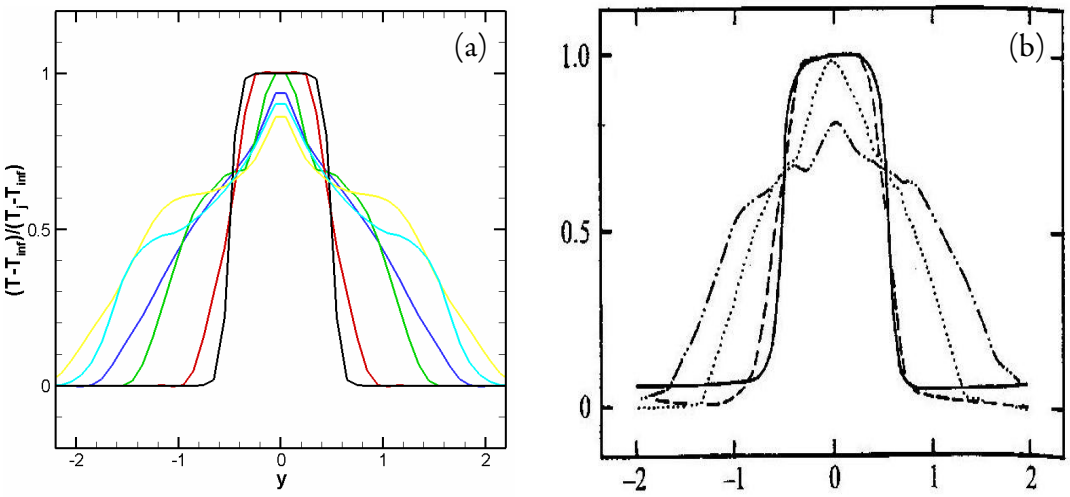

Figure V-5: Mean temperature profiles: (a) LES results; (b) Experimental results (Yu & Monkewitz 1993). See Fig. V-4 for line captions.

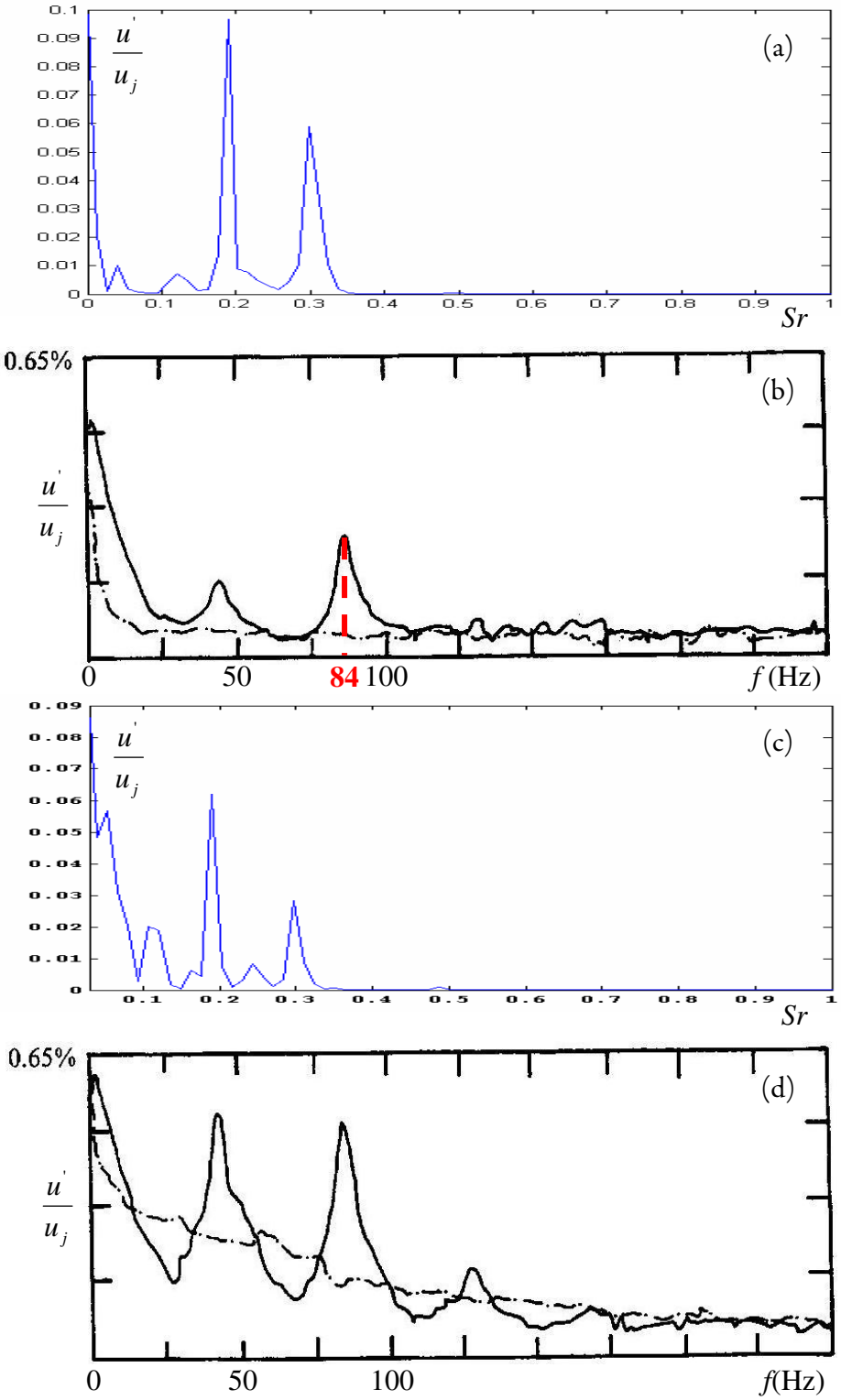

Figure V-6: Streamwise velocity spectra. (a) LES results at point (x=2, y=1, z=1). (b) Experimental spectra at (y=1, z=1) (Yu & Monkewitz 1993). f = 84 Hz corresponds to Sr = 0.3. (c) LES results at point (x=2, y=1.33, z=2). (d) Experimental spectra at (y=1.33, z=2) (Yu & Monkewitz 1993). Solid – Hot Jet, Dashdot – Cold Jet.

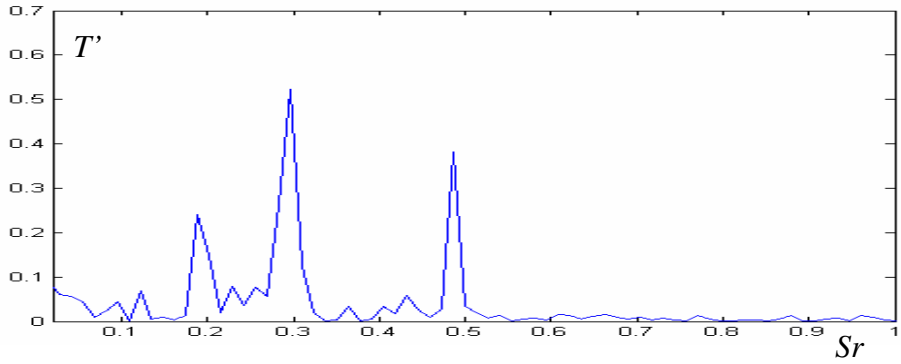

Figure V-7: LES Temperature spectra at point (x=2, y=0.4, z=3).

Table V-1: Simulation Cases and Parameters

Re	S	Da	Ze	T_f	Q_h	h_{fg}
4000	0.76	3	12	4	250	250

Cases	St_0	MLR_0	Fr	Gravitational Direction
0a	-	0	∞	-
0b	-	0	105	negative z
0c	-	0	105	negative y
1a	1	0.1	∞	-
1b	1	0.1	105	negative y
2	4	0.1	105	negative y
3a	16	0.1	∞	-
3b	16	0.1	105	negative y
3c	16	0.85	105	negative y
3d	16	1.7	∞	-
3e	16	1.7	105	negative y

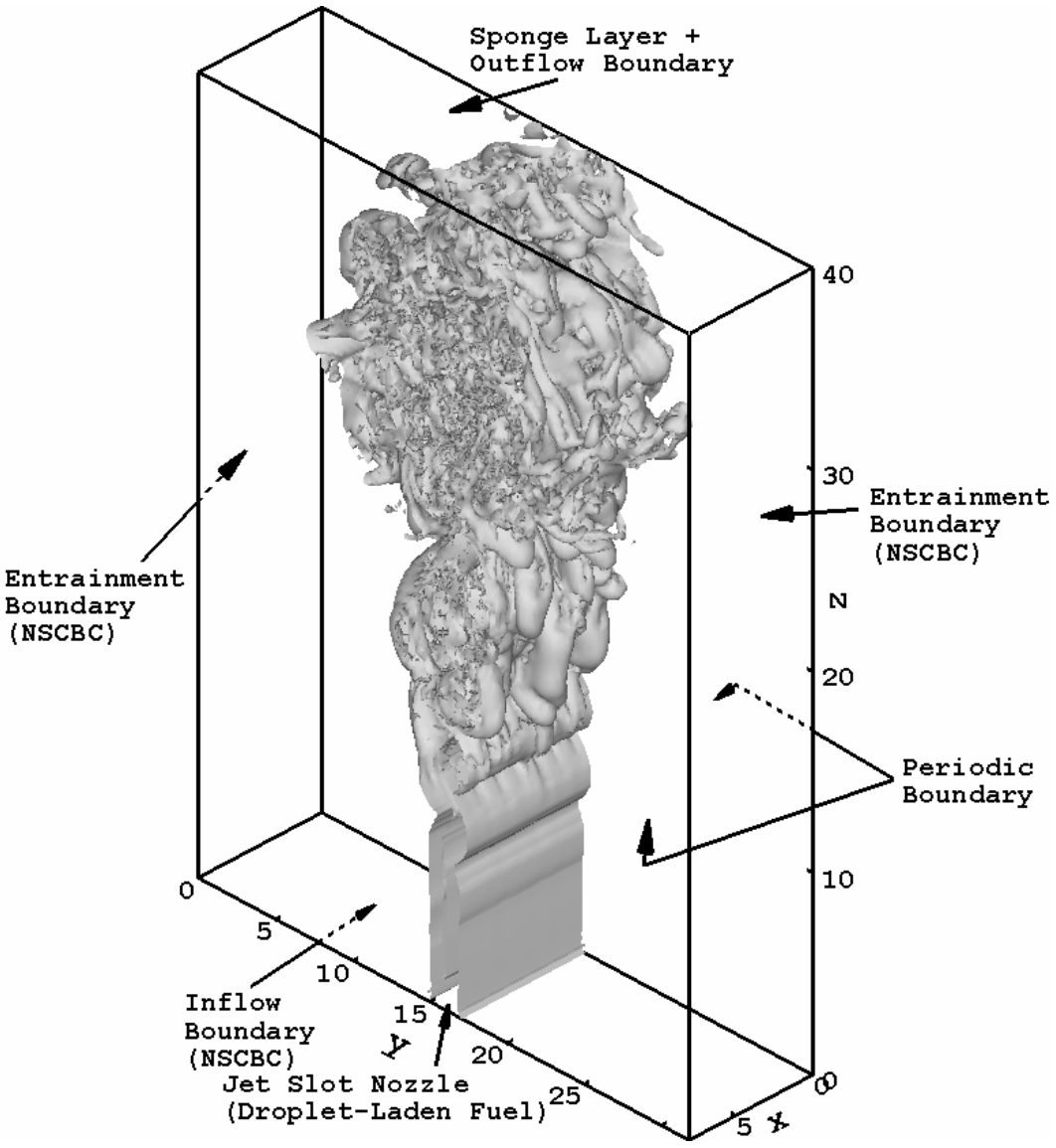

Figure V-8: Schematic of the computational domain, boundary setup and the isosurface of vorticity magnitude (0.25) of Case 0a at t=100.

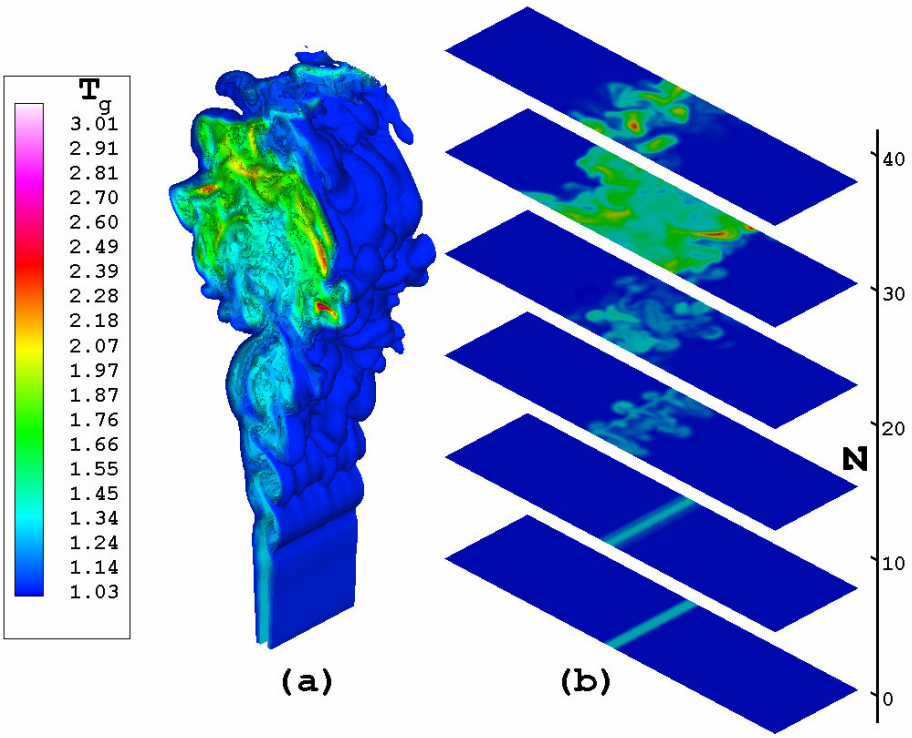

Figure V-9: (a) Temperature isosurfaces of Case 0a at t=100. The green and red colours designate the intermediate and high temperatures, respectively. The blue colour marks the ambient temperature. (b) Temperature contours on selected cross sections.

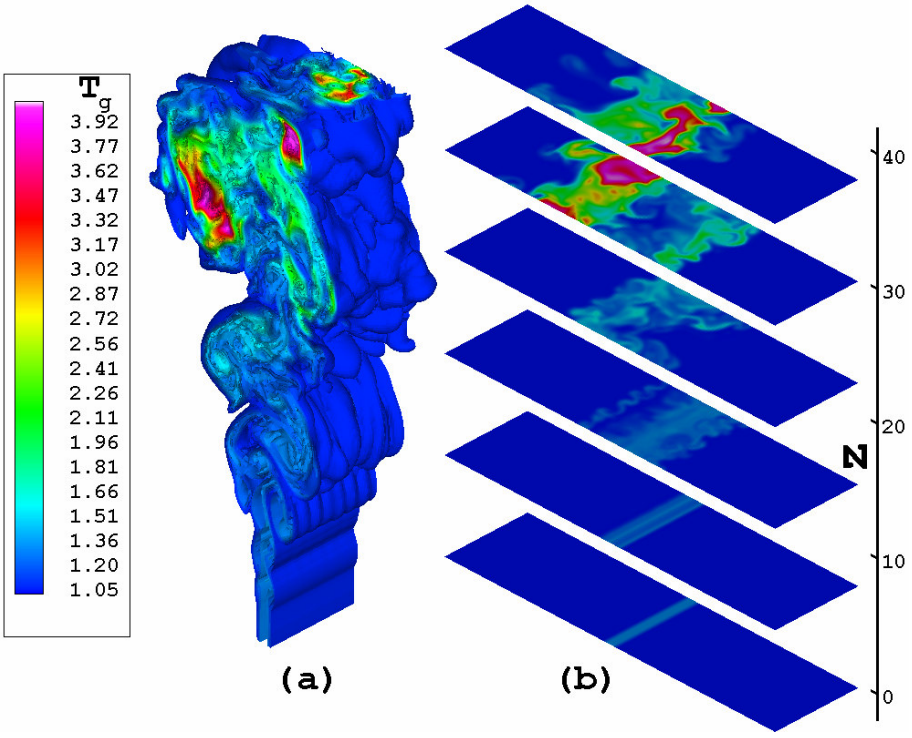

Figure V-10: Temperature isosurfaces (a) and contours on selected cross sections (b) of Case 0b at t=100.

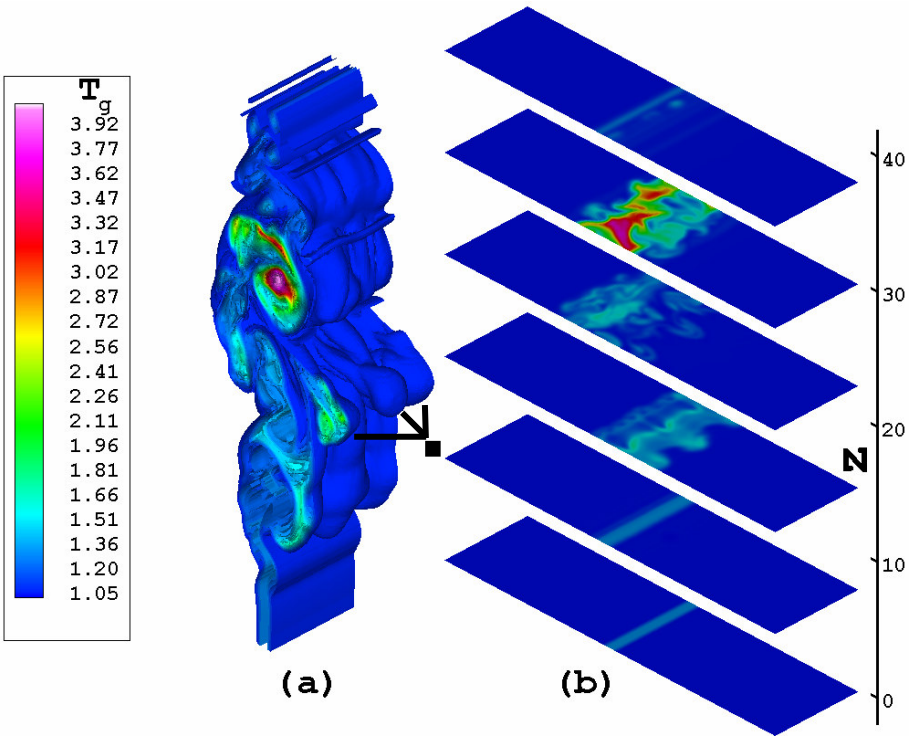

Figure V-11: Temperature isosurfaces (a) and contours on selected cross sections (b) of Case 0c at t=80. (▪ - flow structures induced by buoyancy).

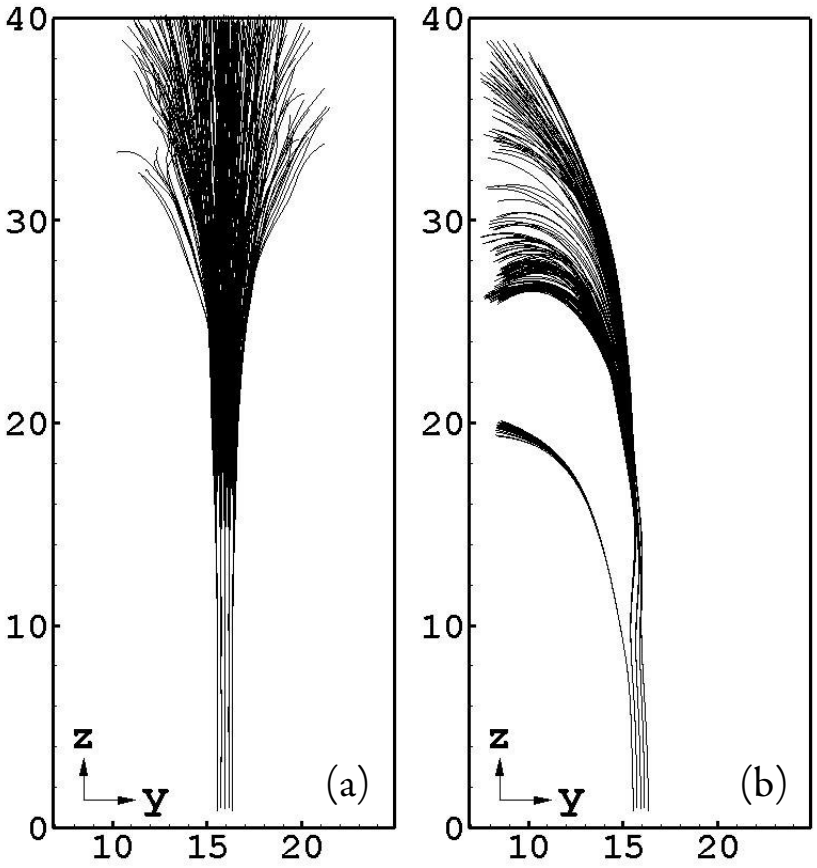

Figure V-12: Droplet trajectories for (a) Case 3d and (b) Case 3e.

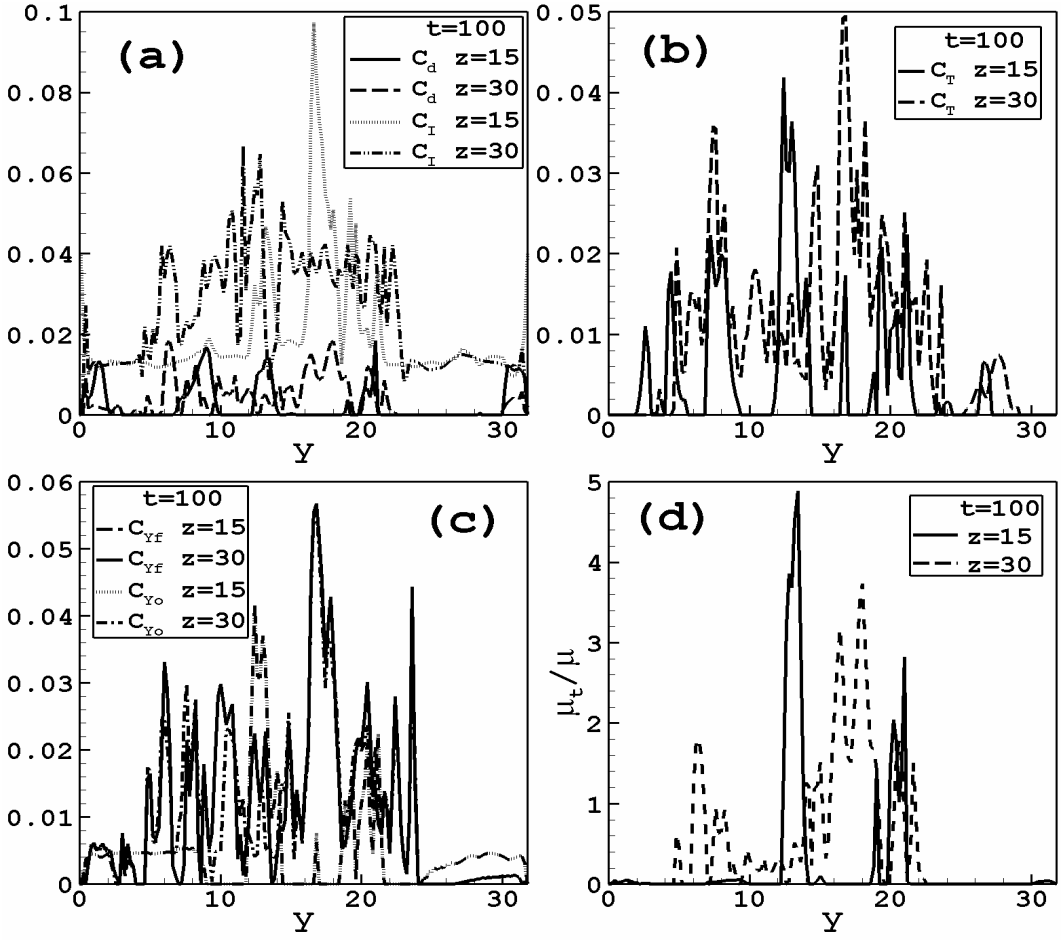

Figure V-13: The lateral distributions of key parameters in the SGS models at z=15 and 30 at t=100. Dynamic model coefficients in (a) momentum equations: C_d and C_I; (b) energy equation: C_T; (c) species equations: C_{Yf} and C_{Yo}; and (d) μ_t/μ.

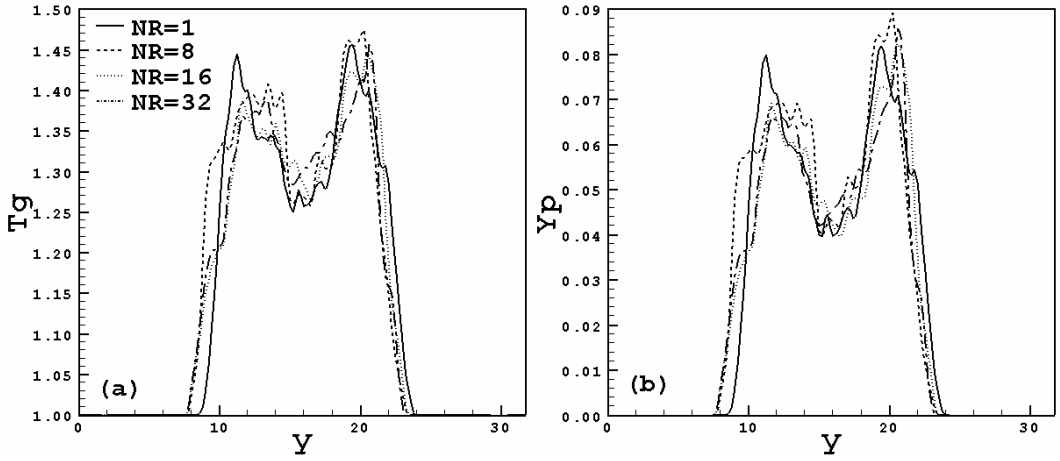

Figure V-14: The effect of N_R on the final LES results at z=30 and t=100. (a) The gas temperature T_g; (b) The mass fraction of the product Y_p. Both profiles have been averaged over the spanwise direction.

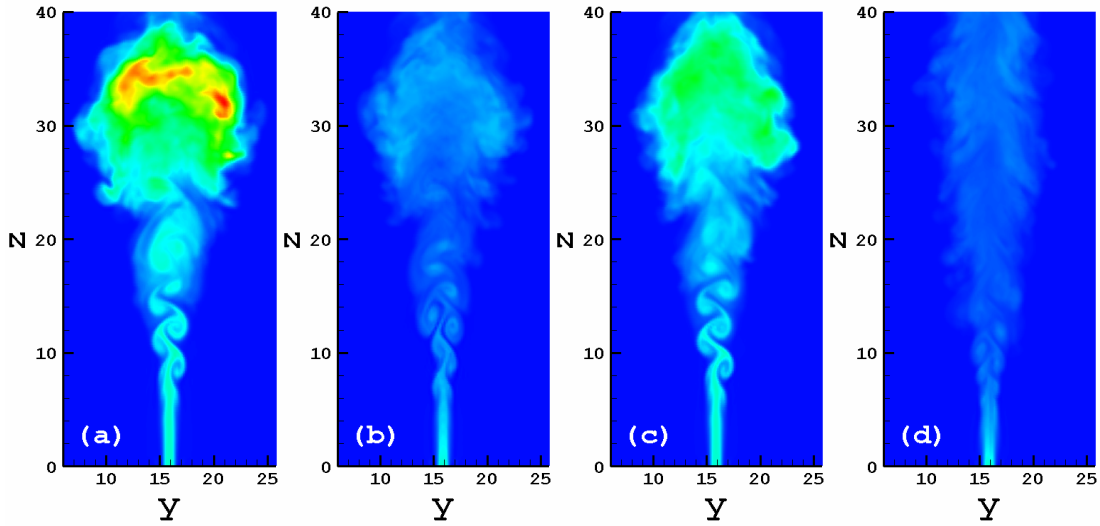

Figure V-15: The temperature fields averaged over the periodic spanwise direction at t=100 for (a) Case 0a, (b) Case 1a, (c) Case 3a and (d) Case 3d. A same temperature scale (1-2.087) is used for all the contour plots. The peak temperature in the whole domain for (a), (b), (c) and (d) is 3.12, 1.39, 2.17 and 1.32, respectively.

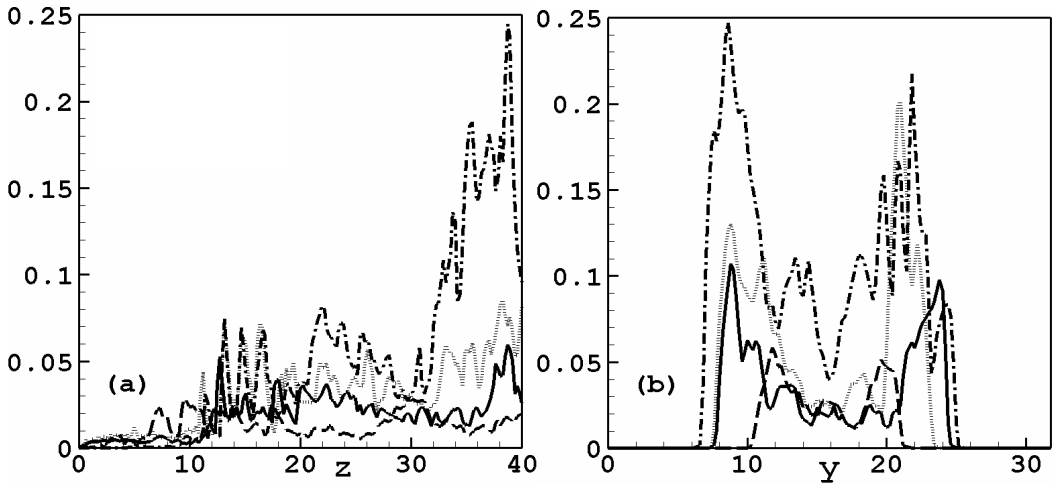

Figure V-16: The normalized temperature fluctuation intensities t=100:

(a) streamwise profile along the jet centreline; (b) lateral profile at z=30.

Dashdot – Case 0a; Solid – Case 1a; Dotted – Case 3a; Dashed – Case 3d.

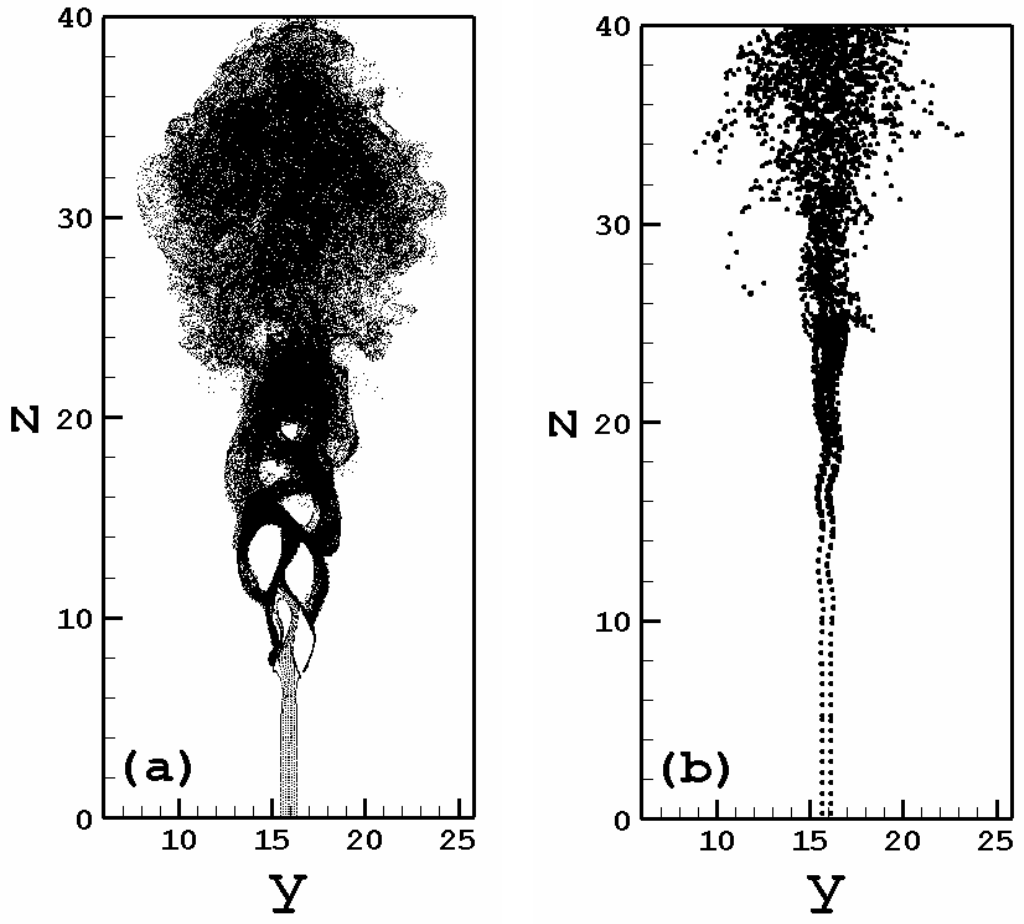

Figure V-17: The instantaneous droplet distribution at t=100 for (a) Case 1a and (b) Case 3a.

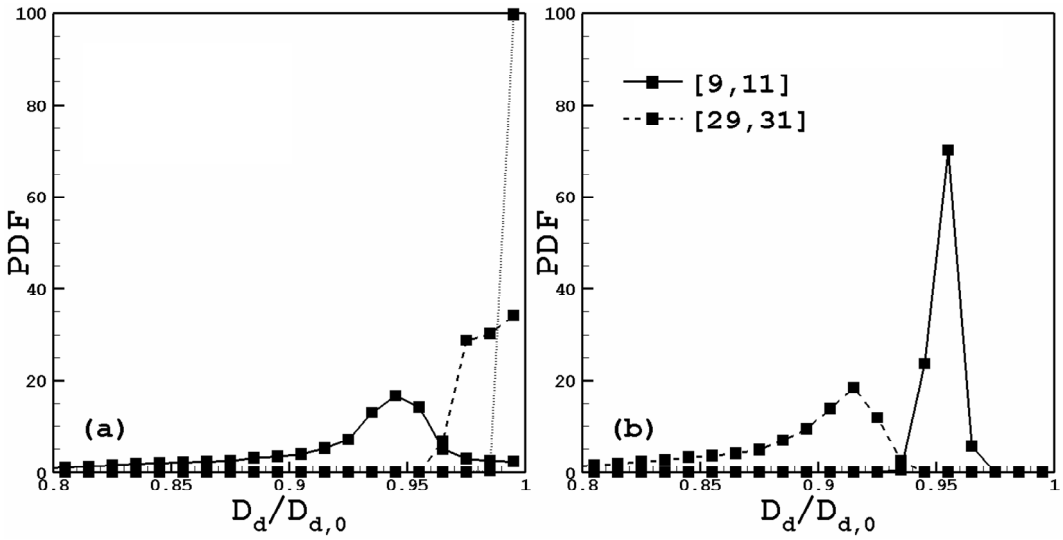

Figure V-18: The PDF profiles of the normalized droplet sizes. In (a): Solid – Case 1a; Dashed – Case 3a; Dotted – Case 3d. In (b): PDF at two heights for Case 1a.

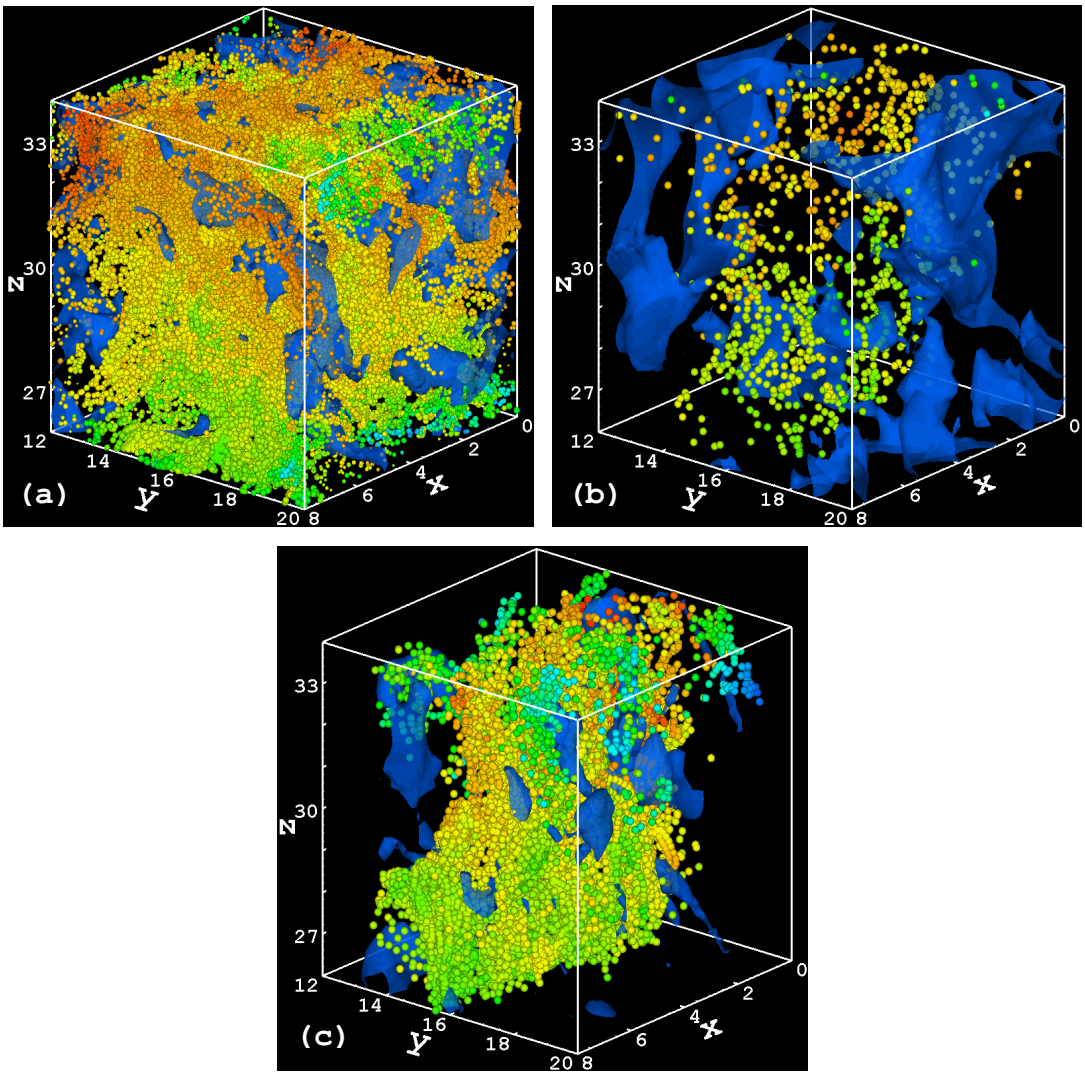

Figure V-19: Snapshots of interaction between evaporating droplets and chemical reaction for different cases: (a) Case 1a; (b) Case 3a; (c) Case 3d. A small cube block in the fully turbulent region, $l_x \times l_y \times l_z = 8 \times 8 \times 8$ in dimension, is magnified for clarity. The blue isosurface represents a typical reaction rate, whose magnitude is 0.004. Droplet temperature is characterized by different colours, blue and red for the lowest and highest temperature, respectively. A same contour legend for droplet temperature, [0.98-1.18], is employed for all the three figures. The size of every single droplet is illustrated by using spheres of different size.

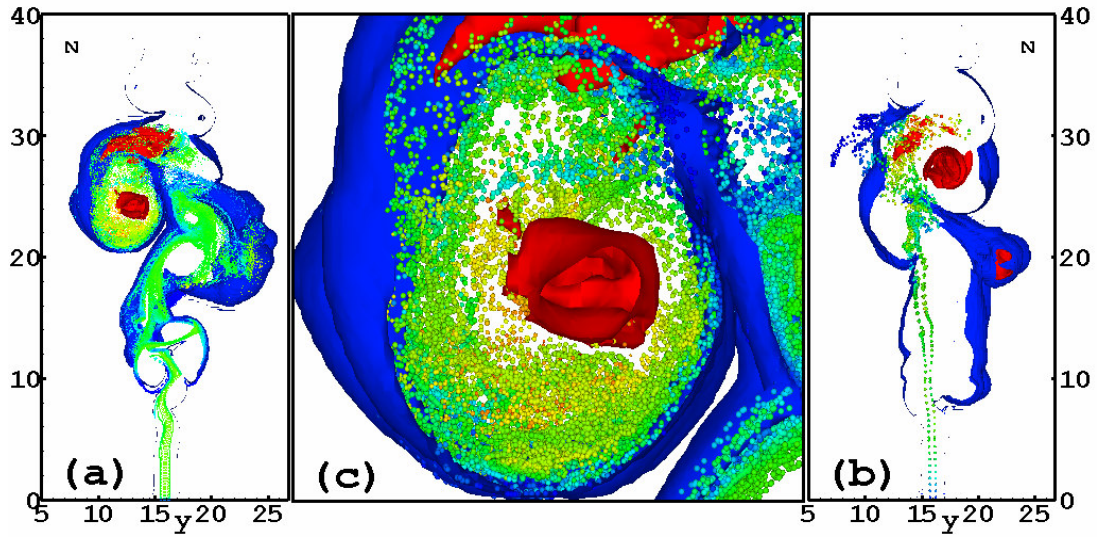

Figure V-20: Instantaneous droplet distributions superimposed with temperature isosurfaces at t=80. T_g=1.005 and 3 are in blue and red colours, corresponding to the ambient and the strong reaction zones, respectively. The colours of the droplets mark the droplet temperature. The droplet size information is also included by using spheres of different diameters. (a) St_0=1; (b) St_0=16; (c) Magnified strong reaction zones in (a).

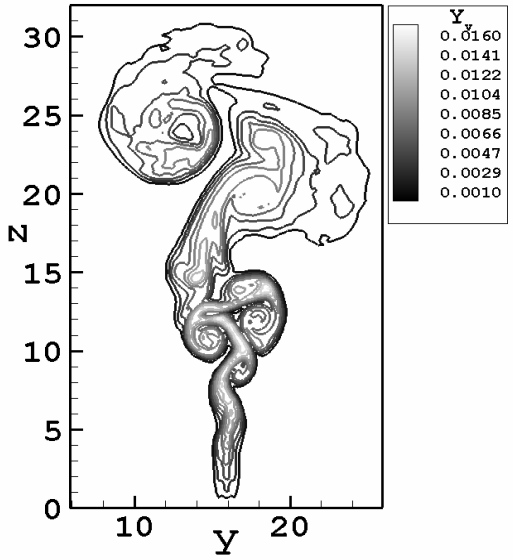

Figure V-21: The averaged Y_v contours for Case 1b at t=80.

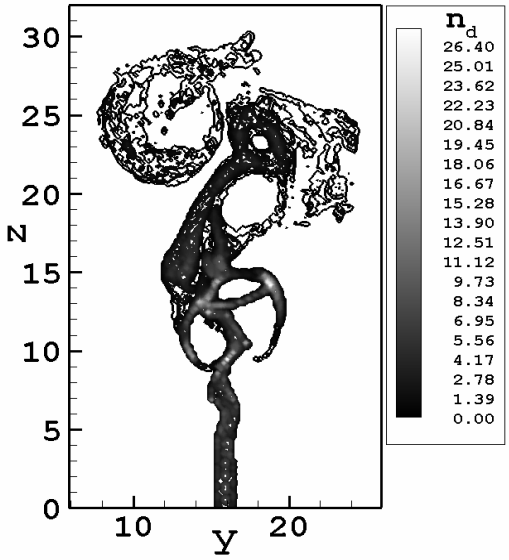

Figure V-22: The contour plot of the averaged droplet number density for Case 1b at t=80.

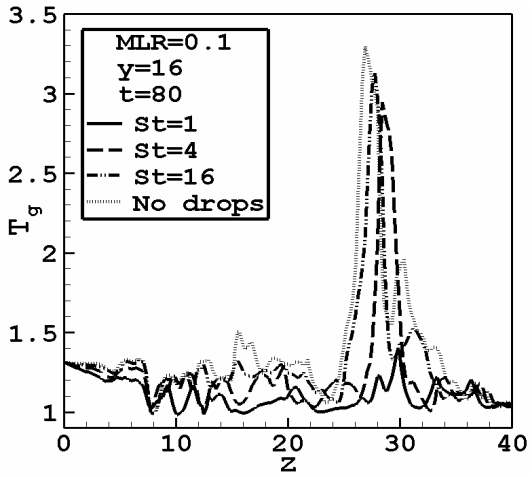

Figure V-23: The averaged centreline profile of T_g.

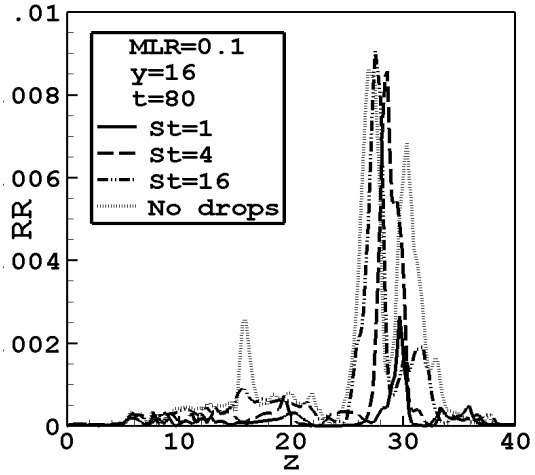

Figure V-24: The averaged centreline profile of *RR*.

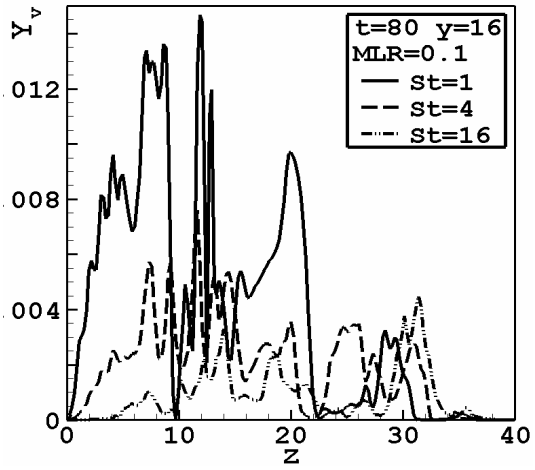

Figure V-25: The averaged centreline profile of Y_v.

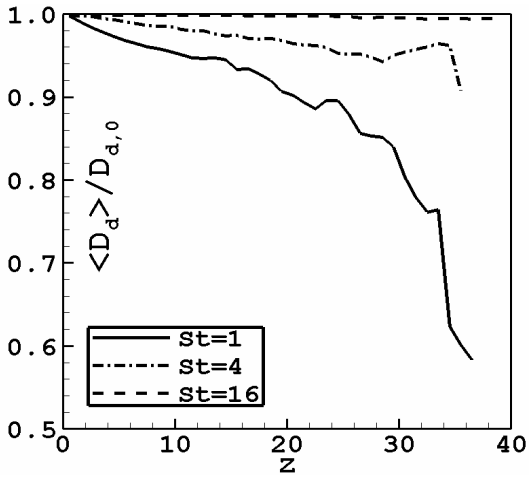

Figure V-26: Variations of the normalized droplet size with the vertical distance for different St_0.

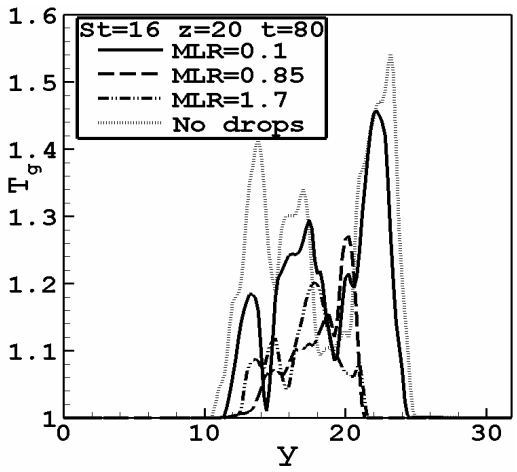

Figure V-27: The averaged lateral profile of T_g at z=20 for the St_0=16 droplets with different MLR_0 when t=80.

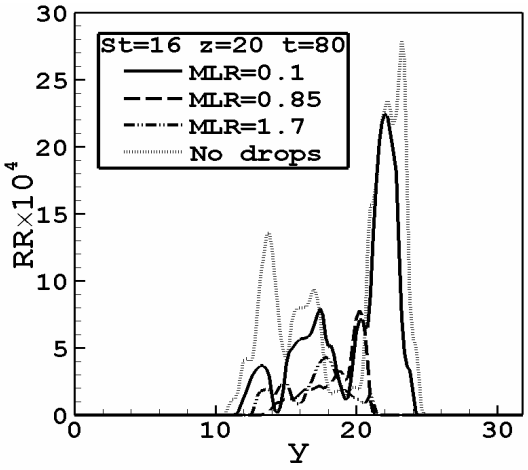

Figure V-28: The averaged lateral profile of RR at z=20 for the St_0=16 droplets with different MLR_0 when t=80.

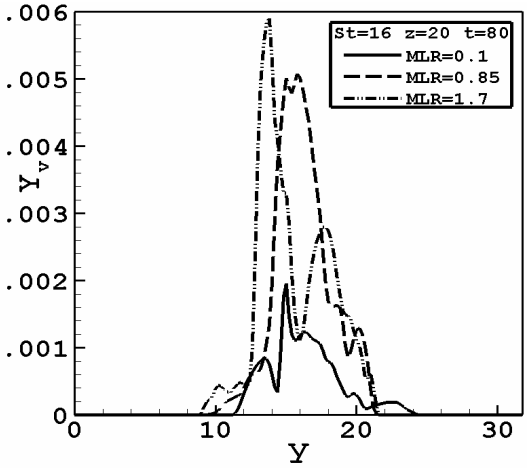

Figure V-29: The averaged lateral profile of Y_v at z=20 for the St_0=16 droplets with different MLR_0 when t=80.

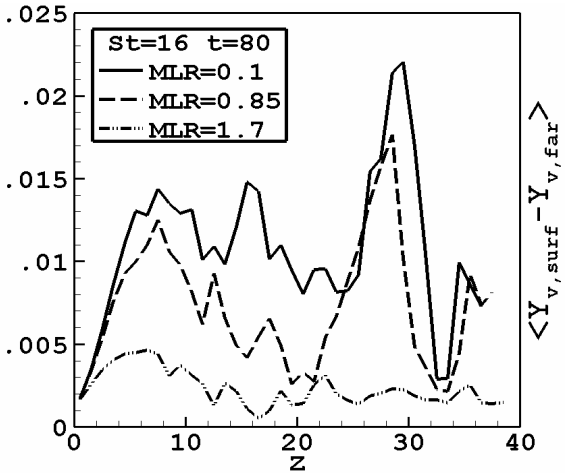

Figure V-30: The vertical distribution of the driving potential of mass transfer for Cases 3b, 3c and 3e.

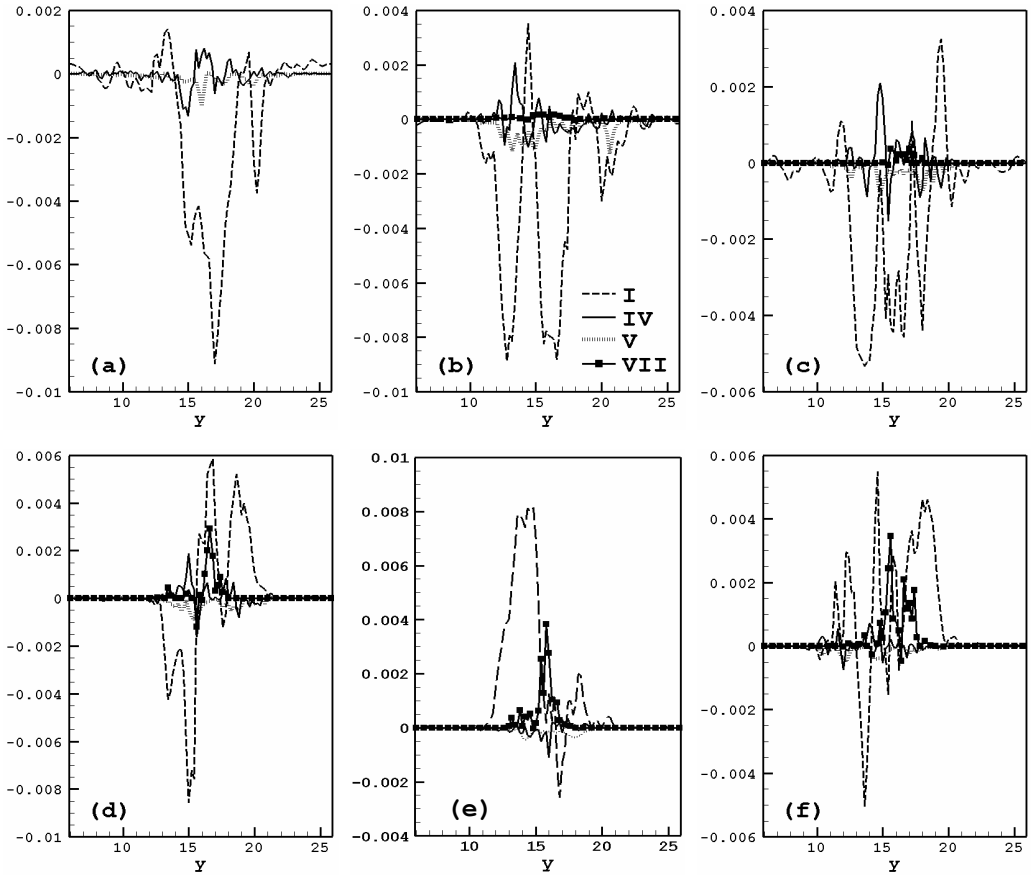

Figure V-31: The x-averaged GSKE budget when t=100 for:

(a) Case 0a at z=30; (b) Case 1a at z=30; (c) Case 3a at z=30;

(d) Case 3d at z=25; (e) Case 3d at z=30; (f) Case 3d at z=35.

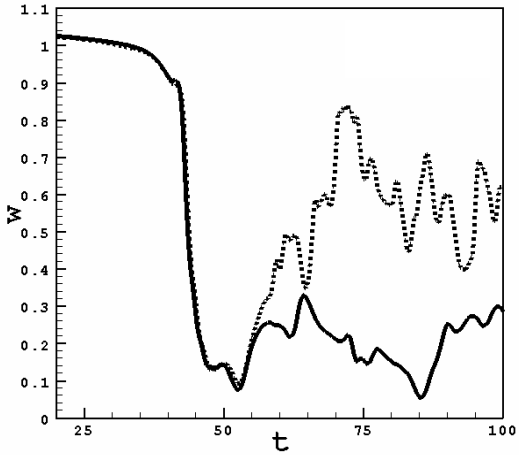

Figure V-32: The time records of streamwise velocity at point (x, y, z) = (4, 15.9, 32) for Cases 0a (solid) and 3d (dashed).

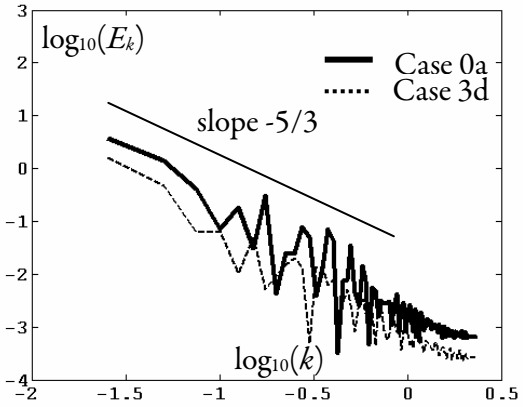

Figure V-33: The energy spectrum of the *x*-averaged centreline streamwise velocity for Cases 0a and 3d.

Chapter VI – LES of a Simplified Small-Scale Fire Suppression System

VI.A Introduction

Life and property loss due to unwanted fires has been a huge concern for centuries. As estimated by Cox (1999), "the total cost of fire to the developed nations of the world is about 1% of GDP each year". Water-based automatic fire sprinklers can effectively reduce residential fire hazards, and have received renewed attention since the ban of Halon gas based fire protection systems due to environmental reasons. However, the overall progress in gaining detailed knowledge of fire suppression systems has been rather slow, due to the complex non-linear, multilateral interactions between fire plumes and water spray.

The suppression mechanisms for water-based fire suppression systems include direct cooling of flame zones, cooling of the fuel surface, dilution of the reactants through the production of water vapour and attenuation of radiation. Strong interactions between flow turbulence and finite-rate chemistry may also lead to flame extinction (Xu & Pope 2000; Xiao *et al.* 2000). The "optimum droplet size" (Grant *et al.* 2000) depends on the dominant suppression mechanism, which varies in different scenarios, and thus differed in various fire scenarios. The water mist systems, in which the initial mean droplet diameter is smaller than ~200 μm, have been receiving renewed attention, since they can make full use of the potential of complete evaporation due to large surface area per unit volume. However, the penetration capacity (Grant *et al.* 2000; Nam 1999) is important, if the droplets have to penetrate deep into the fire or even reach the fire source, *e.g.*, directly cooling the liquid fuel pool. To this end, much bigger droplets, around 1 *mm* or more, are widely deployed for

water spray systems. The evaporation effect due to latent heat of vaporization is thus restricted due to a small total surface area exposed and short residence time as droplets cross over the flame region.

Among the early works, McCaffrey (1984; 1989) provided rare valuable insight on suppression (or dilution) of jet diffusion flames at realistic scales. While most of the work on water-mist technology for fire suppression was still highly empirical in nature until the early 1990's (Tatem *et al.* 1994), substantial detailed experimental investigations have been carried out in recent years (Fuss *et al.* 2002; Richard *et al.* 2003; Fisher *et al.* 2007). Schwille and Lueptow (2006a; 2006b) performed a series of well-established experiments on the interaction between a fire plume and spray in the hot plume region, showing how the plume structure varied due to the presence of droplets and how droplet velocity and trajectories are affected by the fire plume.

A laminar counterflow diffusion flame diluted with water droplets on the oxidizer is a widely used configuration for fundamental theoretical investigation of flame extinction due to intensified strain rate in the presence of water droplets (Lentati & Chelliah 1998a; Dvorjetski & Greenberg 2004). An important parameter is the local Damköhler number (Williams 2000), a measure of competition between a characteristic flow diffusion time scale and a characteristic chemical time scale. If the chemistry cannot catch up with the pace at which reactants diffuse into reaction zones due to promoted strain rate, then the local Damköhler number becomes too small to sustain reaction and local flame quenching takes place. A theoretical analysis of counterflow flame extinction with polydisperse water spray by Dvorjetski and Greenberg (2004) was based on a reduced Damköhler number and large activation-energy asymptotics for the analysis of flame structure (Williams 1985).

Compared to experimental work, numerical studies on multiphase reacting flows, particularly on fire suppression systems, are relatively rare. An early attempt was by Nam (1994; 1996) to investigate the interaction between a fire plume and a sprinkler spray using a RANS (Reynolds-Averaged Navier-Stokes) method. The main focus was to predict the Actual Delivered Densities (ADDs) of sprinklers. However, little information was provided on the physical mechanisms of the highly local and unsteady interactions in the fire plume

region, which is, though physically important, beyond the capacity of RANS-based simulations. The penetration capability of sprinkler spray was scrutinized by Nam in a later paper (1999). It was found that increasing droplet size is a much more effective way for obtaining a higher penetration ratio compared to increasing spray momentum. Prasad *et al.* (1998) studied the suppression of a two-dimensional coflow diffusion flame by fine water mist, using a two-continuum formulation.

It is clear that the selection of simulation approaches and scales of the physical problems in previous numerical studies have been much restricted by the then available computer capacity. However, rapid development in computer hardware and parallel algorithms has taken place in recent years. Accordingly, Large-Eddy Simulation (LES) has appeared as a viable numerical tool to predict fire dynamics and dynamics of fire suppression, taking into consideration both accuracy and cost as compared to other simulation strategies (Luo 2004), and has gained popularity in fire research in recent years (Zhou *et al.* 2002; Xin *et al.* 2002; Prasad & Baum 2005; Xia *et al.* 2008). The Fire Dynamics Simulator (FDS) developed by NIST has shown the capability of LES in various fire scenarios (Xin *et al.* 2002; Prasad & Baum 2005). LES has been employed in Chapter V to investigate the dynamics of turbulent reacting jets diluted with water droplets under various initial droplet sizes and injection densities. It was found that smaller droplets seamlessly followed local flow and concentrated in regions of high strain rates, where intensive mixing and reaction took place. This led to effective reduction of peak reaction rate and peak temperature. Larger droplets, on the other hand, can pass by reaction zones, without much impact on combustion.

The objective of the present chapter is to apply the developed LES methodology to a simplified domestic fire suppression system, in which downward water spray interact with an upward reacting plume. In addition to the reacting jet diluted with water droplets (Chapter V), which is a simplified prototype of humidified gas turbine (Jonsson & Yan 2005), this is the second simplified realistic application studied in this project using the developed dynamic LES methodology. To investigate the mechanisms of multilateral droplet – fire interactions, dynamic subgrid-scale (SGS) models have been employed for six

SGS terms, which significantly reduces the extent of model constant tuning in previous studies. Full details can be found in Chapter II.

VI.B Initial Conditions and Parameters

To simulate a realistic fire suppression scenario using LES is still prohibitively expensive. In this chapter, we limit our aim to improving fundamental understanding of key phenomena in such a scenario in an idealized prototype. Figures VI-1 and VI-2 illustrate the computational domain in which a droplet source is placed at a height of z = 38. The shape and size of the slit sprinkler nozzle is the same as those of the hot fuel jet nozzle. Water droplets are initially discharged from the sprinkler nozzle using a two-dimensional random distribution. The initial discharge angle of a water droplet, ϑ_{d0}, is set by

$$\theta_{d0} = 270^{\circ} + \theta_0 \frac{y_{d0} - L_y/2}{L_{nozzle}} \tag{VI.1}$$

where ϑ_0 is the spray angle of a fire sprinkler; y_{d0} is the initial random lateral coordinate of the droplet; L_{nozzle} is the lateral width of the slit sprinkler nozzle (1 herein). All the water droplets enter the computational domain with a uniform velocity magnitude $|\mathbf{v}_{d0}|$. The initial streamwise and lateral velocity for every droplet are then decided by

$$v_{d0} = |\mathbf{v}_{d0}|\sin\vartheta_{d0},\ w_{d0} = |\mathbf{v}_{d0}|\cos\vartheta_{d0} \tag{VI.2}$$

The initial spanwise velocity of the droplet, w_{d0}, is set to 0. Very similar initial conditions for water sprays were used by Nam (1994; 1996; 1999). A sponge layer (Sandhu & Sandham 1994) starting from z=40 to the outflow boundary z=42.785 is employed to eliminate the reflection of spurious numerical waves at the outflow boundary for all the cases. The modelled fire sprinkler is activated at t=100, when the fire plume, accelerated by the strong buoyancy force (Fr=10), has been established in the computational domain.

Table 1 presents the key simulation and physical parameters. The initial Stokes number St_0, denoting the non-dimensional droplet size, is defined as the ratio of a characteristic droplet responsive time to a characteristic flow time. The initial mass loading ratio MLR_0 is that of the liquid mass flow rate at the sprinkler nozzle to the gas flow rate at the fuel nozzle.

The chosen values for the Damköhler, Da and Zel'dovich number, Ze, the heat release parameter, Q_h, respectively, are shown in Table 1. As radiative heat transfer is not included, these combustion parameters are selected carefully to compensate for radiative heat loss, so that the peak temperature is in the range of a typical small fire. Other initial parameters include: the spray angle ϑ_0, initial Reynolds number Re, latent heat of vaporization of water h_{fg}, the density ratio of the fuel stream to the surrounding S, the computational domain size and grid. The initial droplet diameter for St_0=100 is $D_{d0}^* \approx 720\ \mu m$, and the dimensional initial droplet velocity magnitude for $|\mathbf{v}_{d0}|$=2 is $|\mathbf{v}_{d0}^*| \approx 4\ m/s$, both of which are typical values for standard spray fire sprinklers used for suppression of small-scale fires (Schwille & Lueptow 2006a; 2006b). The droplet number in the domain N_d varies. For example, N_d is close to half a million for Case D at time t = 150 shown in Fig. VI-2.

For Lagrangian-based droplet methods, the "superdrop" model (Kumar *et al.* 1997) is usually adopted to avoid tracking a huge amount of droplets, in which a parcel of physical droplets is represented by one computational droplet. The validity of such method needs further investigation for various scenarios (Persson & Ingason 1996). We found that representing 32 physical droplets by one computational droplet is an optimal choice in LES of a diluted combustion system presented in Chapter V, considering both the computational cost and the numerical accuracy, even in terms of instantaneous flow statistics. For fire suppression systems, generally much bigger droplets are used. To obtain reliable simulation results, physical droplets are traced instead of modelled computational droplets in the present chapter.

VI.C Results and Discussion

VI.C.1 Water Spray vs. Water Mist - Effects of Initial Droplet Size

A general concern of the water-based suppression system is the initial size of the droplets disseminated at the nozzle (Grant *et al.* 2000). Smaller droplets have a better opportunity to make full use of the capacity of complete evaporation. However, in most of the domestic fire suppression systems, the penetration capacity (Nam 1999) of the droplets must be taken

into account, since to efficiently penetrate fire plumes and reach fire base is more crucial to control the fire spread. Figure VI-2 presents the instantaneous distribution of droplets in different initial sizes, *i.e.*, St_0 = 100, 25 and 6.25, in the computational domain. These non-dimensional values correspond to, respectively, 720μm, 360μm and 180μm, the first of which is within the usual range of the volumetric median droplet diameter, d_{v50}, for small fire suppression systems (Schwille & Lueptow 2006a; 2006b), and the third of which is below 200μm and can be considered as mist. As shown in Fig. VI-1, all the St_0 = 100 droplets penetrate the reacting plume region and cover the flame base, forming an ideal pattern in order to control the fire growth and spread. The St_0 = 25 droplets cannot go deep into the plume region. Some of them are retained around the centreline region at $z \approx 20$, referred to as the "interaction boundary" (Schwille & Lueptow 2006a; 2006b), while the others slide down in the off-centre regions where the flow buoyancy is not strong. This statement can be proved by the plots of droplet trajectories shown in Fig. VI-3, where droplets are released at t = 100 and followed until t = 150, for the three cases. The droplet positions are recorded every one time unit, shown as small spheres in the figure. The instantaneous droplet temperature is also given. For the St_0 = 6.25 droplets, none of them can be found below z = 10 in Fig. VI-2c. The initial momentum of the small droplets rapidly vanishes due to the relative strong buoyancy and afterwards these droplets are fully controlled by the rising plume, never reaching the flame base. Notice in Fig. VI-3c the "random walk" of these mist droplets. This situation could be improved by increasing the initial droplet momentum, which is, however, limited by the operating pressure of the sprinklers (Sheppard & Lueptow 2005). Moreover, the fire strength under realistic situations is unpredictable. In a consequence, water spray is generally adopted for suppressing systems due to safety reasons.

The mass fraction of evaporated vapour, Y_v, at t = 150 for the three cases is shown in Fig. VI-4. Although much more vapour is produced for the smaller droplet cases as shown in Fig. VI-4b and VI-4c, the distribution of the vapour in the reacting flow field is far from desired. Especially in Fig. VI-4c, no vapour is found below z = 22, where strong reaction takes place.

On the contrary, in Fig. VI-4a, the reacting plume is better covering by spray droplets and vapour is found throughout the reacting plume, down to the region which is close to the fire base and where intensive reaction is found.

As shown, the St_0 = 25 and 6.25 droplets do not own expected "penetration capacity" (Nam 1999), which is crucial for most fire-fighting cases to rapidly control flame spread and growth. Consequently, the following sections will focus on parametric studies for the spray droplets, St_0 = 100, only.

VI.C.2 Effects of Initial Droplet Momentum

The initial droplet momentum, also referred to as the mass flow rate of the water spray, is an important parameter for practical sprinkler nozzles, which varies either with the initial droplet number or the initial velocity magnitude of every droplet in numerical simulations. In practice, it's determined by the operating pressure of the sprinkler, and generally both the total mass of the ejecting water spray and the initial velocity of the droplets after the break-up process vary with operating pressure (Sheppard & Lueptow 2005). In the present study, these two basic parameters were investigated separately, offering a better explanation of droplet momentum effects on the reacting plume.

Figure VI-5 shows the temperature fields for Cases A, B, E and F at the central plane in the spanwise direction when t = 140. For Cases B, E and F, the total number of ejecting droplets was increased according to MLR_0 while the initial droplet velocity v_{d0} was kept intact. At this time, droplets have fully covered the reacting plume down to the flame base. The cooling effect of the droplets due to the heat exchange between the two phases is obvious. With MLR_0 increased in Fig. VI-5b, VI-5c and VI-5d, the temperature decreases, especially in those active reacting regions. While the plume structure is only moderated in Fig. VI-5b, more evident change can be found in Fig. VI-5c and VI-5d. The rising of the buoyant plume is impeded by droplets, subsequently the lateral extent of the plume becoming wider. Moreover, droplets have induced reversed flow below the sprinkler nozzle. The flow reversal is much stronger in Fig. VI-5d than in Fig. VI-5c. As seen, a big portion of the reversed flow is sandwiched in the blocked rising plume at $z \approx [28, 32]$. Shown in Fig.

VI-6 are the velocity vector fields at the same time and plane for Cases A and F. The entrainment of the air at the lateral boundaries due to the large-scale vortical structures of the buoyant plume is evident in Fig. VI-6a, while in Fig. VI-6b, significant flow reversal is also found at the off-centre regions below $z = 20$, which are covered by droplets and where flow buoyancy is not strong.

The temperature fields at the same plane as in Fig. VI-5 but at a later time $t = 180$ are shown in Fig. VI-7. Compared to Fig. VI-7a, the intensity of the reaction in Fig. VI-7b has been diminished much by droplets. The rising plume is still maintained. In Fig. VI-7c and VI-7d, the high temperature regions are pushed toward the flame base, distributing at the periphery of reversed flow areas. The structure of a rising plume shown in Fig. VI-7a has been completely destroyed.

Figure VI-8 shows the time history of some key parameters recorded at a downstream point on the plume axis of the central spanwise plane $[x, y, z] = [4, 15.8, 24.08]$. For Case B, the magnitude of the streamwise velocity w is smaller than that for Case A, and a small phase delay of w, comparing Case B to Case A, can be found, both due to the drag force exerted on the reacting plume by droplets. For Cases E and F, w becomes negative at $t \approx 165$ and 140, respectively. As shown in Fig. VI-8b, the peak temperature, mean temperature and temperature fluctuations for Case B are all lower than those for Case A. For Case E, after the local flow direction is reversed, the gas temperature T_g is maintained at the level of environmental temperature. This happens to Case F at an earlier time. Stronger temperature fluctuation for Case F than for Case E can be seen after the flow reversal, possibly due to the higher droplet number density for Case F. During the period in which the reversed flow induced by droplets reaches the local region around the monitored point, strong interaction between the two flow streams could introduce better mixing between reactant and oxidizer, leading to transient reaction. This is evident for Case F during $t = [130, 150]$, in which reaction always exists as shown in Fig. VI-8c, while the reaction rate at other times instead appears as a strong pulse. This effect can also be seen in the flow temperature plot, Fig. VI-8b. For Case E, the corresponding period is $t = [155, 165]$. After the flow has been completely reversed, reaction vanishes. Disseminating more droplets does

improve the production of vapour at the initial stage, as shown in Fig. VI-8d. However, such difference is not clearly distinguishable after droplets fully cover the local region. It has been shown in (Xia *et al.* 2006) that better evaporation may not be achieved by continuously increasing the droplet loading, since the driving potential for evaporation decreases with the augmentation of environmental vapour. Similarly, the evaporation process of a cluster of small fuel droplets in statistically stationary homogeneous turbulence was explained by Réveillon and Demoulin (2007). Increasing the local droplet number density through increasing MLR_0 simultaneously accelerates the formation of the vapour field with higher concentration, which impedes the evaporation of succeeding droplets.

The initial droplet momentum can also be varied by changing the initial velocity of droplets, while keeping the number of ejecting droplets identical. Figure VI-9 shows the time records of w and Y_v at the same point as in Fig. VI-8 for Cases A, B, G and H. The streamwise velocities of all the three droplet cases are smaller than that of Case A. Among them no clear distinction is seen. As the initial droplet velocity is increased, the total number of droplets existing in the computational domain is decreased. This may lead to the fact that the difference of the accumulative drag force among the three droplet cases is not significant. No flow reversal takes place. The shorter residence time of droplets in the reacting flow field and less droplets inside the domain make the production of vapour for Case H the lowest.

VI.C.3 Droplet Thermal Effects

For water-based fire suppression systems, one key role played by droplets is to extract thermal energy from the hot plume via cooling and evaporating, and thus reduce the peak reaction rate and temperature of the gas phase. Shown in Fig. VI-10 is an illustration of the interaction between the evaporating droplets and the reacting plume during a short period, showing the captured process in which the gas temperature is considerably decreased through the heat exchange between the phases. As shown by Eq. (II.30), the convective heat transfer due to the temperature difference between the two phases provides the driving potential to raise the droplet temperature and drive evaporation.

The cooling effect induced by droplets can be analyzed in detail via a transport equation on the Filtered Reduced Internal Energy (FRIE) of the two-phase reacting flow, $\overline{\rho_{\mathrm{g}} e_{\mathrm{g}}^{'}}$, defined as

$$\overline{\rho_{\mathrm{g}} e_{\mathrm{g}}^{'}} = \frac{\overline{\rho_{\mathrm{g}} T_{\mathrm{g}}}}{\gamma(\gamma-1)Ma^2} \tag{VI.3}$$

which is also called the filtered *sensible* energy of the carrier phase. The filtered internal energy of the gas phase

$$\overline{\rho_{\mathrm{g}} e_{\mathrm{g}}} = \overline{\rho_{\mathrm{g}}}\left(\frac{\widetilde{T_{\mathrm{g}}}}{\gamma(\gamma-1)Ma^2} + \widetilde{Y_{\mathrm{v}}} h_{\mathrm{v}}^0 \right) = \overline{\rho_{\mathrm{g}} e_{\mathrm{g}}^{'}} + \overline{\rho_{\mathrm{g}} Y_{\mathrm{v}}} h_{\mathrm{v}}^0 \tag{VI.4}$$

under the assumption of identical heat capacities for all the species. In Eq. (VI.4), $\widetilde{Y_{\mathrm{v}}}$ is the Favre-filtered mass fraction of water vapour and h_{v}^0 is the reference enthalpy for vapour. While Eq. (VI.4) provides comprehensive information on the filtered internal energy, the FRIE defined in Eq. (VI.3) is only and directly temperature-dependent and thus of more practical interest.

The transport equation for FRIE can be written as

$$\begin{aligned} \frac{\mathrm{D}}{\mathrm{D}t}\left(\overline{\rho_{\mathrm{g}} e_{\mathrm{g}}^{'}}\right) = & \underbrace{\frac{\partial R_k}{\partial x_k}}_{\mathrm{I}} \underbrace{- \overline{p} \frac{\partial \widetilde{u_{\mathrm{g},k}}}{\partial x_k}}_{\mathrm{II}} \underbrace{+ \overline{Q_{\mathrm{h}} \omega_{\mathrm{T}}}}_{\mathrm{III}} \underbrace{+ \widehat{\sigma_{ik}} \widehat{S_{ik}}}_{\mathrm{IV}} \underbrace{- \widehat{\overline{\rho_{\mathrm{g}}} \tau_{ik}} \widehat{S_{ik}}}_{\mathrm{V}} \\ & \underbrace{- \left(h_{\mathrm{v}}^0 - \frac{\widetilde{u_{\mathrm{g},i}} \widetilde{u_{\mathrm{g},i}}}{2} \right) \overline{S_{\mathrm{ms}}}}_{\mathrm{VI}} \underbrace{- \widetilde{u_{\mathrm{g},i}} \overline{S_{\mathrm{mo},i}}}_{\mathrm{VII}} \underbrace{+ \overline{S_{\mathrm{en}}}}_{\mathrm{VIII}} \end{aligned} \tag{VI.5}$$

where $\widehat{\sigma_{ik}}$ and $\widehat{\overline{\rho_{\mathrm{g}}} \tau_{ik}}$ are the grid scale and subgrid scale stress tensors, the latter of which is determined by the dynamic Smagorinsky model. $\widehat{S_{ik}}$ is the strain rate tensor. The cap symbol " $\widehat{f}$ " designates function f is evaluated with filtered quantities. Equation (VI.5) presents the thermal effect of droplets in the subgrid scale on the grid-scale internal energy.

Terms II-VIII in Eq. (VI.5) designate the pressure dilatation, combustion released heat, grid scale dissipation rate , subgrid scale dissipation rate, and effects due to droplet mass, momentum and energy source terms, respectively. To simplify the analysis and, more importantly, reveal the pertinent factors responsible for the rate of change of FRIE, all the

redistributive terms have been categorized into term I. These terms are not traced, since their integral effect is to transport internal energy from one place to another through various physical mechanisms, such as convection, diffusion, grid and subgrid scale transportation, *etc.*, instead of producing or dissipating internal energy as source or sink terms (Luo 1999). To further distinguish among the thermal, dynamic and evaporating contributions from droplets, substituting Eqs. (II.51)-(II.53) into Eq. (VI.5) and rearranging the droplet-related terms yield

$$\frac{\mathrm{D}}{\mathrm{D}t}\left(\overline{\rho_{\mathrm{g}} e_{\mathrm{g}}^{'}}\right)=\underbrace{\frac{\partial R_k}{\partial x_k}}_{\mathrm{I}}\underbrace{-\overline{p}\frac{\partial \widetilde{u_{\mathrm{g},k}}}{\partial x_k}}_{\mathrm{II}}\underbrace{+\underline{Q}_{\mathrm{h}}\overline{\omega_{\mathrm{T}}}}_{\mathrm{III}}\underbrace{+\widehat{\sigma_{ik}}\widehat{S_{ik}}}_{\mathrm{IV}}\underbrace{-\overline{\rho_{\mathrm{g}}}\tau_{ik}\widehat{S_{ik}}}_{\mathrm{V}}\underbrace{+S_{\mathrm{th}}}_{\mathrm{VI}}\underbrace{+S_{\mathrm{me}}}_{\mathrm{VII}}\underbrace{+S_{\mathrm{evt}}}_{\mathrm{VIII}}\underbrace{+S_{\mathrm{evm}}}_{\mathrm{IX}} \tag{VI.6}$$

where

$$S_{\mathrm{th}}=-\frac{1}{V}\sum_k\left[\frac{1}{3}\frac{Nu_k}{(\gamma-1)Ma^2 Pr}\frac{m_{\mathrm{d},k}}{St_k}\left(T_{\mathrm{g},k}-T_{\mathrm{d},k}\right)\right] \tag{VI.7}$$

$$S_{\mathrm{me}}=-\frac{1}{V}\sum_k\left[-F_{\mathrm{drag},k,i}\left(\widetilde{u_{\mathrm{g},i}}-v_{\mathrm{d},k,i}\right)\right] \tag{VI.8}$$

$$S_{\mathrm{evt}}=-\frac{1}{V}\sum_k\left[\frac{1}{(\gamma-1)Ma^2}\dot{m}_{\mathrm{d},k}T_{\mathrm{d},k}\right] \tag{VI.9}$$

$$S_{\mathrm{evm}}=-\frac{1}{V}\sum_k\left[\frac{1}{2}\dot{m}_{\mathrm{d},k}\left(\widetilde{u_{\mathrm{g},i}}-v_{\mathrm{d},k,i}\right)^2\right] \tag{VI.10}$$

As indicated, S_{th} is the thermal cooling effect due to the convective heat transfer between the two phases; S_{me} is the mechanical work done by the drag force; S_{evt} is the droplet internal energy which is transferred into the gas after evaporation; S_{evm} is a contribution arising from the interaction of kinetic energy between the two phases. The latent heat of vaporization, h_{fg}, plays its role via S_{th}, as shown in Eq. (II.30), and impact the evaporation rate $\dot{m}_{\mathrm{d}}$ indirectly, but it does not appear explicitly in all the droplet source/sink terms, which are expressed by Eqs. (VI.7)-(VI.10). This is a direct consequence of the fact that the budget analysis is upon the temperature-dependent internal energy $\overline{\rho_{\mathrm{g}} e_{\mathrm{g}}^{'}}$, but not the total internal energy $\overline{\rho_{\mathrm{g}} e_{\mathrm{g}}}$.

Statistics on the budget terms in Eq. (VI.6) have been obtained for Cases A, B, G and H. No such statistics have been done for Cases E and F, since they are highly unsteady flow phenomena, as indicated by the temporal records of the streamwise velocity at a downstream point in Fig. VI-8a. To this end, the time averaging procedure is not proper for these specific cases. t = [140, 200] has been chosen as the recording period for the averaging purpose, which contains approximately one "flow-through time" period and two "droplet-through time" periods. At t = 140, droplets have covered the whole plume region from the sprinkler nozzle down to the fire base at the inflow boundary. Further recording, although preferable, has not been performed due to the huge computational cost demanded by the two-phase flow simulations. However, as will be shown, clear trend of the droplet thermal effect on the reacting plume has been unveiled with the current data. The spatial ensemble averaging over the spanwise direction is performed finally.

Shown in Fig. VI-11 are the centreline budgets of the combustion released heat term III and all the droplet terms, VI, VII, VIII and IX, in Eq. (VI.6) for Cases A, B, G and H. A comprehensive discussion on the effects of other terms in Eq. (VI.6), *i.e.*, II, IV and V, is deferred to the next section "Droplet Dynamic Effects", since the same terms but with opposite signs appear in the transport equation for the filtered kinetic energy as well. As shown, the magnitudes of VI and VII are similar and dominant among all the droplet-related terms, followed by VIII. The contribution of term IX is the smallest. Except for the heat exchange term VI, all the other three are source terms for FRIE. This means term VI is the only driving potential to reduce gas temperature among all the droplet terms in Eq. (VI.6), while the others act as undesirable "side effects". In Fig. VI-11a, the magnitude of the profile for Case B is bigger than those for Cases G and H, since more droplets exists in the computational domain and longer residence time offers a better opportunity for the two phases to exchange heat. It is noteworthy that the mechanical work term VII serves as a considerable source to FRIE. This can be explained by the simple fact that "Friction produces heat". This effect due to the inter-phase drag has been seldom discussed, as it is difficult to be investigated with a convection-free configuration such as counterflow diffusion flame laden with water droplets, which is widely adopted in previous studies on

this topic (Lentati & Chelliah 1998a, 1998b; Dvorjetski & Greenberg 2004; Chelliah 2007). Moreover, the inter-phase drag is insignificant for fine water mist droplets (Lentati & Chelliah 1998a, 1998b; Dvorjetski & Greenberg 2004; Chelliah 2007) compared with water spray droplets investigated in this study. It was found in the present study that S_{me} can be an important contribution to the gas phase internal energy, and thus the temperature. In the region below and close to the droplet discharging position, the magnitude of term VII for Case H is the biggest, but the difference among the three cases becomes not significant in upstream regions. Similar to VII, IX only shows distinguishable difference close to the discharging position. The magnitude of term VIII for Case B is much bigger than that of the other two cases. This can be explained as follows. The evaporation rate of droplets for Case B is prone to be promoted by the stronger driving potential for heat exchange, as shown in Fig. VI-11a. Figure VI-8b has illuminated that more vapour is produced at a downstream monitored point for Case B in comparison to Cases G and H. Meanwhile, the longer interaction time between the two phases for Case B benefits the augmentation of droplet temperature.

Figure VI-11a shows the averaged centreline budget of the combustion released heat, term III in Eq. (VI.6), for Cases A, B, G and H. Since Q_h is set to be a constant, this plot also directly reveals the averaged reaction rate. The solid line presents a typical reaction rate plot of fire plumes widely observed in experiments, in which intense reaction takes place in the vicinity of flame base and the flow in downstream regions is characterized by thermal plume. As shown, the peak reaction rate has been considerably weakened for all the droplet cases. In Figs. VI-11b and VI-11c, the magnitudes of both the sink term S_{th} and the source term S_{me} for Case B predominate over those for Cases G and H, and temperature reduction seems more guaranteed for Case B. Consequently, intuition may suggest that better control over the reaction rate should be found in Case B, which is, however, not the fact as shown in Fig. VI-11a. Moreover, in downstream regions where $z \approx [20, 30]$, higher reaction rate can be found for droplet cases. Especially for Case H, another peak appears at $z \approx 21$, whose magnitude approaches that of the primary peak at $z \approx 7$. These phenomena cannot be explained directly from Figs. VI-11b ~ VI-11e, which *only* presents the thermal effect of

droplets on the internal energy of the reacting plume. As shown by Eq. (II.25), reaction rate depends upon both the mass fractions of reactants and gas temperature, which are nonlinearly correlated in finite-rate reactions as in this study, where considerable quench of flames is induced by water droplets. The mixing of reactants in large scales and the micro-mixing in small scales are the other crucial factors affecting reaction. The gas temperature rise due to the initial enhancement of turbulent mixing after the droplet injection has been found in a previous numerical study of water spray suppression for a compartment pool fire (Yoon *et al.* 2007). Réveillon and Vervisch (2000) found the scalar dissipation rate is enhanced with the presence of fuel droplets in homogeneous decaying turbulence. Similarly, as shown by Fig. IV-6 in Chapter IV, the conditional scalar dissipation rate in a reacting shear layer is also found enhanced due to the non-reactive droplets. Quantities such as mixture fraction and scalar dissipation rate deserve further investigation, although more consideration is necessary, since mixture fraction defined in the usual way is no longer a passive scalar in the presence of evaporated vapour (Réveillon & Vervisch 2000). Moreover, the (filtered) scalar dissipation rate cannot be directly obtained with the LES data. Models such as those proposed by Domingo *et al.* (2002) may be used to evaluate the subgrid scalar dissipation rate, but validation must be carried out against DNS or experimental data. The full physics involved seems only possible to be investigated with DNS in a simpler configuration. Despite the complex thermodynamic interactions, the overall droplet effects in reducing the reaction rate and gas temperature are clearly demonstrated in Figs. VI-11a, VI-8a and VI-8b.

VI.C.4. Droplet Dynamic Effects

The droplet dynamic effect on the reacting plume is scrutinized via the following transport equation,

$$\frac{\mathrm{D}}{\mathrm{D}t}\left(\overline{\rho_\mathrm{g}}\widehat{k_\mathrm{g}}\right)=\underbrace{-\frac{\partial\left(\overline{p}\widetilde{u_{\mathrm{g},k}}\right)}{\partial x_k}}_{\mathrm{I}}+\underbrace{\overline{p}\frac{\partial\widetilde{u_{\mathrm{g},k}}}{\partial x_k}}_{\mathrm{II}}+\underbrace{\frac{\partial\left(\widehat{\sigma_{ik}}\widetilde{u_{\mathrm{g},i}}\right)}{\partial x_k}}_{\mathrm{III}}\underbrace{-\widehat{\sigma_{ik}}\widehat{S_{ik}}}_{\mathrm{IV}}\underbrace{-\frac{\partial\left(\overline{\rho_\mathrm{g}}\tau_{ik}\widetilde{u_{\mathrm{g},i}}\right)}{\partial x_k}}_{\mathrm{V}}\underbrace{+\overline{\rho_\mathrm{g}}\tau_{ik}\widehat{S_{ik}}}_{\mathrm{VI}}$$
$$\underbrace{-\frac{\left(\rho_\mathrm{a}-\overline{\rho_\mathrm{g}}\right)\widetilde{u_{\mathrm{g},i}}g_i}{\mathrm{Fr}}}_{\mathrm{VII}}\underbrace{-\frac{\widetilde{u_{\mathrm{g},i}}\widetilde{u_{\mathrm{g},i}}}{2}\overline{S_\mathrm{ms}}}_{\mathrm{VIII}}\underbrace{+\widetilde{u_{\mathrm{g},i}}\overline{S_{\mathrm{mo},i}}}_{\mathrm{IX}} \tag{VI.11}$$

where $\overline{\rho_\mathrm{g}}\widehat{k_\mathrm{g}}$ is the Grid-Scale Kinetic Energy (GSKE) of the gas phase, and $\widehat{k_\mathrm{g}}=\widetilde{u_{\mathrm{g},i}}\widetilde{u_{\mathrm{g},i}}/2$. Equation (VI.11) presents the dynamic effect of droplets in the subgrid scale on the grid-scale kinetic energy. Terms I-IX account for the effects of pressure transport, pressure dilatation, viscous or GS diffusion, viscous or GS dissipation, redistribution due to SGS stress or SGS diffusion, SGS dissipation, buoyancy, and effects due to the droplet mass and momentum source terms, respectively. A similar equation without the droplets source terms have been used by da Silva and Métais (2002) to investigate the kinetic energy exchange between grid and subgrid scales in a turbulent plane jet with DNS data. In the present study, the SGS stress tensor τ_{ij} in terms V and VII is modelled by the dynamic Smagorinsky model. The quality of LES can thus be appraised by comparing the magnitudes of the GS dissipation IV and SGS dissipation VI (da Silva & Métais 2002). Terms II, IV, VI, VIII and IX in Eq. (VI.11) appear in Eq. (VI.5) as well, but with opposite signs, since dissipation of kinetic energy results in production of thermal energy, or *vice versa*. It is also interesting to note that although the buoyancy term VII plays an important role for the development of kinetic energy, which will be shown below, it does not affect the internal energy at all.

Similar to the previous section, rearrangement of the droplet terms VIII and IX has been performed to obtain physically meaningful source/sink terms due to droplets. This is different from the practice in Chapter V, where the effects of droplet source terms on the GSKE were analyzed. The new equation reads

$$\frac{\mathrm{D}}{\mathrm{D}t}\left(\overline{\rho_{\mathrm{g}}}\widehat{k_{\mathrm{g}}}\right)=\underbrace{-\frac{\partial\left(\overline{p}\widetilde{u_{\mathrm{g},k}}\right)}{\partial x_k}}_{\mathrm{I}}+\underbrace{\overline{p}\frac{\partial\widetilde{u_{\mathrm{g},k}}}{\partial x_k}}_{\mathrm{II}}+\underbrace{\frac{\partial\left(\widehat{\sigma_{ik}}\widetilde{u_{\mathrm{g},i}}\right)}{\partial x_k}}_{\mathrm{III}}\underbrace{-\widehat{\sigma_{ik}}\widehat{S_{ik}}}_{\mathrm{IV}}\underbrace{-\frac{\partial\left(\overline{\rho_{\mathrm{g}}}\tau_{ik}\widetilde{u_{\mathrm{g},i}}\right)}{\partial x_k}}_{\mathrm{V}}+\underbrace{\overline{\rho_{\mathrm{g}}}\tau_{ik}\widehat{S_{ik}}}_{\mathrm{VI}}$$
$$\underbrace{-\frac{\left(\rho_{\mathrm{a}}-\overline{\rho_{\mathrm{g}}}\right)\widetilde{u_{\mathrm{g},i}}g_i}{\mathrm{Fr}}}_{\mathrm{VII}}+\underbrace{S_{\mathrm{me}}}_{\mathrm{VIII}}+\underbrace{S_{\mathrm{ev}}}_{\mathrm{IX}} \tag{VI.12}$$

where

$$S_{\mathrm{me}}=-\frac{1}{V}\sum_k F_{\mathrm{drag},k,i}\widetilde{u_{\mathrm{g},i}} \tag{VI.13}$$

$$S_{\mathrm{ev}}=-\frac{1}{V}\sum_k\left\{\dot{m}_{\mathrm{d},k}\left(\widetilde{u_{\mathrm{g},i}}v_{\mathrm{d},k,i}-\widetilde{u_{\mathrm{g},i}}\widetilde{u_{\mathrm{g},i}}/2\right)\right\} \tag{VI.14}$$

S_{me} is the mechanical work due to the drag force, and S_{ev} the contribution from the evaporation.

Figure VI-12 presents the averaged plume centreline budgets of respective terms in Eq. (VI.12) for Cases A, B, G and H. As shown, the pressure terms are dominant for all the cases. Also, their profile shapes are fairly similar to that of the combustion released heat term in Eq. (VI.6), which designates a close correlation between these terms. Dilatation is a measure of volume variation (Luo 1999). As reaction induces volume expansion, the pressure-dilatation term rapidly grows and acts as a strong source term for the GSKE. It's also interesting to find that the sum of these two terms related to pressure, *i.e.*, $\widetilde{u_{\mathrm{g},k}}\partial\overline{p}/\partial x_k$, is tiny, indicating that statistically the spatial variation of pressure is very small. This is true for a reacting plume with or without suppressing droplets in open space and demonstrates the success of non-reflecting boundary conditions applied.

The second contribution comes from the buoyancy term VII and the mechanical work done by the droplets, VIII. For Case A, the buoyancy term is a considerable source for GSKE. As Eq. (II.13) would reveal, the augmentation of the streamwise momentum by the buoyancy force is the fundamental explanation. Its peak is found at a higher location, $z \approx 13$, than that of the reaction rate as shown in Fig. VI-9e. This is the region where the gas temperature goes highest. The buoyancy effect has been weakened a lot for all the droplet cases, among which the droplets for Case H affect the work done by the buoyancy most

significantly. At the droplet discharging position, small level of flow reversal can be found, which induces a strong peak of term VIII for Case H. In this region, the directions of the drag force and the streamwise velocity of the gas phase are opposite. Notice $\mathbf{F}_{drag}$ is defined as the drag force exerted by the flow on droplets.

The droplet evaporation effect S_{ev} stands in the third position for the contribution to the GSKE, together with the SGS diffusion V and SGS dissipation VI. The profiles of S_{ev} exhibit a similar trend to those of S_{me}, with the magnitudes ten times lower. The low level of evaporation for these suppression cases is the direct cause which leads to the magnitudes of S_{ev} is not significant. The GS diffusion III and dissipation IV are the smallest contribution, which are one order of magnitude smaller than the SGS diffusion VII and dissipation VIII, respectively. This is also a direct proof that the grid spacing has been chosen properly, since it is a prerequisite for well-resolved LES that the SGS dissipation rate must predominate over the GS dissipation rate. The GS diffusion is much weaker than the SGS diffusion, which was also found in the *a-priori* DNS analysis on a turbulent plane jet (da Silva & Métais 2002). This applies to both the reacting plume and the two-phase cases. Droplets decrease both the GS and SGS diffusion effect, as shown in Figs. VI-12c and VI-12e. For the reacting plume, the GS diffusion effect mostly act as a sink to the GSKE, while for all the droplet cases, it fluctuates weakly around zero, except in the vicinity to the flame base. The difference among the droplet cases is hardly discernible. The fluctuation of the SGS diffusion for the droplet cases is smaller than that of the reacting plume. While the modification to the GS dissipation IV due to droplets is not obvious, the SGS dissipation effect VI is evidently stronger for the droplet cases. This can be justified since the interaction between evaporating droplets and the reacting flow is truly subgrid-scale phenomena in the present study. As droplets penetrate the reacting plume, the large-scale flow structures undergo considerable modification and more small-scale structures appear, accounting for the enhancement of the SGS dissipation VI. This is especially evident in the regions close to the sprinkler nozzle, where the highest droplet number density is found, and regions close to the flame base, where the initially developed vortical structures are

destroyed by droplets. As discussed above, the higher reaction rate found in the downstream region must also be induced by the enhanced turbulent mixing.

VI.D Chapter Summary

A fundamental study of dynamic interactions between a buoyant reacting plume and evaporating droplets has been carried out using LES. An idealised prototype configuration is set up to numerically mimic a sprinkler system placed right above the fire source, dispensing evaporating droplets of various properties. The configuration is different from most used in previous numerical studies and has a prototype value. An extensive parametric study has been conducted by varying the initial Stokes number (St_0) or non-dimensional droplet size, mass loading ratio (MLR_0) and droplet velocity (v_{d0}), independently.

Droplets of three initial sizes (720μm, 360μm and 180μm) have distinctively different dynamic interactions with the reacting plume. The smallest droplets are held up completely by the rising buoyant reacting plume and never reach below a certain height. The medium droplets are partially blocked by the upward plume but some droplets reach the plume base level in the peripheral regions. The largest droplets can penetrate the whole plume and have maximum suppression effects on the reaction.

Detailed field analysis has been conducted to examine the complex nonlinear interactions among droplet dynamics, evaporation, turbulence and chemical reaction under different levels of MLR_0 (i.e., 0, 3, 6 and 9) for the water spray droplets St_0=100 or $D^*_{d,0}$=720μm. Increasing MLR_0 progressively increases the droplet effects, and in the case of the largest drops used, the reaction is completely suppressed and the plume structure destroyed. Increasing MLR_0 is more effective in causing flow reversal in the central plume region than increasing droplet velocity v_{d0} for the same initial droplet momentum. However, when St_0 and MLR_0 are fixed, increasing v_{d0} has mixed effects. On the one hand, larger v_{d0} leads to higher droplet penetration capacity and lower plume upward velocity. On the other hand, it results in less droplet residence time in the computational domain and consequently shorter time for thermal cooling of the reacting plume.

The budget equation for a non-dimensional gas temperature called the Filtered Reduced Internal Energy (FRIE) has been analyzed, with a focus on the droplet-related terms. One remarkable finding is that the only "cooling" effect on gas temperature comes from the convective heat transfer between the phases while there are three mechanisms (mechanical work done by droplet drag force, internal energy transfer into the gas phase due to evaporation and kinetic energy interactions between the phases) contributing to "warming" effects. On a purely order of magnitude analysis, all four droplet-related terms are very small compared with the heat release term. However, their importance in combustion suppression is amply demonstrated in the resulting significant reduction in reaction rate and gas temperature especially the peak values. The droplet dynamic effect on the fire plume is analyzed through the transport equation of the Grid-Scale Kinetic Energy (GSKE). Compared to the evaporation term, the drag contribution is more important and stands in the second position together with the buoyancy. The subgrid-scale dissipation rate is enhanced by droplets.

Table VI-1: Simulation parameters and cases. Re=4000, S=0.76, Fr=10, Da=80, Ze=8.5, Q_h=250, h_{fg}=250, ϑ_0=50°. The computational domain size $L_x \times L_y \times L_z$ = 8×31.8×42.785, and the grid $n_x \times n_y \times n_z$ = 41×160×200.

Re	S	Fr	Da	Ze	Q_h	h_{fg}	ϑ_0
4000	0.76	10	80	8.5	250	250	50°

Cases	St_0	MLR_0	$\lvert v_{d0} \rvert$
A	-	0	-
B	100	3	2
C	25	3	2
D	6.25	3	2
E	100	6	2
F	100	9	2
G	100	3	3
H	100	3	4

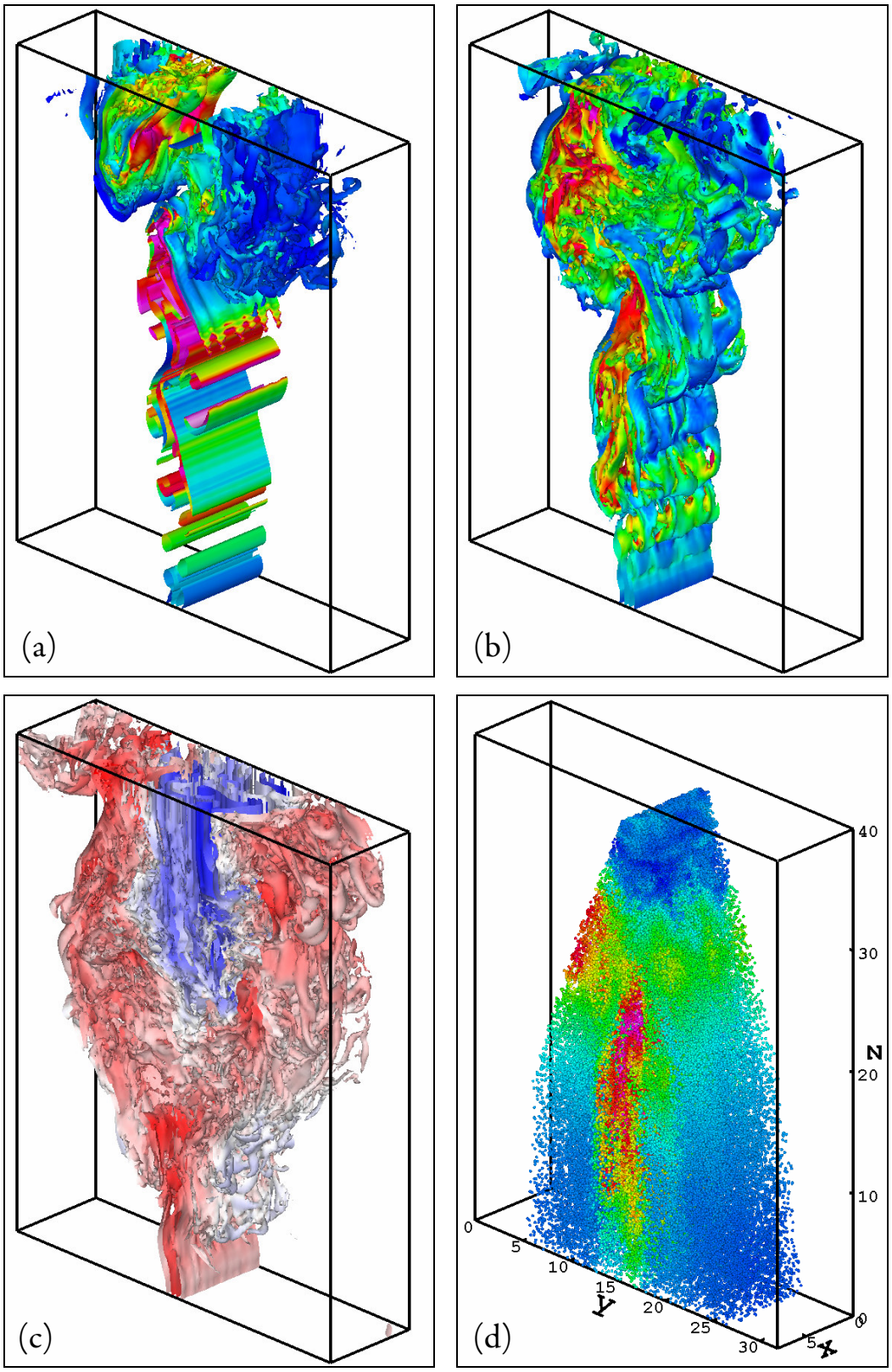

Figure VI-1: Illustration of some suppression cases investigated. The iso-surface of the vorticity magnitude $|\omega|=1$ at t =180 are shown in Figs. VI-1a, VI-1b and VI-1c for the reacting plume and the plume undergoing mild and moderate suppression, respectively.

Figure VI-1d illustrates the instantaneous distribution of droplets for the case of Fig. VI-1b. The colour information gives the gas temperature in Fig. VI-1a, VI-1b, the streamwise velocity in Fig. VI-1c and the evaporation rate of every single droplet in Fig. VI-1d, respectively.

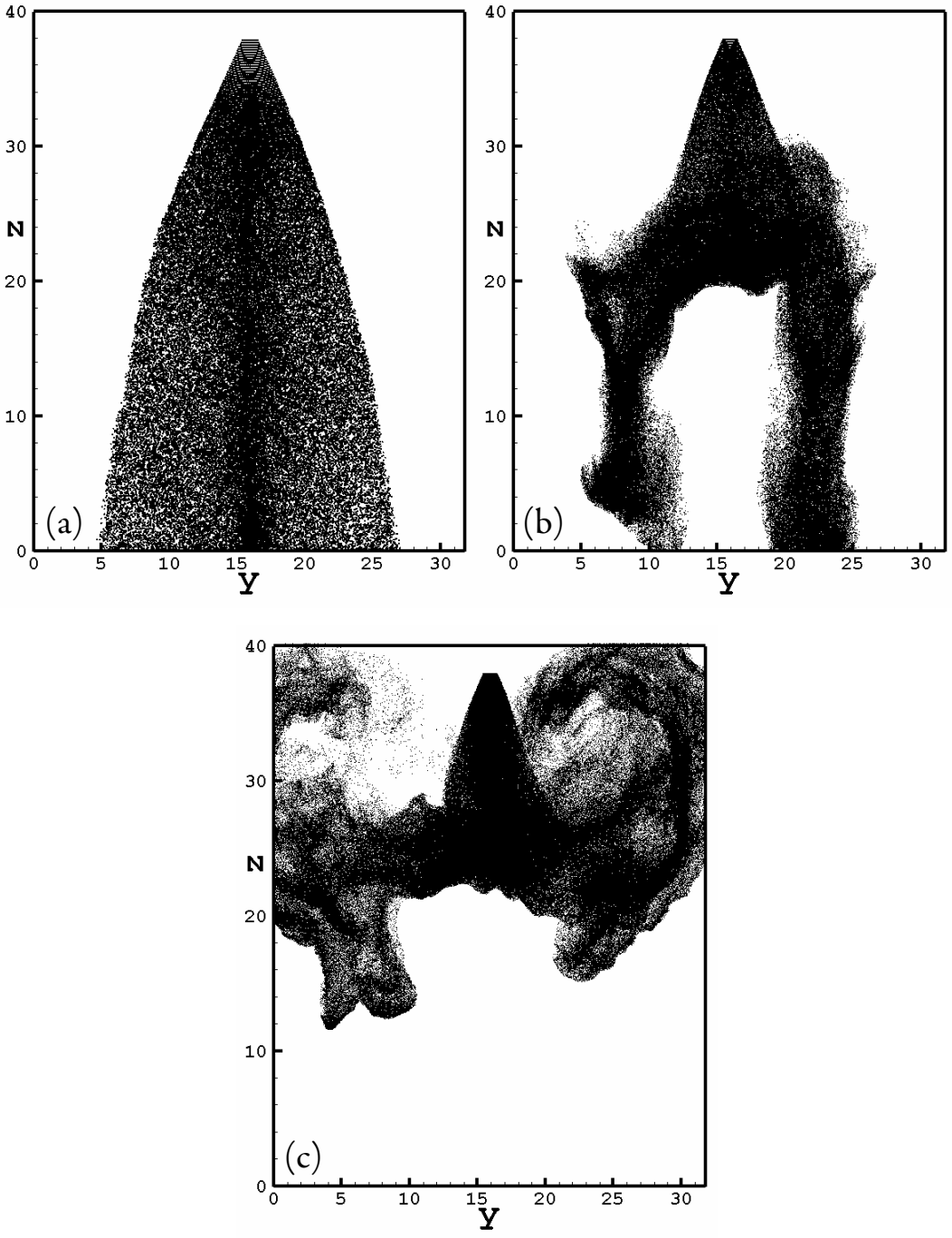

Figure VI-2: The droplet distribution at t = 150 for:

(a) Case B, (b) Case C and (c) Case D.

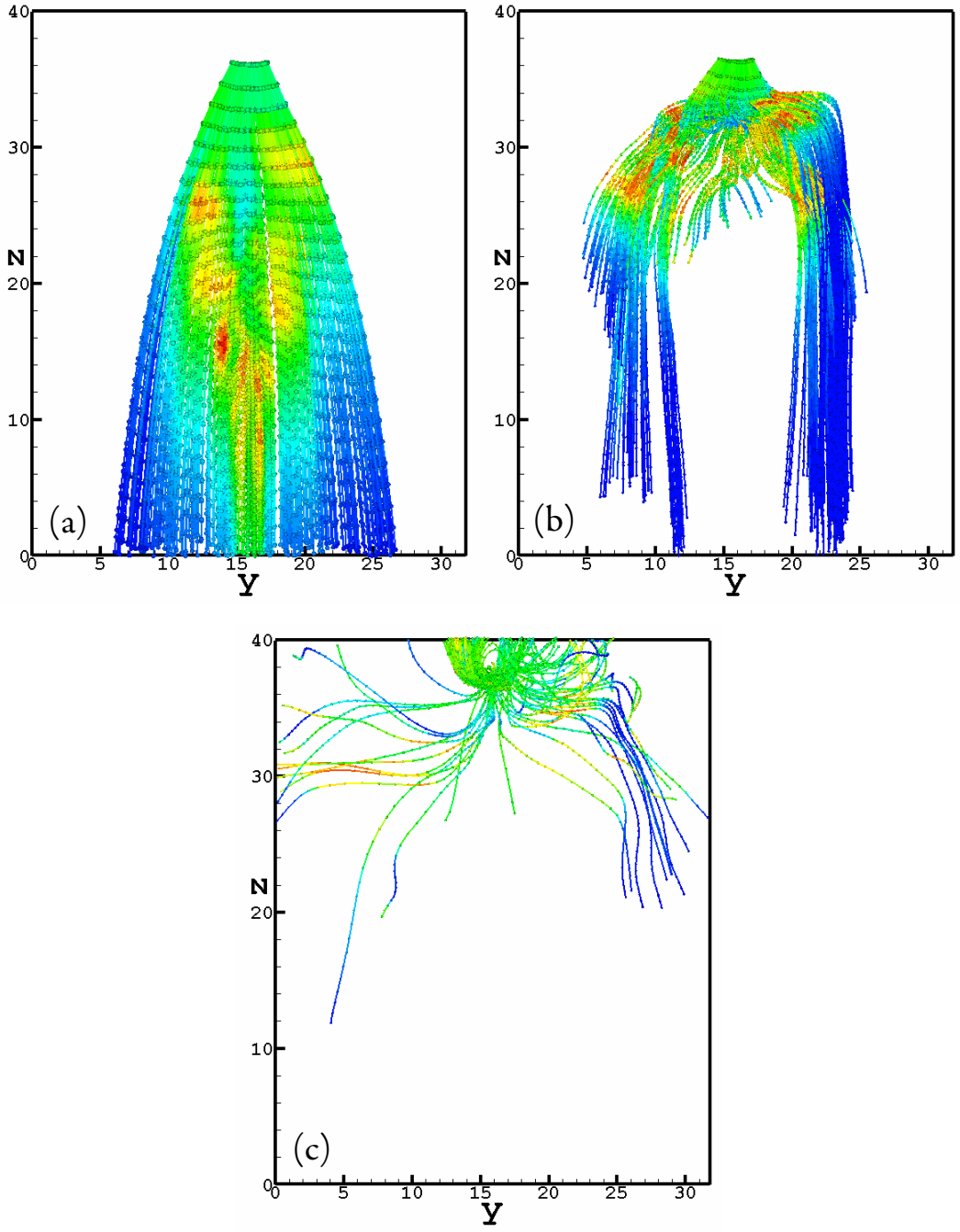

Figure VI-3: The droplet trajectories during the period t = [100, 150] for: (a) Case B, (b) Case C and (c) Case D. The droplet position was recorded every one time unit, shown as points in the figure. The colour information illustrates the instantaneous droplet temperature.

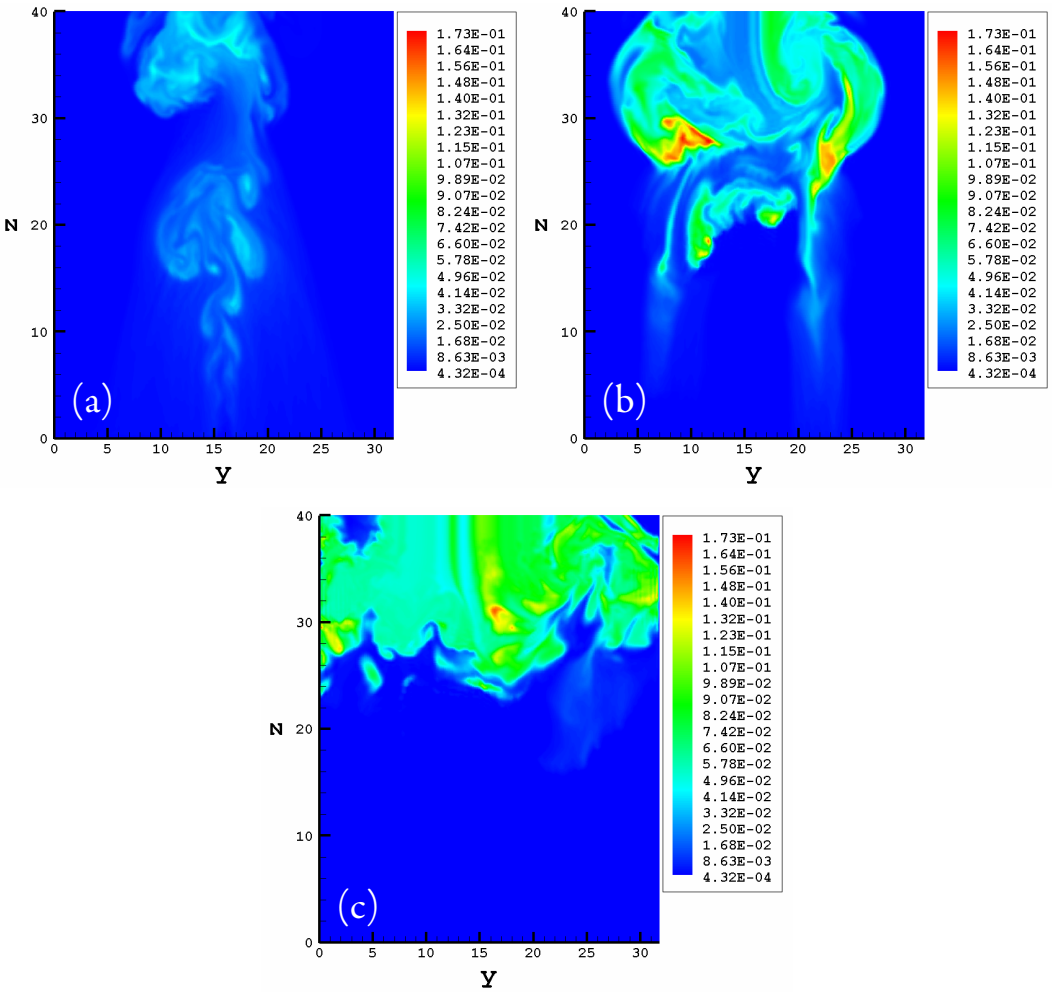

Figure VI-4: The mass fraction of evaporated vapour Y_v at the central plane in the spanwise direction when t = 150 for: (a) Case B, (b) Case C and (c) Case D.

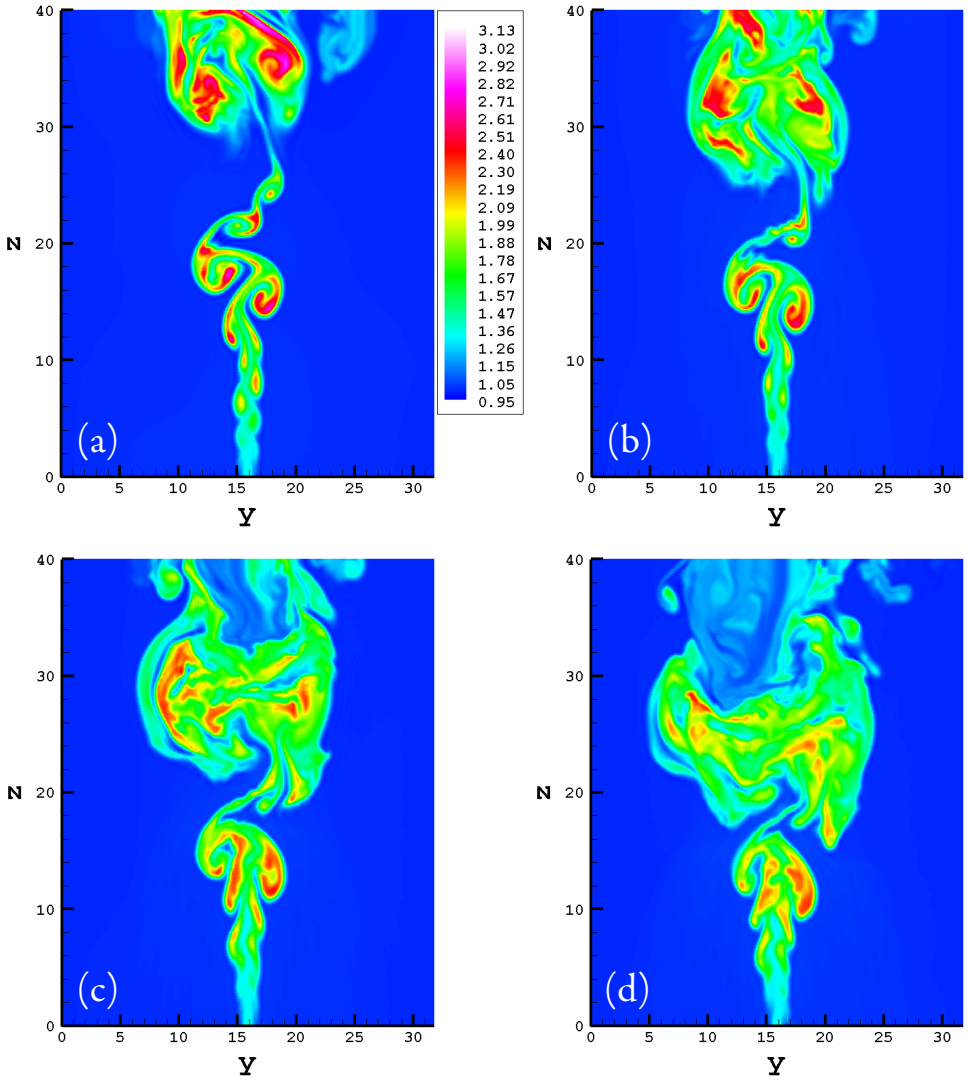

Figure VI-5: The temperature fields at the central plane in the spanwise direction when t = 140 for: (a) Case A, (b) Case B, (c) Case E and (d) Case F.

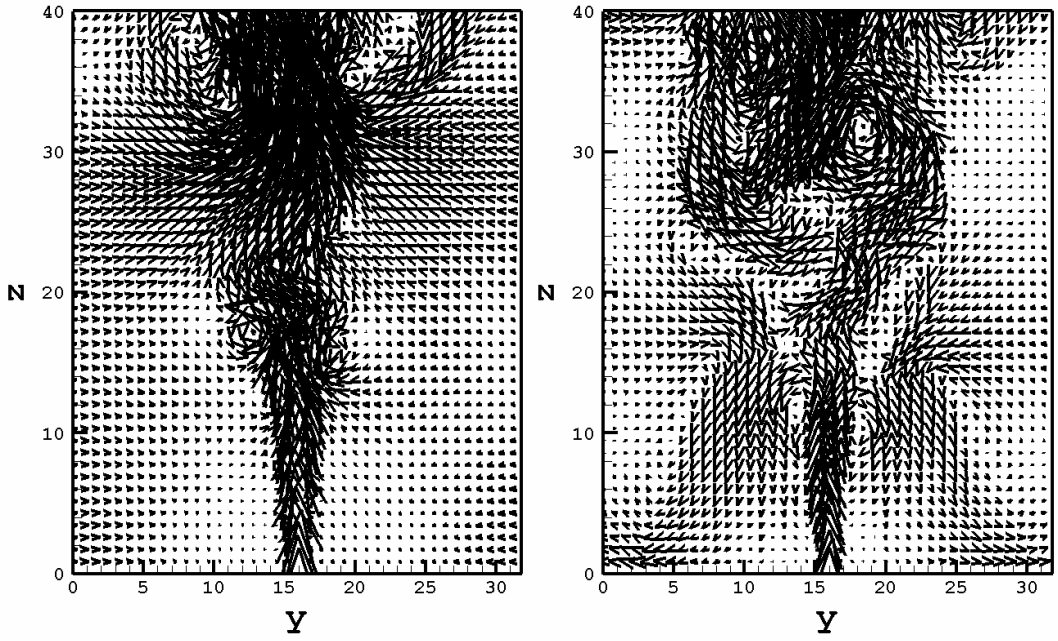

Figure VI-6: The velocity vector fields at the central plane in the spanwise direction when t = 140, left for Case A and right for Case F.

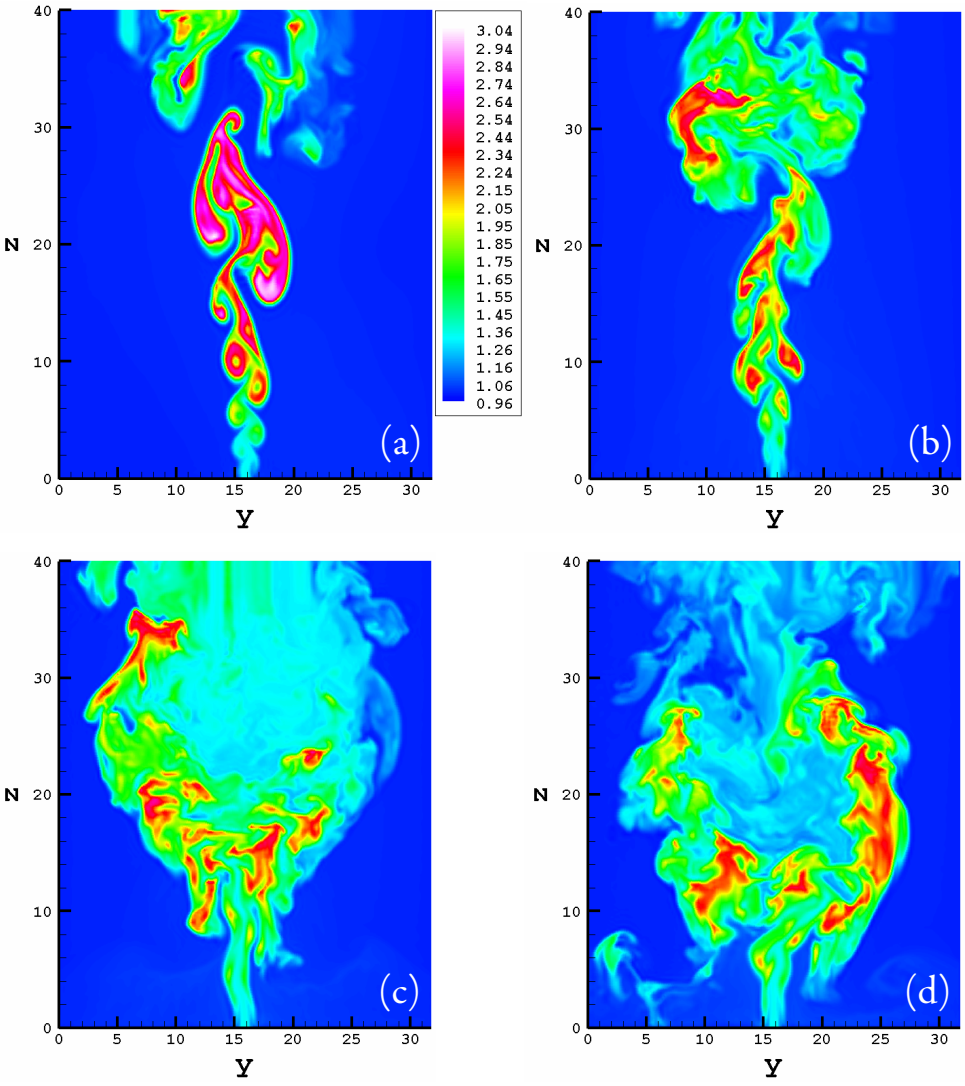

Figure VI-7: The temperature fields at the central plane in the spanwise direction when t = 180 for: (a) Case A, (b) Case B, (c) Case E and (d) Case F.

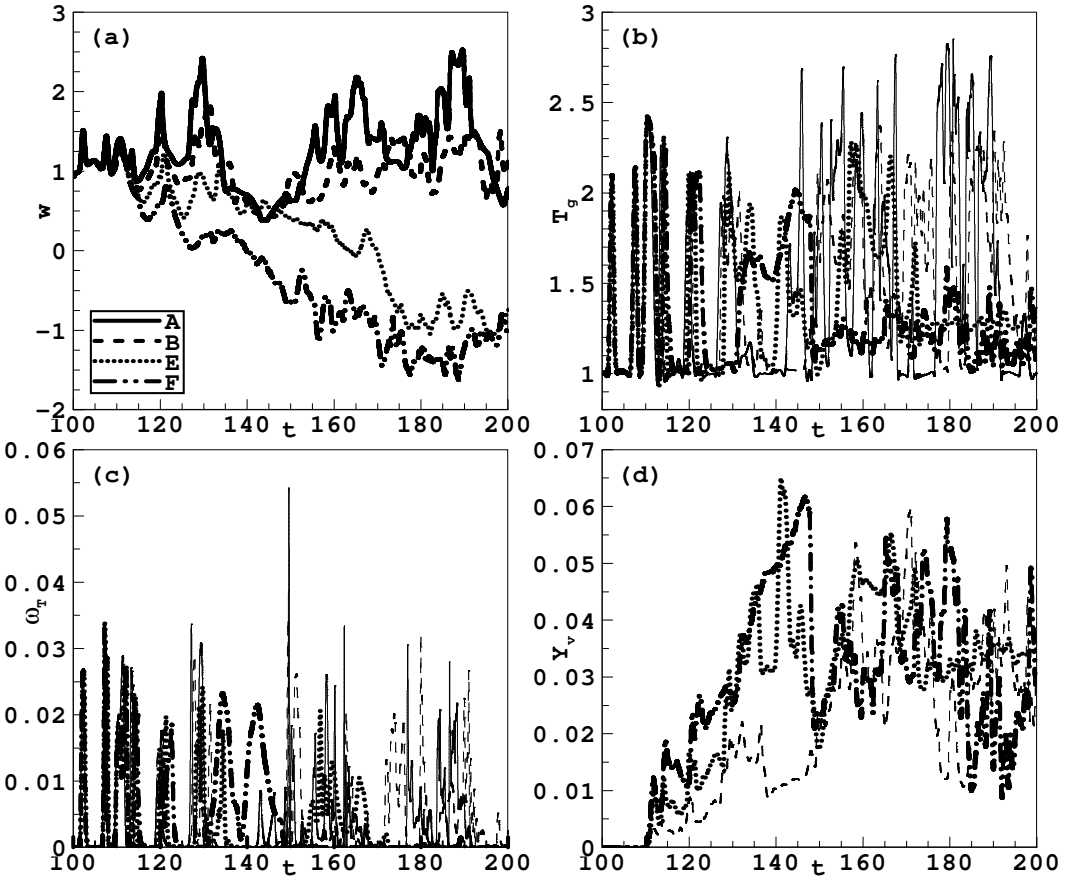

Figure VI-8: Time records of (a) the streamwise velocity w, (b) gas temperature T_g, (c) reaction rate ω_T and (d) the mass fraction of evaporated vapour Y_v, at a downstream point on the plume axis of the central spanwise plane $[x, y, z] = [4, 15.8, 24.08]$ for Cases A, B, E and F.

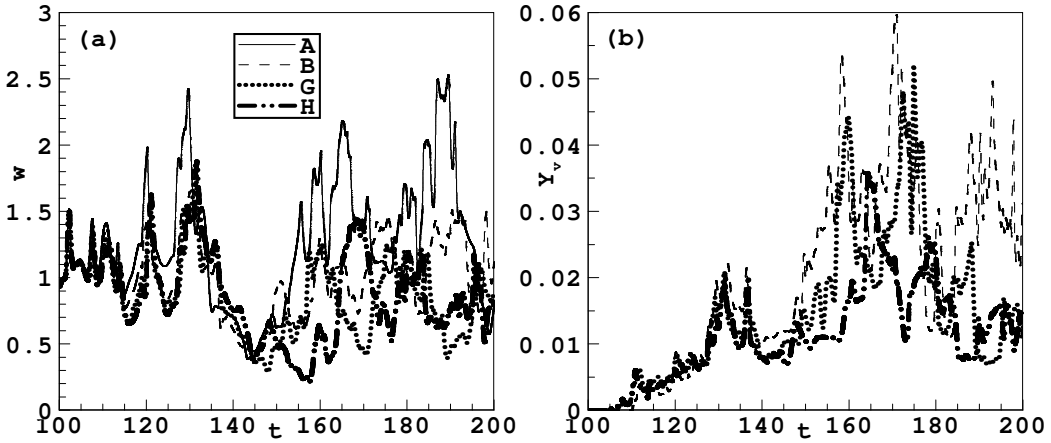

Figure VI-9: Time records of (a) w and (b) Y_v at $[x, y, z] = [4, 15.8, 24.08]$ for Cases A, B, G and H.

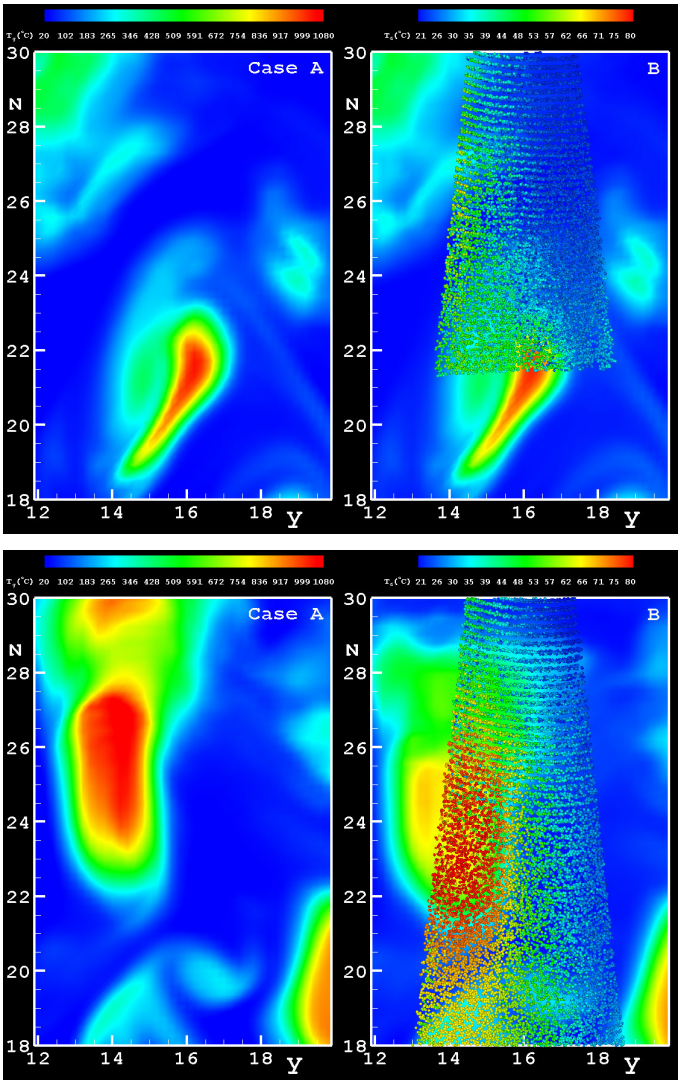

Figure VI-10: Snapshots of interaction between evaporating droplets and the reacting plume at t=109 (top) and t=116 (bottom). The gas temperature has been averaged over the spanwise direction to obtain the contour plots.

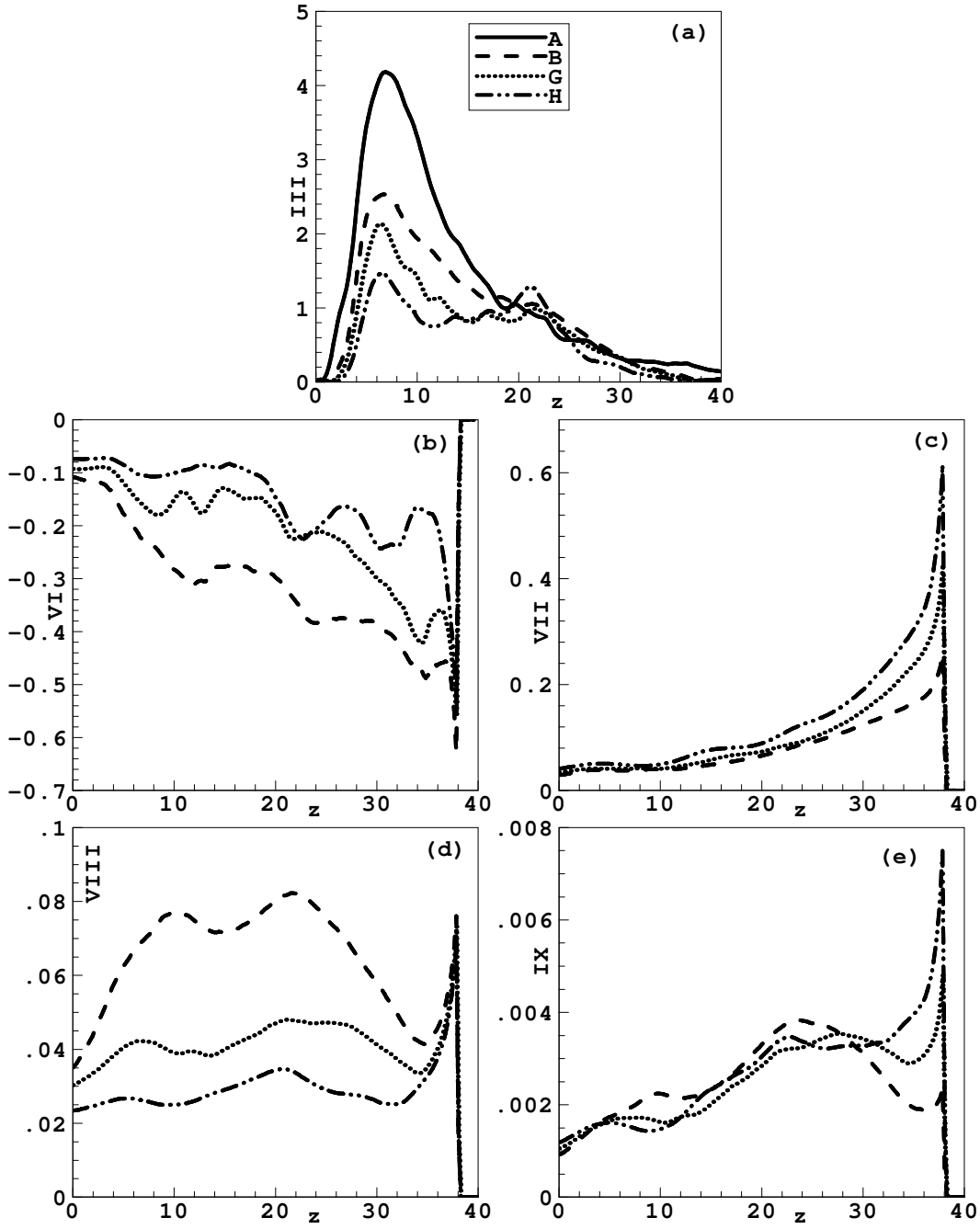

Figure VI-11: Plume centreline budgets of (a) the combustion released heat III and droplet contributions: (b) VI, (c) VII, (d) VIII and (e) IX in Eq. (VI.6) for the Filtered Reduced Internal Energy (FRIE) of the fire plume for Cases A, B, G and H.

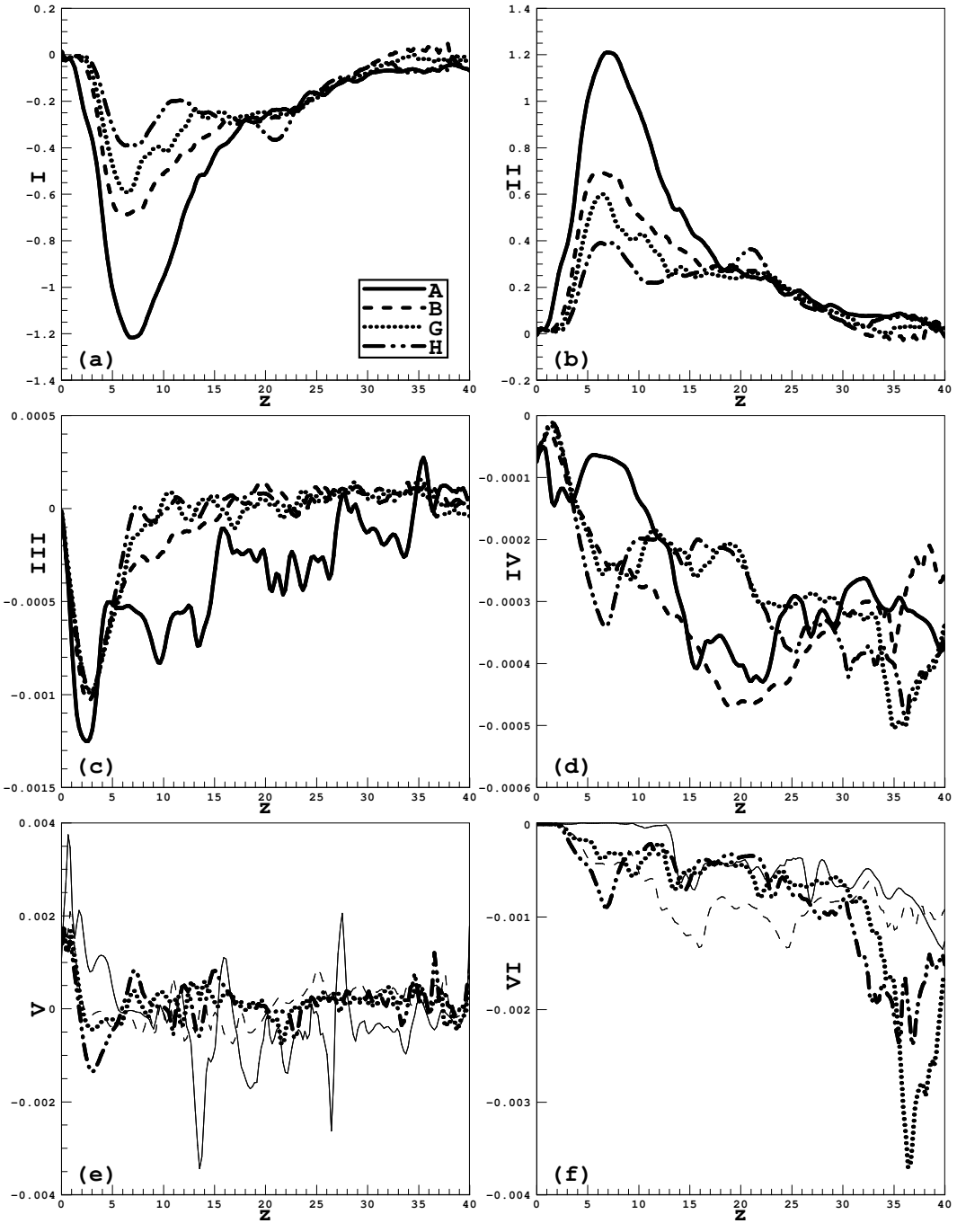
A
B
G
H
(a)
(b)
(c)
(d)
(e)
(f)
I
II
III
IV
V
VI
Z

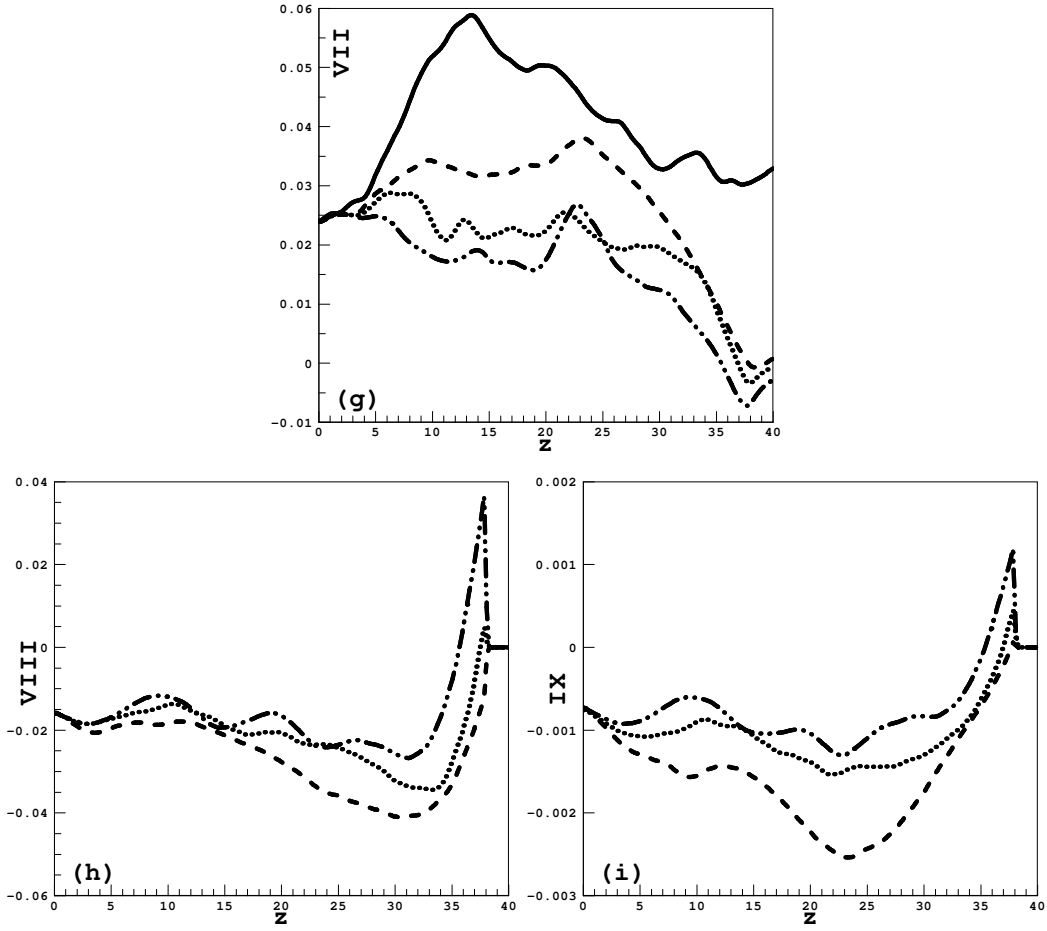

Figure VI-12: Plume centreline budgets of respective terms in Eq. (VI.12) for the Grid-Scale Kinetic Energy (GSKE) of the fire plume for Cases A, B, G and H.

Chapter VII – Thesis Summary

VII.A Summary

In this project, an in-house DNS/LES code has been further developed to investigate the complex interactions between evaporating droplets and reacting flows. The scientific problem studied herein is the non-premixed combustion interacting with water droplets, whose primary role is to inhibit combustion rather than promote combustion as in a spray combustion system. The computational configurations employed in this project are relevant to realistic applications such as fire suppression system, gas turbines, *etc*. The Lagrangian approach is used for the dispersed droplet phase, since the computer capability has been rapidly expanded and massively parallel supercomputers such as HPCx and HECToR become accessible. The outcome of simulations in both canonical and realistic configurations has demonstrated the capability of the developed DNS/LES methodology in capturing the fundamental physics involved in the multilateral interactions between the two phases. These include: self-consistency of the DNS results of a temporal droplet-laden reacting mixing layer as evidenced in the grid independency test, quantitative comparison of the instantaneous and statistical LES results with the experimental results of a heated planar jet in the near field, and qualitative agreement of the LES results with the experimental study of a small-scale fire suppression system. Features of the developed methodology comprises: (1) Careful selection of mathematical models and numerical schemes based on consideration of both the fundamental physics and computational cost. (2) Adoption of the Germano dynamic procedure for the subgrid-scale models in LES. It effectively avoids the tuning of model constants and overcomes the well-known over-dissipative nature of the Smagorinsky model. (3) Careful design of the parallel algorithm, especially for the dispersed

phase, using a domain decomposition strategy and a non-blocking communication mechanism of MPI.

In DNS of a temporal reacting shear layer laden with water droplets, analysis has been focused on the droplet effect on key quantities for combustion modelling. In particular, the conditional scalar dissipation rate $\langle \chi | Z \rangle$ is found to be enhanced by evaporating droplets, which suggests that they can promote micromixing and combustion under certain conditions, in addition to their roles in combustion suppression. The transport equation for the mixture fraction variance $\widetilde{Z''^2}$ has been analyzed, with inclusion of the vaporization-related source terms. Such source terms exhibit more complex local variations in the present shear-flow configuration, compared with the case in the homogeneous decaying turbulence configuration of Réveillon and Vervisch (2000). Specifically, the correlation between the evaporation source and the fluctuation of the mixture fraction $\widetilde{Z''\dot{W}_v}$ exhibits different signs at the fuel-rich and fuel-lean streams, which may have important implications on the relation between evaporation and mixing in such a flow. The analysis is strengthened by the detailed examination of the instantaneous interaction between the phases.

Two spatially developing two-phase flows, i.e., a turbulent reacting jet diluted with droplets and a buoyant reacting plume suppressed by droplets, are studied with the developed dynamic LES methodology. Both of these prototype flows have multiple applications in industrial and domestic devices such as gas turbines and fire suppression systems. The presented field analysis helps the understanding of the dynamics of the droplets in the flow. Especially, the unique characteristic of the St_0~1 droplets, i.e., the preferential concentration, has been well captured in the diluted reacting jet. The implication of this phenomenon for combustion dilution has been discussed, comparing with the performance of droplets of bigger sizes (spray droplets). In the suppression configuration, however, the deployment of smaller droplets is unfavourable due to the fact that they don't have enough momentum to compete with the buoyancy of the fire plume. How the instantaneous plume structures are affected and the fire plume is destroyed due to the increasing mass flow rate of spray droplets have been shown and analyzed. A systematic

method to evaluate quantitatively the droplet effects on the kinetic and internal energy of the gas phase has been proposed. It is useful to distinguish the different mechanisms of interaction. The dynamic effect of droplets due to the inter-phase drag on the kinetic energy is found to be predominant compared to the evaporation effect. The subgrid-scale dissipation rate is enhanced by droplets. Detailed analysis of the budget equation for the internal energy, representing the gas temperature, reveals roles played by the droplet-related terms in combustion suppression. The only "cooling" effect on gas temperature comes from the convective heat transfer between the phases while there are three mechanisms (mechanical work done by droplet drag force, internal energy transfer into the gas phase due to evaporation and kinetic energy interactions between the phases) contributing to "warming" effects. On the whole, evaporating droplets in all cases studied result in significant reduction in reaction rate and gas temperature especially the peak values.

VII.B Recommendations for Future work

This work forms a base for future work on numerical study of multiphase reacting flows using DNS/LES. Step-by-step improvements can be made if various simplifications imposed on the mathematical models are lifted, advanced models for droplet evaporation and LES combustion are developed, or the parallel algorithm is improved, etc. Further studies may address the following topics.

(1) The full validation of the two-phase code is still incomplete. A dataset of multiphase reacting flow designed for CFD validation is unavailable yet. Well-defined numerical (Miller & Bellan 1999) or experimental (Chen *et al.* 2006) results of non-reactive canonical multiphase flow configurations can be found and are suited for the validation purpose.

(2) There is still a big room for improvement in the parallel algorithm, especially for the discrete droplet phase. We have been informed by the Cray engineers that the memory pointer, which is being used to record the droplet data, is not welcomed and generally

causes (considerable) deterioration of parallel performance. In order to improve the parallel code, specific attention should be given to this issue in the first place.

(3) Droplet effects on turbulence can be revealed by the turbulent kinetic energy (TKE) budget analysis, with the droplet source terms incorporated into the TKE equation. Distinct behaviour is expected for droplets with different initial sizes due to their different kinematical and thermodynamic contributions to the flow field. It is also worth investigating how the droplets affect the mixing and entrainment through the vorticity transport equations.

(4) Flow effects on droplets, *e.g.*, the droplet fluctuation velocity, dispersion characteristic, *etc.*, can be investigated under the current configurations of multiphase reactive flows. These are important for the performance of various industrial devices.

(5) Introducing models explicitly to account for the subgrid flow effects on droplets deserves attention. Current work is patchy in this area and considerable modelling work is needed. A fully resolved DNS can be performed to assist the model development.

(6) Droplet-droplet collision could be important in some two-phase flow regimes. Direct or stochastic collision models can be introduced to investigate the importance of this phenomenon, which is generally ignored or accounted for by simple models or corrections currently.

Appendix - The Governing Equations for Reactive and Evaporative Two-Phase Flows

As stated by White (1991), the three fundamental laws of mechanics, conservation of mass, momentum and energy, are Lagrangian in nature. The methodology based on an infinitesimal control mass, i.e., fluid element, is therefore followed to obtain the gas phase governing equations in the framework of evaporating two-phase flow systems. To simplify the writing work, the superscript "*" to designate a dimensional variable with SI units is ignored in this appendix.

A.1 Conservation of Mass

Consider a fluid element which contains an evaporating droplet. The law of mass conservation reads

$$m = m_{\mathrm{g}} + m_{\mathrm{d}} = \mathrm{const} \tag{A.1}$$

Apply the material derivative,

$$\frac{Dm_{\mathrm{g}}}{Dt} + \frac{dm_{\mathrm{d}}}{dt} = 0 \tag{A.2}$$

It should be noted that for the dispersed phase, the convective parts in the material derivative vanish. As in White (1991),

$$\frac{Dm_{\mathrm{g}}}{Dt} = V\left\{\frac{\partial \rho_{\mathrm{g}}}{\partial t} + \frac{\partial\left(\rho_{\mathrm{g}} u_{\mathrm{g},i}\right)}{\partial x_i}\right\} \tag{A.3}$$

Then, (A.2) becomes

$$\frac{\partial \rho_{\mathrm{g}}}{\partial t}+\frac{\partial\left(\rho_{\mathrm{g}} u_{\mathrm{g},i}\right)}{\partial x_i}=-\frac{1}{V}\frac{dm_{\mathrm{d}}}{dt}=-\frac{\dot{m}_{\mathrm{d}}}{V} \tag{A.4}$$

For multi-droplets system, (A.4) can be written as

$$\frac{\partial \rho_{\mathrm{g}}}{\partial t}+\frac{\partial\left(\rho_{\mathrm{g}} u_{\mathrm{g},i}\right)}{\partial x_i}=-\frac{1}{V}\sum_k \dot{m}_{\mathrm{d},k} \tag{A.5}$$

which is the final form of the continuity equation.

A.2 Conservation of Momentum – the Newton's Second Law

Newton's second law states that

$$F_i=\frac{d\left(mu_i\right)}{dt} \tag{A.6}$$

For a combined system of the fluid element with one dispersed droplet, (A.6) can be written as

$$F_i=F_{\mathrm{body},i}+F_{\mathrm{surface},i}=\frac{d\left(m_{\mathrm{g}}u_{\mathrm{g},i}+m_{\mathrm{d}}v_{\mathrm{d},i}\right)}{dt}=\frac{D\left(m_{\mathrm{g}}u_{\mathrm{g},i}\right)}{Dt}+\frac{d\left(m_{\mathrm{d}}v_{\mathrm{d},i}\right)}{dt} \tag{A.7}$$

For the first term on the right-hand-side (RHS) of (A.7), we have

$$\frac{D\left(m_{\mathrm{g}}u_{\mathrm{g},i}\right)}{Dt}=V\frac{D\left(\rho_{\mathrm{g}}u_{\mathrm{g},i}\right)}{Dt}=V\left\{\frac{\partial\left(\rho_{\mathrm{g}}u_{\mathrm{g},i}\right)}{\partial t}+\frac{\partial\left(\rho_{\mathrm{g}}u_{\mathrm{g},i}u_{\mathrm{g},j}\right)}{\partial x_j}\right\} \tag{A.8}$$

And the second term

$$\frac{d\left(m_{\mathrm{d}}v_{\mathrm{d},i}\right)}{dt}=m_{\mathrm{d}}\frac{dv_{\mathrm{d},i}}{dt}+\frac{dm_{\mathrm{d}}}{dt}v_{\mathrm{d},i} \tag{A.9}$$

Substitute the droplet momentum equation into (A.9),

$$\frac{d\left(m_{\mathrm{d}}v_{\mathrm{d},i}\right)}{dt}=F_{\mathrm{drag},i}+m_{\mathrm{d}}g_i+\dot{m}_{\mathrm{d}}v_{\mathrm{d},i} \tag{A.10}$$

The external body forces (F_{body}) include the buoyancy force for the fluid element and the gravitational force for the droplet. In the present study, the ratio of droplet to fluid densities is taken to be ~1000, so the buoyancy force exerted on the droplet, which is submerged in the flow, can be ignored. The bubble-laden liquid flow is a different situation. The external surface forces (F_{surface}) are the normal and shear stresses. Thus,

$$F_{\text{body},i} = -\left(\rho_{\text{a}} - \rho_{\text{g}}\right) V g_i + m_{\text{d}} g_i \tag{A.11}$$

$$F_{\text{surface},i} = V\left(-\frac{\partial p}{\partial x_i} + \frac{\partial \sigma_{ij}}{\partial x_j}\right) \tag{A.12}$$

The detailed derivation procedure for (A.12) can be found in White (1991). Substitute (A.8), (A.10), (A.11) and (A.12) into (A.7),

$$\frac{\partial\left(\rho_{\text{g}} u_{\text{g},i}\right)}{\partial t} + \frac{\partial\left(\rho_{\text{g}} u_{\text{g},i} u_{\text{g},j}\right)}{\partial x_j} + \frac{1}{V}\left(F_{\text{drag},i} + \dot{m}_{\text{d}} v_{\text{d},i}\right) = -\left(\rho_{\text{a}} - \rho_{\text{g}}\right) g_i - \frac{\partial p}{\partial x_i} + \frac{\partial \sigma_{ij}}{\partial x_j} \tag{A.13}$$

The term $m_{\text{d}}g_i$ has been crossed out due to its appearance on both sides of (A.13). Finally, if multiple droplets are concerned, (A.13) becomes

$$\frac{\partial\left(\rho_{\text{g}} u_{\text{g},i}\right)}{\partial t} + \frac{\partial}{\partial x_j}\left(\rho_{\text{g}} u_{\text{g},i} u_{\text{g},j} + p\delta_{ij} - \sigma_{ij}\right) + \left(\rho_{\text{a}} - \rho_{\text{g}}\right) g_i = -\frac{1}{V}\sum_k \left(F_{\text{drag},k,i} + \dot{m}_{\text{d},k} v_{\text{d},k,i}\right) \tag{A.14}$$

A.3 Conservation of Energy – the First Law of Thermodynamics

The first law of thermodynamics can be written as

$$\frac{dE}{dt} = \frac{dQ}{dt} + \frac{dW}{dt} \tag{A.15}$$

And,

$$E = E_{\text{g}} + E_{\text{d}} \tag{A.16}$$

$$E_{\mathrm{g}} = m_{\mathrm{g}}\left(e_{\mathrm{g}} + \frac{1}{2} u_{\mathrm{g},i} u_{\mathrm{g},i} \right) = V E_{\mathrm{T}} \tag{A.17}$$

$$E_{\mathrm{d}} = m_{\mathrm{d}}\left(e_{\mathrm{d}} + \frac{1}{2} v_{\mathrm{d},i} v_{\mathrm{d},i} \right) \tag{A.18}$$

The potential energy is ignored in (A.17) and (A.18).

$$\frac{DE_{\mathrm{g}}}{Dt} = V\left\{ \frac{\partial E_{\mathrm{T}}}{\partial t} + \frac{\partial\left(E_{\mathrm{T}} u_{\mathrm{g},i} \right)}{\partial x_i} \right\} \tag{A.19}$$

$$\frac{dE_{\mathrm{d}}}{dt} = \frac{d\left\{ m_{\mathrm{d}}\left(e_{\mathrm{d}} + \frac{1}{2} v_{\mathrm{d},i} v_{\mathrm{d},i} \right) \right\}}{dt} = m_{\mathrm{d}} \frac{de_{\mathrm{d}}}{dt} + m_{\mathrm{d}} v_{\mathrm{d},i} \frac{dv_{\mathrm{d},i}}{dt} + \frac{dm_{\mathrm{d}}}{dt} e_{\mathrm{d}} + \frac{dm_{\mathrm{d}}}{dt}\left(\frac{1}{2} v_{\mathrm{d},i} v_{\mathrm{d},i} \right) \tag{A.20}$$

As in Sandham (1989), the reference internal energy is set to zero at T=0 for the liquid phase, so e_{d}=$c_{\mathrm{d}}T_{\mathrm{d}}$, where c_{d} is assumed to be constant. The difference between the specific heat capacity at constant pressure and constant volume for the droplet is very small, so a unified c_{d} is used here. Substitute the droplet temperature and momentum equations into (A.20) for the first and second terms on the RHS,

$$\frac{dE_{\mathrm{d}}}{dt} = h_{\mathrm{t}} A_{\mathrm{d}}\left(T_{\mathrm{g}} - T_{\mathrm{d}} \right) + \dot{m}_{\mathrm{d}} h_{\mathrm{fg}} + F_{\mathrm{drag},i} v_{\mathrm{d},i} + m_{\mathrm{d}} g_i v_{\mathrm{d},i} + \dot{m}_{\mathrm{d}} c_{\mathrm{d}} T_{\mathrm{d}} + \frac{1}{2} \dot{m}_{\mathrm{d}} v_{\mathrm{d},i} v_{\mathrm{d},i} \tag{A.21}$$

The rate of work done to the combined element is due to the gravity and stresses, and the rate of heat consists of the conduction heat from the neighbour elements, which is represented by the Fourier's law, and the heat of combustion, i.e.,

$$\frac{dQ}{dt} = V\left(-\frac{\partial q_i}{\partial x_i} - \sum_{n=1}^{N_{\mathrm{s}}} \Delta h_{\mathrm{f},n}^{0} \dot{\omega}_n \right) \tag{A.22}$$

$$\frac{dW}{dt} = -\left(\rho_{\mathrm{a}} - \rho_{\mathrm{g}} \right) V g_i u_{\mathrm{g},i} + m_{\mathrm{d}} g_i v_{\mathrm{d},i} + V \frac{\partial}{\partial x_i}\left(-p u_{\mathrm{g},i} + u_{\mathrm{g},j} \sigma_{ij} \right) \tag{A.23}$$

Detailed information was given in White (1991) for the non-reactive terms in the above two equations. Substitute (A.19), (A.21), (A.22) and (A.23) into (A.15),

$$\frac{\partial E_{\mathrm{T}}}{\partial t}+\frac{\partial\left(E_{\mathrm{T}}u_{\mathrm{g},i}\right)}{\partial x_i}+\frac{1}{V}\left\{h_{\mathrm{t}}A_{\mathrm{d}}\left(T_{\mathrm{g}}-T_{\mathrm{d}}\right)+\dot{m}_{\mathrm{d}}h_{\mathrm{fg}}+F_{\mathrm{drag},i}v_{\mathrm{d},i}+\dot{m}_{\mathrm{d}}c_{\mathrm{d}}T_{\mathrm{d}}+\frac{1}{2}\dot{m}_{\mathrm{d}}v_{\mathrm{d},i}v_{\mathrm{d},i}\right\}$$
$$=-\frac{\partial q_i}{\partial x_i}-\sum_{n=1}^{N_{\mathrm{s}}}\Delta h_{\mathrm{f},n}^{0}\dot{\omega}_n-\left(\rho_{\mathrm{a}}-\rho_{\mathrm{g}}\right)g_iu_{\mathrm{g},i}+\frac{\partial}{\partial x_i}\left(-pu_{\mathrm{g},i}+u_{\mathrm{g},j}\sigma_{ij}\right) \tag{A.24}$$

The term $m_{\mathrm{d}}g_iv_{\mathrm{d},i}$ disappears due to its appearance on both sides of (A.24). As for a fluid element containing multiple droplets, (A.24) becomes

$$\frac{\partial E_{\mathrm{T}}}{\partial t}+\frac{\partial\left[\left(E_{\mathrm{T}}+p\right)u_{\mathrm{g},i}+q_i-u_{\mathrm{g},j}\sigma_{ij}\right]}{\partial x_i}+\left(\rho_{\mathrm{a}}-\rho_{\mathrm{g}}\right)g_iu_{\mathrm{g},i}+\sum_{n=1}^{N_{\mathrm{s}}}\Delta h_{\mathrm{f},n}^{0}\dot{\omega}_n$$
$$=-\frac{1}{V}\sum_k\left\{\begin{array}{l}h_{\mathrm{t},k}A_{\mathrm{d},k}\left(T_{\mathrm{g},k}-T_{\mathrm{d},k}\right)+\dot{m}_{\mathrm{d},k}h_{\mathrm{fg}}+F_{\mathrm{drag},k,i}v_{\mathrm{d},k,i}\\+\dot{m}_{\mathrm{d},k}c_{\mathrm{d}}T_{\mathrm{d},k}+\frac{1}{2}\dot{m}_{\mathrm{d},k}v_{\mathrm{d},k,i}v_{\mathrm{d},k,i}\end{array}\right\} \tag{A.25}$$

A.4 Conservation Equations for Species

The transport process of various species can be described by the general convection-diffusion equation,

$$\frac{\partial\left(\rho_{\mathrm{g}}Y_n+m_n/V\right)}{\partial t}+\frac{\partial\left(\rho_{\mathrm{g}}Y_nu_{\mathrm{g},i}\right)}{\partial x_i}=\frac{\partial}{\partial x_i}\left(\rho_{\mathrm{g}}D\frac{\partial Y_n}{\partial x_i}\right) \tag{A.26}$$

where m_k accounts for the additional mass source due to reaction or evaporation. The Fick's law has been employed to describe the mass diffusion. Identical mass diffusion property is assumed for different species by a unified diffusion coefficient, D. For fuel and oxidizer,

$$\frac{1}{V}\frac{\partial m_n}{\partial t}=-\dot{\omega}_n \tag{A.27}$$

while for liquid vapour, the source term is same as in (A.5). To sum up, the final forms of species equations are

$$\frac{\partial\left(\rho_{\mathrm{g}}Y_n\right)}{\partial t}+\frac{\partial\left(\rho_{\mathrm{g}}Y_nu_{\mathrm{g},i}\right)}{\partial x_i}=\frac{\partial}{\partial x_i}\left(\rho_{\mathrm{g}}D\frac{\partial Y_n}{\partial x_i}\right)+\dot{\omega}_n \tag{A.28}$$

for fuel and oxidizer, and

$$\frac{\partial\left(\rho_{\mathrm{g}} Y_{\mathrm{v}}\right)}{\partial t}+\frac{\partial\left(\rho_{\mathrm{g}} Y_{\mathrm{v}} u_{\mathrm{g},i}\right)}{\partial x_i}=\frac{\partial}{\partial x_i}\left(\rho_{\mathrm{g}} D \frac{\partial Y_{\mathrm{v}}}{\partial x_i}\right)-\frac{1}{V}\sum_k \dot{m}_{\mathrm{d},k} \tag{A.29}$$

for liquid vapour, respectively.

Bibliography

- Abdel-Hameed H. and Bellan J. *"Direct Numerical Simulation of Two-Phase Laminar Jet Flows with Different Cross-Section Injection Geometries"* Physics of Fluids, Vol. 14 (10) 3655-3674, 2002.
- Akhavan R., Ansari A., Kang S. and Mangiavacchi N. *"Subgrid-Scale Interactions in a Numerically Simulated Planar Turbulent Jet and Implications for Modelling"* Journal of Fluid Mechanics, Vol. 408 83-120, 2000.
- Apte S.V., Mahesh K., Moin P. and Oefelein J.C. *"Large-Eddy Simulation of Swirling Particle-Laden Flows in a Coaxial-Jet Combustor"* International Journal of Multiphase Flow, Vol. 29 (8) 1311-1331, 2003.
- Armenio V., Piomelli U. and Fiorotto V. *"Effect of the Subgrid Scales on Particle Motion"* Physics of Fluids, Vol. 11(10) 3030-3042, 1999.
- Balachandar S. and Maxey M.R. *"Methods for Evaluating Fluid Velocities in Spectral Simulations of Turbulence"* Journal of Computational Physics, Vol. 83 (1) 96-125, 1989.
- Bilger R.W. *"Turbulent Jet Diffusion Flames"* Progress in Energy and Combustion Science, Vol. 1 (2-3) 87-109, 1976.
- Bilger R.W. *"Turbulent-Diffusion Flames"* Annual Review of Fluid Mechanics, Vol. 21 101-135, 1989.
- Bilger R.W. *"Conditional Moment Closure for Turbulent Reacting Flow"* Physics of Fluids A, Vol. 5 (2) 436-444, 1993.

- Bilger R.W. *"Some Aspects of Scalar Dissipation"* Flow Turbulence and Combustion, Vol. 72 93-114, 2004.
- Boivin M., Simonin O. and Squires K.D. *"Direct Numerical Simulation of Turbulence Modulation by Particles in Isotropic Turbulence"* Journal of Fluid Mechanics, Vol. 375 235-263, 1998.
- Boivin M., Simonin O. and Squires K.D. *"On the Prediction of Gas-Solid Flows with Two-Way Coupling Using Large Eddy Simulation"* Physics of Fluids, Vol. 12 (8) 2080-2090, 2000.
- Burton T.M. and Eaton J.K. *"Fully Resolved Simulations of Particle-Turbulence Interaction"* Journal of Fluid Mechanics, Vol. 545 67-111, 2005.
- Chelliah H.K. *"Flame Inhibition/Suppression by Water Mist: Droplet Size/Surface Area, Flame Structure, and Flow Residence Time Effects"* Proceedings of the Combustion Institute, Vol. 31 2711-2719, 2007.
- Chen Y.C., Starner S.H. and Masri A.R. *"A Detailed Experimental Investigation of Well-Defined, Turbulent Evaporating Spray Jets of Acetone"* International Journal of Multiphase Flow, Vol. 32 (4) 389-412, 2006.
- Colonius T. *"Modeling Artificial Boundary Conditions for Compressible Flow"* Annual Review of Fluid Mechanics, Vol. 36 315-345, 2004.
- Cox G. *"Fire Research in the 21st Century"* Fire Safety Journal, Vol. 32 203-219, 1999.
- Crowe C.T., Sharma M.P. and Stock D.E. *"Particle-Source in Cell (PSI-CELL) Model for Gas-Droplet Flows"* Journal of Fluids Engineering – Transactions of the ASME, Vol. 99 (2) 325-332, 1977.
- Crowe C.T., Sommerfeld M. and Tsuji Y. *"Multiphase Flows with Droplets and Particles"* CRC Press, 1998.
- Crowe C.T., Troutt T.R. and Chung J.N. *"Numerical Models for Two-Phase Turbulent Flows"* Annual Review of Fluid Mechanics, Vol. 28 11-43, 1996.

- Da Silva C.B. and Métais O. *"On the Influence of Coherent Structures upon Interscale Interactions in Turbulent Plane Jets"* Journal of Fluid Mechanics, Vol. 473 103-145, 2002.
- DesJardin P.E. and Frankel S.H. *"Large Eddy Simulation of a Nonpremixed Reacting Jet: Application and Assessment of Subgrid-Scale Combustion Models"* Physics of Fluids, Vol. 10 (9) 2298-2314, 1998.
- DesJardin P.E., O'Hern T.J. and Tieszen S.R. *"Large Eddy Simulation and Experimental Measurements of the Near-Field of a Large Turbulent Helium Plume"* Physics of Fluids, Vol. 16 (6) 1866-1883, 2004.
- Dimotakis P.E. *"Turbulent Mixing"* Annual Review of Fluid Mechanics, Vol. 37 329-356, 2005.
- Domingo P., Vervisch L. and Bray K. *"Partially Premixed Flamelets in LES of Nonpremixed Turbulent Combustion"* Combustion Theory and Modelling, Vol. 6 (4) 529-551, 2002.
- Domingo P., Vervisch L. and Reveillon J. *"DNS Analysis of Partially Combustion in Spray and Gaseous Turbulent Flame-Bases Stabilized in Hot Air"* Combustion and Flame, Vol. 140 (3) 172-195, 2005.
- Dvorjetski A. and Greenberg J.B. *"Theoretical Analysis of Polydisperse Water Spray Extinction of Opposed Flow Diffusion Flames"* Fire Safety Journal, Vol. 39 309-326, 2004.
- Elghobashi S. and Truesdell G.C. *"Direct Simulation of Particle Dispersion in a Decaying Isotropic Turbulence"* Journal of Fluid Mechanics, Vol. 242 655-700, 1992.
- Elghobashi S. and Truesdell G.C. *"On the 2-way Interaction between Homogeneous Turbulence and Dispersed Solid Particles .1. Turbulence Modification"* Physics of Fluids A – Fluid Dynamics, Vol. 5 (7) 1790-1801, 1993.
- Elghobashi S., Zhong R. and Boratav O. *"Effects of Gravity on Turbulent Nonpremixed Flames"* Physics of Fluids, Vol. 11 (10) 3123-3135, 1999.

- Faeth G.M. *"Mixing, Transport and Combustion in Sprays"* Progress in Energy and Combustion Science, Vol. 13 (4) 293-345, 1987.
- Fede P. and Simonin O. *"Numerical Study of the Subgrid Fluid Turbulence Effects on the Statistics of Heavy Colliding Particles"* Physics of Fluids, Vol. 18 (4) Art. No. 045103, 2006.
- Fernandez-Tarrazo E., Sanchez A.L., Linan A. and Williams F.A. *"A simple one-step chemistry model for partially premixed hydrocarbon combustion"* Combustion and Flame, Vol. 147 (1-2) 32-38, 2006.
- Ferziger J.H. and Peric M. *"Computational Methods for Fluid Dynamics (3rd Edition)"* Springer, 2004.
- Fisher B.T., Awtry A.R., Sheinson R.S. and Fleming J.W. *"Flow Behavior Impact on the Suppression Effectiveness of Sub-10-μm Water Drops in Propane/Air Co-Flow Non-Premixed Flames"* Proceedings of the Combustion Institute, Vol. 31 2731-2739, 2007.
- Fuss S.P., Chen E.F., Yang W.H., Kee R.J., Williams B.A. and Fleming J.W. *"Inhibition of Premixed Methane/Air Flames by Water Mist"* Proceedings of the Combustion Institute**,** Vol. 29 361-368, 2002.
- Gago C.F., Garnier F. and Utheza F. *"Direct testing of subgrid scale models in large-eddy simulation of a non-isothermal turbulent jet"* International Journal for Numerical Methods in Fluids, Vol. 42 (9) 999-1026, 2003.
- Gaitonde D.V. and Visbal M.R. *"Pade-Type Higher-Order Boundary Filters for the Navier-Stokes Equations"* AIAA Journal, Vol. 38 (11) 2103-2112, 2000.
- Germano M., Piomelli U., Moin P. and Cabot W.H. *"A Dynamic Subgrid-Scale Eddy Viscosity Model"* Physics of Fluids A – Fluid Dynamics, Vol. 3 (7) 1760-1765, 1991.
- Ghosal S., Lund T.S., Moin P. and Akselvoll K. *"A Dynamic Localization Model for Large-Eddy Simulation of Turbulent Flows"* Journal of Fluid Mechanics, Vol. 286 229-255, 1995.

- Göz M.F., Lain S. and Sommerfeld M. *"Study of the Numerical Instabilities in Lagrangian Tracking of Bubbles and Particles in Two-Phase Flow"* Computers and Chemical Engineering, Vol. 28 (12) 2727-2733, 2004.
- Grant G., Brenton J. and Drysdale D. *"Fire Suppression by Water Sprays"* Progress in Energy and Combustion Science, Vol. 26 (2) 79-130, 2000.
- Gutmark E. and Wygnanski I. *"The Planar Turbulent Jet"* Journal of Fluid Mechanics, Vol. 73 465-495, 1976.
- Hadinoto K., Jones E.N., Yurteri C. and Curtis J.S. *"Reynolds Number Dependence of Gas-Phase Turbulence in Gas-Particle Flows"* International Journal of Multiphase Flow, Vol. 31 (4) 416-434, 2005.
- Hu Z.W., Luo X.Y. and Luo K.H. *"Numerical Simulation of Particle Dispersion in a Spatially Developing Mixing Layer"* Theoretical and Computational Fluid Dynamics, Vol. 15 (6) 403-420, 2002.
- Hussain A.K.M.F. and Clark A.R. *"Upstream Influence on Near-Field of a Plane Turbulent Jet"* Physics of Fluids, Vol. 20 (9) 1416-1426, 1977.
- Janicka J. and Sadiki A. *"Large Eddy Simulation of Turbulent Combustion Systems"* Proceedings of the Combustion Institute, Vol. 30 537-547, 2005.
- Jiang X. and Luo K.H. *"Spatial Direct Numerical Simulation of the Large Vortical Structures in Forced Plumes"* Flow Turbulence and Combustion, Vol. 64 (1) 43-69, 2000a.
- Jiang X. and Luo K.H. *"Combustion-Induced Buoyancy Effects of an Axisymmetric Reactive Plume"* Proceedings of the Combustion Institute, Vol. 28 1989-1995, 2000b.
- Jiang X. and Luo K.H. *"Direct Numerical Simulation of the Near Field Dynamics of a Rectangular Reactive Plume"* International Journal of Heat and Fluid Flow, Vol. 22 (6) 633-642, 2001a.

- Jiang X. and Luo K.H. *"Mixing and Entrainment of Transitional Non-Circular Buoyant Reactive Plumes"* Flow Turbulence and Combustion, Vol. 67 (1) 57-79, 2001b.
- Jonsson M. and Yan J.Y. *"Humidified Gas Turbines – a Review of Proposed and Implemented Cycles"* Energy, Vol. 30 (7) 1013-1078, 2005.
- Kajishima T. *"Influence of Particle Rotation on the Interaction between Particle Clusters and Particle-Induced Turbulence"* International Journal of Heat and Fluid Flow, Vol. 25 (5) 721-728, 2004.
- Kee R.J., Zhu H.Y. and Goodwin D.G. *"Solid-Oxide Fuel Cells with Hydrocarbon Fuels"* Proceedings of the Combustion Institute, Vol. 30 2379-2404, 2005.
- Kempf A., Lindstedt R.P. and Janicka J. *"Large-Eddy Simulation of a Bluff-Body Stabilized Nonpremixed Flame"* Combustion and Flame, Vol. 144 (1-2) 170-189, 2006.
- Kempf A.M. *"LES Validation from Experiments"* Flow Turbulence and Combustion, DOI 10.1007/s10494-007-9128-9.
- Kempf A., Klein M. and Janicka J. *"Efficient generation of initial- and inflow-conditions for transient turbulent flows in arbitrary geometries"* Flow Turbulence and Combustion, Vol. 74 (1) 67-84, 2005.
- Klein M. *"An Attempt to Assess the Quality of Large Eddy Simulations in the Context of Implicit Filtering"* Flow Turbulence and Combustion, Vol. 75 (1-4) 131-147, 2005.
- Kornev N. and Hassel E. *"Synthesis of homogeneous anisotropic divergence-free turbulent fields with prescribed second-order statistics by vortex dipoles"* Physics of Fluids, Vol. 19 (6) Art. No. 067101, 2007.
- Kuerten J.G.M. and Vreman A.W. *"Can Turbophoresis Be Predicted by Large-Eddy Simulation?"* Physics of Fluids, Vol. 17 (1) Art. No. 011701, 2005.
- Kumar S., Heywood G.M. and Liew S.K. *"Superdrop Modeling of a Sprinkler Spray in a Two-Phase CFD-Particle Tracking Model"* Proceedings of the 5th International Symposium, International Association for Fire Safety Science, 889-900, 1997.

- Kurose R., Makino H., Michioka T. and Komori S. *"Large Eddy Simulation of a Non-Premixed Turbulent Reacting Mixing Layer: Effects of Heat Release and Span-wise Fluid Shear"* Combustion and Flame, Vol. 127 (3) 2157-2163, 2001.
- Larcheveque L., Sagaut P., Mary I. and Labbe O. *"Large-eddy simulation of a compressible flow past a deep cavity"* Physics of Fluids, Vol. 15 (1) 193-210, 2003.
- Le Ribault C., Sarkar S. and Stanley S.A. *"Large Eddy Simulation of a Plane Jet"* Physics of Fluids, Vol. 11 (10) 3069-3083, 1999.
- Leboissetier A., Okong'o N. and Bellan J. *"Large Eddy Simulation of Jets Laden with Evaporating Drops"* AIAA paper 1170, 2004.
- Leboissetier A., Okong'o N. and Bellan J. *"Consistent Large-Eddy Simulation of a Temporal Mixing Layer Laden with Evaporating Drops. Part 2. A posteriori Modelling"* Journal of Fluid Mechanics, Vol. 523 37-78, 2005.
- Lele S.K. *"Compact Finite-Difference Schemes with Spectral-Like Resolution"* Journal of Computational Physics, Vol. 103 (1) 16-42, 1992.
- Lenormand E., Sagaut P., Phuoc L.T. and Comte P. *"Subgrid-scale models for large-eddy simulations of compressible wall bounded flows"* AIAA Journal, Vol. 38 (8) 1340-1350, 2000.
- Lentati A.M. and Chelliah H.K. *"Dynamics of Water Droplets in a Counterflow Field and their Effect on Flame Extinction"* Combustion and Flame, Vol. 115 158-179, 1998a.
- Lentati A.M. and Chelliah H.K. *"Physical, Thermal, and Chemical Effects of Fine-Water Droplets in Extinguishing Counterflow Diffusion Flames"* Proceedings of the Combustion Institute, Vol. 27 2839-2946, 1998b.
- Lilly D.K. *"A Proposed Modification of the Germano-Subgrid-Scale Closure Method"* Physics of Fluids A – Fluid Dynamics, Vol. 4 (3) 633-635, 1992.

- Ling W., Chung J.N. and Crowe C.T. "*Direct Numerical Simulation of a Two-Way Thermally Coupled Droplet-Laden Mixing Layer*" Journal of Fluid Mechanics, Vol. 437 45-68, 2001.
- Luo K.H. *"Combustion Effects on Turbulence in a Partially Premixed Supersonic Diffusion Flame"* Combustion and Flame, Vol. 119 (4) 417-435, 1999.
- Luo K.H. *"Instabilities, Entrainment and Mixing in Reacting Plumes"* European Journal of Mechanics B – Fluids, Vol. 23 (3) 443-460, 2004.
- Luo K.H. *"New Opportunities and Challenges in Fire Dynamics Modelling"* Proceedings of the Fourth International Seminar on Fire and Explosion Hazards, 39-52, 2004.
- Martin M.P., Piomelli U. and Candler G.V. *"Subgrid-scale models for compressible large-eddy simulations"* Theoretical and Computational Fluid Dynamics, Vol. 13 (5) 361-376, 2000.
- Mashayek F. *"Droplet-Turbulence Interactions in Low-Mach-Number Homogeneous Shear Two-Phase Flows"* Journal of Fluid Mechanics, Vol. 367 163-203, 1998.
- Mashayek F. *"Numerical Investigation of Reacting Droplets in Homogeneous Shear Turbulence"* Journal of Fluid Mechanics, Vol. 405 1-36, 2000.
- Mashayek F., Jaberi F.A., Miller R.S. and Givi P. *"Dispersion and Polydispersity of Droplets in Stationary Isotropic Turbulence"* International Journal of Multiphase Flow, Vol. 23 (2) 337-355, 1997.
- McCaffrey B.J. *"Jet Diffusion Flame Suppression Using Water Sprays – An Interim Report"* Combustion Science and Technology, Vol. 40 107-136, 1984.
- McCaffrey B.J. *"Momentum Diffusion Flame Characteristics and the Effects of Water Spray"* Combustion Science and Technology, Vol. 63, 315-335, 1989.

- Michioka T., Kurose R., Sada K. and Makino H. *"Direct Numerical Simulation of a Particle-Laden Mixing Layer with a Chemical Reaction"* International Journal of Multiphase Flow, Vol. 31 (7) 843-866, 2005.
- Miller R.S. *"Effects of Nonreacting Solid Particle and Liquid Droplet Loading on an Exothermic Reacting Mixing Layer"* Physics of Fluids, Vol. 13 (11) 3303-3320, 2001.
- Miller R.S. and Bellan J. *"Direct Numerical Simulation of a Confined Three-Dimensional Gas Mixing Layer with One Evaporating Hydrocarbon-Droplet-Laden Stream"* Journal of Fluid Mechanics, Vol. 384 293-338, 1999.
- Miller R.S. and Bellan J. *"Direct Numerical Simulation and Subgrid Analysis of a Transitional Droplet Laden Mixing Layer"* Physics of Fluids, Vol. 12 (3) 650-671, 2000.
- Miller R.S., Harstad K. and Bellan J. *"Evaluation of Equilibrium and Non-Equilibrium Evaporation Models for Many-Droplet Gas-Liquid Flow Simulations"* International Journal of Multiphase Flow, Vol. 24 (6) 1025-1055, 1998.
- Mittal R. and Iaccarino G. *"Immersed Boundary Methods"* Annual Review of Fluid Mechanics, Vol. 37 239-261, 2005.
- Moin P., Squires K., Cabot W. and Lee S. *"A Dynamic Subgrid-Scale Model for Compressible Turbulence and Scalar Transport"* Physics of Fluids A – Fluid Dynamics, Vol. 3 (11) 2746-2757, 1991.
- Monkewitz P.A., Bechert D.W., Barsikow B. and Lehmann B. *"Self-Exited Oscillations and Mixing in a Heated Round Jet"* Journal of Fluid Mechanics, Vol. 213 611-639, 1990.
- Moser R.D. and Rogers M.M. *"The 3-Dimensional Evolution of a Plane Mixing Layer - Pairing and Transition to Turbulence"* Journal of Fluid Mechanics, Vol. 247 275-320, 1993.

- Nam S. *"Numerical Simulation of Actual Delivered Density of Sprinkler Spray through Fire Plumes"* Atomization and Sprays, Vol. 4 385-404, 1994.
- Nam S. *"Development of a Computational Model Simulating the Interaction between a Fire Plume and a Sprinkler Spray"* Fire Safety Journal, Vol. 26 1-33, 1996.
- Nam S. *"Numerical Simulation of the Penetration Capability of Sprinkler Sprays"* Fire Safety Journal, Vol. 32 307-329, 1999.
- O'Hern T.J., Weckman E.J., Gerhart A.L., Tieszen S.R. and Schefer R.W. *"Experimental Study of a Turbulent Buoyant Helium Plume"* Journal of Fluid Mechanics, Vol. 544 143-171, 2005.
- Okong'o N.A. and Bellan J. *"Consistent Large-Eddy Simulation of a Temporal Mixing Layer Laden with Evaporating Drops. Part 1. Direct Numerical Simulation, Formulation and a priori Analysis"* Journal of Fluid Mechanics, Vol. 499 1-47, 2004.
- Pantano C. and Sarkar S. *"A Study of Compressibility Effects in the High-Speed Turbulent Shear Layer Using Direct Simulation"* Journal of Fluid Mechanics, Vol. 451 329-371, 2002.
- Pantano C., Sarkar S. and Williams F.A. *"Mixing of a Conserved Scalar in a Turbulent Reacting Shear Layer"* Journal of Fluid Mechanics, Vol. 481 291-328, 2003.
- Pera C., Réveillon J., Vervisch L. and Domingo P. *"Modeling Subgrid Scale Mixture Fraction Variance in LES of Evaporating Spray"* Combustion and Flame, Vol. 146 635-648, 2006.
- Persson B. and Ingason H. *"Modelling of Interaction between Sprinklers and Fire Vents - Present Knowledge"* SP REPORT 1996:32, Fire Technology, Swedish National Testing and Research Institute, 1996.
- Pitsch H. *"Large-Eddy Simulation of Turbulent Combustion"* Annual Review of Fluid Mechanics, Vol. 38 453-482, 2006.

- Poinsot T.J. and Lele S.K. *"Boundary-Conditions for Direct Simulations of Compressible Viscous Flows"* Journal of Computational Physics, Vol. 101 (1) 104-129, 1992.
- Poinsot T. and Veynante D. *"Theoretical and Numerical Combustion (2nd Edition)"* Edwards, 2005.
- Pope S.B. *"PDF Methods for Turbulent Reactive Flows"* Progress in Energy and Combustion Science, Vol. 11 (2) 119-192, 1985.
- Pope S.B. *"Turbulent Premixed Flames"* Annual Review of Fluid Mechanics, Vol. 19 237-270, 1987.
- Pope S.B. *"Ten Questions Concerning the Large-Eddy Simulation of Turbulent Flows"* New Journal of Physics, Vol. 6 Art. No. 35, 2004.
- Prasad K. and Baum H.R. *"Coupled Fire Dynamics and Thermal Response of Complex Building Structures"* Proceedings of the Combustion Institute, Vol. 30 2255-2262, 2005.
- Prasad K., Li C. and Kailasanath K. *"Simulation of Water Mist Suppression of Small Scale Methanol Liquid Pool Fires"* Fire Safety Journal, Vol. 33 (3) 185-212, 1999.
- Prasad K., Li C., Kailasanath K., Ndubizu C., Ananth R. and Tatem P.A. *"Numerical Modeling of Water Mist Suppression of Methane-Air Diffusion Flames"* Combustion Science and Technology, Vol. 132 (1-6) 325-364, 1998.
- Ramaprian B.R. and Chandrasekhara M.S. *"LDA Measurements in Plane Turbulent Jets"* Journal of Fluids Engineering – Transactions of the ASME, Vol. 107 (2) 264-271, 1985.
- Ravier S., Abid M., Amielh M. and Anselmet F. *"Direct Numerical Simulations of Variable-Density Plane Jets"* Journal of Fluid Mechanics, Vol. 546 153-191, 2006.
- Réveillon J. and Vervisch L. *"Spray Vaporization in Nonpremixed Turbulent Combustion Modeling: A Single Droplet Model"* Combustion and Flame, Vol. 121 (1-2) 75-90, 2000.

- Réveillon J. and Vervisch L. *"Analysis of Weakly Turbulent Dilute-Spray Flames and Spray Combustion Regimes"* Journal of Fluid Mechanics, Vol. 537 317-347, 2005.
- Réveillon J. and Demoulin F.-X. *"Effects of the Preferential Segregation of Droplets on Evaporation and Turbulent Mixing"* Journal of Fluid Mechanics, Vol. 583 273-302, 2007.
- Richards G.A., Casleton K.H. and Chorpening B.T. *"CO_2 and H_2O Diluted Oxy-Fuel Combustion for Zero-Emission Power"* Proceedings of the Institution of Mechanical Engineers Part A – Journal of Power and Energy, Vol. 219 (A2) 121-126 Special Issue, 2005.
- Richard J., Garo J.P., Souil J.M., Vantelon J.P. and Knorre V.G. *"Chemical and Physical Effects of Water Vapor Addition on Diffusion Flames"* Fire Safety Journal, Vol. 38 569-587, 2003.
- Rogers M.M. and Moser R.D. *"The Three-Dimensional Evolution of a Plane Mixing Layer: the Kelvin–Helmholtz Rollup"* Journal of Fluid Mechanics, Vol. 243 183-226, 1992.
- Sadiki A., Chrigui M., Janicka J. and Maneshkarimi M.R. *"Modeling and Simulation of Effects of Turbulence on Vaporization, Mixing and Combustion of Liquid-Fuel Sprays"* Flow Turbulence and Combustion, Vol. 75 (1-4) 105-130, 2005.
- Sandham N.D. and Reynolds W.C. *"A Numerical Investigation of the Compressible Mixing Layer"* Report No. TF-45, Stanford University, 1989.
- Sandhu H.S. and Sandham N.D. *"Boundary Conditions for Spatially Growing Compressible Shear Layers"* QMW-EP-1100, Internal Report, Queen Mary and Westfield College, 1994.
- Sankaran V. and Menon S. *"LES of Spray Combustion in Swirling Flows"* Journal of Turbulence, Vol. 3 Art. No. 011, 2002.
- Sazhin S.S. *"Advanced Models of Fuel Droplet Heating and Evaporation"* Progress in Energy and Combustion Science, Vol. 32 162-214, 2006.

- Schmitt M.P. *"Thermally Accurate LES of the Stability-Emission Performance of Staged Gas-Turbine Combustion"* Ph.D. Thesis, CERFACS, 2005.
- Schwille J.A. and Lueptow R.M. *"The Reaction of a Fire Plume to a Droplet Spray"* Fire Safety Journal, Vol. 41 390-398, 2006a.
- Schwille J.A. and Lueptow R.M. *"Effect of a Fire Plume on Suppression Spray Droplet Motion"* Atomization and Sprays, Vol. 16 563-577, 2006b.
- Segura J.C., Eaton J.K. and Oefelein J.C. *"Predictive Capabilities of Particle-Laden Large Eddy Simulation"* Report No. TSD-156, Stanford University, 2004.
- Sheikhi M.R.H., Drozda T.G., Givi P., Jaberi F.A. and Pope S.B. *"Large Eddy Simulation of a Turbulent Nonpremixed Piloted Methane Jet Flame (Sandia Flame D)"* Proceedings of the Combustion Institute, Vol. 30 549-556, 2005.
- Sheppard D.T. and Lueptow R.M. *"Characterization of Fire Sprinkler Sprays Using Particle Image Velocimetry"* Atomization and Sprays, Vol. 15 341-362, 2005.
- Shotorban B. and Mashayek F. *"Modeling Subgrid-Scale Effects on Particles by Approximate Deconvolution"* Physics of Fluids, Vol. 17 (8) Art. No. 081701, 2005.
- Sirignano W.A. *"Fluid Dynamics and Transport of Droplets and Sprays"* Cambridge University Press, New York, 2005.
- Smagorinsky J. *"General circulation experiments with the primitive equations: I. The basic experiment"* Monthly Weather Review, Vol. 91 99-164, 1963.
- Spalding D.B. *"The Combustion of Liquid Fuels"* Proceedings of the Combustion Institute, Vol. 4 847-864, 1953.
- Squires K.D. and Eaton J.K. *"Particle Response and Turbulence Modification in Isotropic Turbulence"* Physics of Fluids A – Fluid Dynamics, Vol. 2 (7) 1191-1203, 1990.
- Squires K.D. and Eaton J.K. *"Preferential Concentration of Particles by Turbulence"* Physics of Fluids A – Fluid Dynamics, Vol. 3 (5) 1169-1179, 1991.

- Sreedhara S. and Huh K.Y., *"Conditional Statistics of Nonreacting and Reacting Sprays in Turbulent Flows by Direct Numerical Simulation"* Proceedings of the Combustion Institute, Vol. 31 2335-2342, 2007.
- Stanley S.A., Sarkar S. and Mellado J.P. *"A Study of the Flow-Field Evolution and Mixing in a Planar Turbulent Jet Using Direct Numerical Simulation"* Journal of Fluid Mechanics, Vol. 450 377-407, 2002.
- Tang L., Wen F., Yang Y., Crowe C.T., Chung J.N. and Troutt T.R. *"Self-Organizing Particle Dispersion Mechanism in a Plane Wake"* Physics of Fluids A – Fluid Dynamics, Vol. 4 (10) 2244-2251, 1992.
- Tatem P.A., Beyler C.L., Dinenno P.J., Budnick E.K., Back G.G. and Younis S.E. *"A Review of Water Mist Technology for Fire Suppression"* NRL/MR/6180-94-7624, Naval Research Laboratory, 1994.
- Thomas F.O. and Chu H.C. *"An Experimental Investigation of the Transition of a Planar Jet – Subharmonic Suppression and Upstream Feedback"* Physics of Fluids A – Fluid Dynamics Vol. 1 (9) 1566-1587, 1989.
- Thompson K.W. *"Time-Dependant Boundary-Conditions for Hyperbolic Systems"* Journal of Computational Physics, Vol. 68 (1) 1-24, 1987.
- Thompson K.W. *"Time-Dependant Boundary-Conditions for Hyperbolic Systems .2."* Journal of Computational Physics, Vol. 89 (2) 439-461, 1990.
- Tieszen S.R. *"On the Fluid Mechanics of Fires"* Annual Review of Fluid Mechanics, Vol. 33 67-92, 2001.
- Vervisch L. and Poinsot T. *"Direct Numerical Simulation of Non-Premixed Turbulent Flames"* Annual Review of Fluid Mechanics, Vol. 30 655-691, 1998.
- Veynante D. and Knikker R. *"Comparison between LES Results and Experimental Data in Reacting Flows"* Journal of Turbulence, Vol. 7 Art. No. 35, 2006.
- Veynante D. and Vervisch L. *"Turbulent Combustion Modeling"* Progress in Energy and Combustion Science, Vol. 28 (3) 193-266, 2002.

- Vreman B. *"Direct and Large-Eddy Simulation of the Compressible Turbulent Mixing Layer"* Ph.D. Thesis, University of Twente, 1995.
- Vreman B., Geurts B. and Kuerten H. *"Subgrid-Modeling in LES of Compressible Flow"* Applied Scientific Research, Vol. 54 (3) 191–203, 1995.
- Wang Y. and Rutland C.J. *"Effects of Temperature and Equivalence Ratio on the Ignition of n-Heptane Fuel Spray in Turbulent Flow"* Proceedings of the Combustion Institute, Vol. 30 893-900, 2005.
- Wang Y. and Rutland C.J. *"Direct Numerical Simulation of Ignition in Turbulent n-Heptane Liquid-Fuel Spray Jets"* Combustion and Flame, Vol. 149 353-365, 2007.
- White F.M. *"Viscous Fluid Flow (2nd Edition)"* McGraw-Hill, 1991.
- Williams F.A. *"Combustion Theory (2nd Edition)"* The Benjamin/Cummings Publishing Company, Inc., California, 1985.
- Williams F.A. *"Progress in Knowledge of Flamelet Structure and Extinction"* Progress in Energy and Combustion Science, Vol. 26 657-682, 2000.
- Wray A.A. *"Very Low Storage Time-Advancement Schemes"* Internal Report, NASA-Ames Research Center, California, 1986.
- Xia J., Luo K.H. and Kumar S. *"Large-Eddy Simulation of a Turbulent Diffusion Flame Laden with Evaporating Droplets"* FEDSM2006-98443, 2006 ASME Joint U.S. – European Fluids Engineering Summer Meeting, Miami, FL, 2006.
- Xia J., Luo K.H. and Kumar S. *"Large-Eddy Simulation of Interactions Between a Reacting Jet and Evaporating Droplets"* Flow, Turbulence and Combustion, Vol. 80 133-153, 2008.
- Xiao K., Schmidt D. and Maas U. *"A Study of Local Flame Structures in Piloted Jet Diffusion Flame Using a Probability Density Function Method"* Proceedings of the Combustion Institute, Vol. 28 157-165, 2000.

- Xin Y., Gore J., McGrattan K.B., Rehm R.G. and Baum H.R. *"Large Eddy Simulation of Buoyant Turbulent Pool Fires"* Proceedings of the Combustion Institute, Vol. 29 259-266, 2002.
- Xu J. and Pope S.B. *"PDF Calculations of Turbulent Nonpremixed Flames with Local Extinction"* Combustion and Flame, Vol. 123 281-307, 2000.
- Yamamoto Y., Potthoff M., Tanaka T., Kajishima T. and Tsuji Y. *"Large-Eddy Simulation of Turbulent Gas-Particle Flow in a Vertical Channel: Effect of Considering Inter-Particle Collisions"* Journal of Fluid Mechanics, Vol. 442 303-334, 2001.
- Yoon S.S., Kim H.Y., DesJardin P.E., Hewson J.C., Tieszen S.R. and Blanchat T.K. *"Unsteady RANS Modeling of Water-Spray Suppression for Large-Scale Compartment Pool Fires"* Atomization and Sprays, Vol. 17 1-45, 2007.
- Yoshizawa A. *"Statistical-Theory for Compressible Turbulent Shear Flows, with the Application to Subgrid Modeling"* Physics of Fluids, Vol. 29 (7) 2152-2164, 1986.
- Yu M.H. and Monkewitz P.A. *"Oscillations in the Near-Field of a Heated 2-Dimensional Jet"* Journal of Fluid Mechanics, Vol. 255 323-347, 1993.
- Yuu S., Ueno T. and Umekage T. *"Numerical Simulation of the High Reynolds Number Slit Nozzle Gas-Particle Jet Using Subgrid-Scale Coupling Large Eddy Simulation"* Chemical Engineering Science, Vol. 56 (14) 4293-4307, 2001.
- Zhou X., Luo K.H. and Williams J.J.R. *"Large-Eddy Simulation of a Turbulent Forced Plume"* European Journal of Mechanics B – Fluids, Vol. 20 (2) 233-254, 2001a.
- Zhou X., Luo K.H. and Williams J.J.R. *"Study of Density Effects in Turbulent Buoyant Jets Using Large-Eddy Simulation"* Theoretical and Computational Fluid Dynamics, Vol. 15 (2) 95-120, 2001b.
- Zhou X., Luo K.H. and Williams J.J.R. *"Vortex Dynamics in Spatio-Temporal Development of Reacting Plumes"* Combustion and Flame, Vol. 129 (1-2) 11-29, 2002.

Publications

Journal Publications:

(1) K.H. Luo, J. Xia and E. Monaco, "Multiscale Modelling of Multiphase Flow with Complex Interactions", submitted to *Journal of Multiscale Modelling*.

(2) J. Xia, K.H. Luo and S. Kumar, "Large-Eddy Simulation of Interactions between a Reacting Jet and Evaporating Droplets", *Flow Turbulence and Combustion* **80**, 133-153 (2008).

Refereed Conference Papers:

(1) J. Xia, K.H. Luo and S. Kumar, "Dynamic Interactions between a Buoyant Reacting Plume and Evaporating Droplets", accepted for presentation and publication at the 9th International Symposium on Fire Safety Science.

(2) J. Xia and K.H. Luo, "Direct Numerical Simulation of Diluted Combustion by Evaporating Droplets", accepted for an oral presentation at the 32nd International Symposium on Combustion.

(3) J. Xia, K.H. Luo and S. Kumar, "Large-Eddy Simulation of Interactions between a Fire Plume and Water Spray", The Fifth International Seminar on Fire and Explosion Hazards, Edinburgh, UK, April 23-27 2007.

(4) J. Xia, K.H. Luo and S. Kumar, "Large-Eddy Simulation of a Turbulent Diffusion Flame Laden with Evaporating Droplets", FEDSM2006-98443, 2006 ASME Joint U.S. – European Fluids Engineering Summer Meeting, Miami, FL, 2006.

(5) J. Xia, K.H. Luo and S. Kumar, "Large-Eddy Simulation of Interactions between a Reacting Jet and Evaporating Droplets", Conference on Turbulence and Interactions - TI2006, Porquerolles, France, 2006.

Other Conference Papers:

(1) J. Xia, K.H. Luo and S. Kumar, "Large-Eddy Simulation of a Turbulent Buoyant Flame Interacting with Droplets", The Fifth International Conference on Fluid Mechanics – ICFM-V, Shanghai, China, August 15-19 2007.

(2) J. Xia, K.H. Luo and S. Kumar, "Study on Suppression of a Reacting Plume by Evaporating Droplets Using Large-Eddy Simulation", The Third European Combustion Meeting - ECM2007, Chania, Crete, Greece, April 11-13 2007.

Presentations

Oral Presentations:

(1) "Investigation of Droplet Effects on a Reacting Plume Using Dynamic Large-Eddy Simulation", Joint UK Turbulence Consortium / UK Turbulence Platform Workshop, The Beaulieu Hotel, Beaulieu, UK, 27 September 2007.

(2) "Large-Eddy Simulation of a Turbulent Buoyant Flame Interacting with Droplets", The Fifth International Conference on Fluid Mechanics – ICFM-V, Shanghai, China, 16 August 2007.

(3) "Large-Eddy Simulation of Turbulent Reactive Flows Laden with Non-Reactive Droplets", COCCFEA (Consortium on Computational Combustion for Engineering Applications) Summer School for Computational Combustion using High Performance Computing, Cranfield University, 18 July 2007.

(4) "Large-Eddy Simulation of Interactions between a Fire Plume and Water Spray", The Fifth International Seminar on Fire and Explosion Hazards, Edinburgh, UK, 26 April 2007.

(5) "Large-Eddy Simulation of Multiphase Reacting Flows", COCCFEA workshop, Imperial College, London, UK, 19 December 2006.

(6) "Multiphase Reacting Flow Simulations on HPCx", Workshop on Computational Engineering on HPCx, Daresbury Laboratory, Warrington, UK, 14 December 2006.

(7) "Parallel DNS/LES of Multiphase Turbulent Flows", UK Turbulence Consortium Workshop, The Beaulieu Hotel, Beaulieu, UK, 22 September 2006.

(8) "Study of the Interactions of Water-Spray with a Turbulent Buoyant Plume and Suppression Mechanisms of Fires", BRE Trust PhD studentship Annual Review and Presentations, BRE, Watford, UK, 18 September 2006.

(9) "Large-Eddy Simulation of Interactions between a Reacting Jet and Evaporating Droplets", Conference on Turbulence and Interactions - TI2006, Porquerolles, France, 29 May 2006.

Poster Presentations:

(1) "Dynamic Large-Eddy Simulation of a Simplified Small Fire Suppression System", Atomisation and Spray Combustion, The Autumn Meeting of The Combustion Institute (British Section), Imperial College, London, 26 September 2007.

(2) "Study on Suppression of a Reacting Plume by Evaporating Droplets Using Large-Eddy Simulation", The Third European Combustion Meeting - ECM2007, Chania, Crete, Greece, 13 April 2007.

(3) "Dynamic LES of a Heated Planar Jet", One-day meeting on Current Research in Combustion: A Forum for Research Students and Young Researchers, organized by the Combustion Physics Group, Institute of Physics, Loughborough Conference Centre, Loughborough, 21 September 2005.